8-2011

Low-Thrust Assited Angles-Only Navigation

Robert W. Gillis
Utah State University

LOW-THRUST ASSISTED ANGLES-ONLY NAVIGATION

by

Robert W. Gillis

A thesis submitted in partial fulfillment
of the requirements for the degree

of

MASTER OF SCIENCE

in

Mechanical Engineering

Approved:

David K. Geller, Ph.D. Major Professor	Don Cripps, Ph.D. Committee Member
Stephen A. Whitmore, Ph.D. Committee Member	Mark R. McLellan, Ph.D. Vice President for Research and Dean of Graduate Studies

UTAH STATE UNIVERSITY
Logan, Utah

2011

Abstract

Low-Thrust Assisted Angles-Only Navigation

by

Robert W. Gillis, Master of Science

Utah State University, 2011

Major Professor: David K. Geller, Ph.D.
Department: Electrical and Computer Engineering

Traditional spacecraft proximity operations require large and expensive on-board sensors and significant ground support. Relative angle measurements can be obtained from small, simple, and inexpensive on-board sensors, but have not traditionally been used for proximity operations because of difficulty generating range information. In this thesis it is shown that useful relative range data can be generated provided that the spacecraft is experiencing a small continuous thrust such as would be provided by a low-thrust propulsion system. In previous work range observability was shown with impulsive maneuvers. This thesis will expand this work to low-thrust spacecraft and will show how range can be observed under normal operating conditions. The low-thrust methods covered here may be particularly useful in higher orbits (such as GEO) where the gravity gradient is relatively small. A computer simulation is used to develop and test guidance, navigation, and control algorithms for such maneuvers. The capabilities and limitations of these techniques and algorithms are then analyzed.

(99 pages)

To my best friend and loving companion, Juli, who makes every day far better than it could possible be without her.

Acknowledgments

I feel it is very important to thank the many individuals that have helped me get to this point. First I would like to thank my research adviser, Dr. Geller. I could not have asked for a better mentor. Without his insightful guidance the work would not have been possible.

I would like to thank my loving wife and companion, Juli. Her constant love has been a light and an inspiration to me. Nothing I can say can ever fully express my appreciation for her.

I would also like to thank my caring parents. Their faith in me and constant encouragement has given me courage to attempt daunting task and to work harder and longer than I thought I could.

There have been many other friends, classmates, teachers, and mentors, too numerous to list here by name, who have been of invaluable help in my studies and life. Whether explaining a complicated subject, helping me to succeed in a difficult class, inspiring me to reach higher than I thought possible, or simply helping to destress and take a break, I would not have been able to accomplish nearly as much without their support.

Contents

List of Tables

List of Figures

Notation

Decorations

$\bar{o}$	Vector (3x1 matrix)
$\hat{o}$	Estimated Value
$\widetilde{o}$	Measured Value
$\dot{o}$	First time derivative
$\ddot{o}$	Second time derivative

Superscripts

o^-	Previous Estimate
o^+	Updated Estimate

Subscripts

o_c	Chaser values
o_t	Target values
o_{rel}	Relative value
o^{frame}	Value as observed and coordinated in "frame"

Errors

ν	Measurement Error $(\widetilde{o} - \bar{o})$
e	Residual Error $(\widetilde{o} - \hat{o})$

Noise

$\mathbf{w}$	Process Noise
$\mathbf{n}$	Measurement Noise

Other

O	Capital is a matrix
$[o\times]$	Cross Product Matrix Form
$\mathbf{o}$	Bold lower case is a nx1 matrix
f(x)	function of x
I	Identity matrix

Acronyms

AON	angles-only navigation
ARCSS	Autonomous Rendezvous and Capture Sensor System
AVGS	Advanced Video Guidance Sensor
DART	Demonstration of Autonomous Rendezvous and Technology; spacecraft
DOF	degree of freedom
ECI	earth-centered inertial frame
EKF	extended Kalman filter
GN&C	guidance, navigation, and control
GEO	geosynchronous orbit
LEO	low-earth orbit
LIDAR	light detection and ranging
LVLH	local vertical local horizontal frame
LOS	line-of-sight
LQR	linear quadratic regulator
MUBLCOM	Multiple Paths, Beyond-Line-of-Sight; satellite
PD	position-derivative (controller)
RPO	rendezvous and proximity operations
XSS-11	the eXperimental Satellite System-11; spacecraft

Chapter 1

Introduction

There are a wide variety of missions that are best accomplished using some type of proximity maneuvers. Many space missions and programs like Apollo and the International Space Station would not have been possible without docking and other proximity maneuvers. Today there is a growing interest in expanding proximity operations capabilities to new types of missions and crafts [1][2][3]. In particular, there is considerable interest in autonomous satellites that monitor, inspect, and service other spacecraft. Relative angle measurements can be generated from small inexpensive sensors, but have not traditionally been used for proximity operations because of difficulty determining range [4]. Past research projects at Utah State University have worked on techniques to gain range information from angle measurements. These studies show that, in some cases, impulsive maneuvers can make relative range observable [5]. This study aims to not only expands this work to low-thrust, but also to shows how range can be made observable under normal operating conditions. For example, previous studies were inconclusive on whether station keeping directly below a targeted spacecraft could produce range information [6].

The focus of this study is on generating range information using only angle measurements and maneuvers achievable with low levels of thrust, such as would be provided by an electric propulsion system. These systems have become increasingly common with literally hundreds now operating in orbit [7]. These systems are characterized by a high specific impulse with low levels of thrust. There characteristics can can potentially provide many benefits to a mission, including increased payload, longer operational life, expanded operations, and launch vehicle class step-downs [8]. Some of the electric propulsion systems are more scalable than conventional rockets, and can be sized for small spacecraft that could not carry other types of propulsion systems. While the electric systems cannot generate the level of thrust provided by traditional thrusters, they are capable of firing continuously for long periods of time. This both allows and necessitates different types of maneuvers for gaining navigation information. These same types of maneuvers would also be used by a system with a low powered chemical or cold gas system.

Chapter 2

Thesis Statement

The purpose of this thesis is to determine if angles only navigation (AON) can produce significant range information when assisted by low continuous thrust. This is accomplished by developing an orbital simulation tool that uses an extended Kalman filter (EKF) to estimate the relative position between a chaser and target spacecraft. Range errors and filter covariances are analyzed to determine the level of range knowledge. Specifically, 3-σ bounds on position are calculated from the Kalman filter covariance matrix. With a correctly implemented Kalman filter the true position is almost always within these bounds. If the 3-σ bounds in the line-of-sight (LOS) direction decrease due to angle measurements taken during a low-thrust maneuver then it can be concluded that angles-only navigation (AON) produced range information. This will be called low-thrust assisted angles-only navigation.

The Δv of the maneuvers are also recorded in an attempt to gain some feel for how efficient different maneuvers are in using propellants to obtain range information. In general though this study does not attempt to find optimal maneuvers based on a particular criterion.

All simulations include six degrees of freedom (DOF) dynamics. White process noise is used simulate unmodeled/expected accelerations such as errors in thruster knowledge, solar pressure, higher gravity terms, and so forth. Camera measurements are also corrupted with white noise to simulate measurement errors. The chief objective is to show the feasibility of low-thrust-assisted AON for determining ranges information in the LOS direction. Performance studies for specific spacecraft and more complex error models will be the focus of future research.

Chapter 3

Literature Survey

3.1 A Brief History of Proximity Operations

Angle measurements played an essential role in some of the earliest proximity operations. Both Gemini [9] and Apollo [10] used angle measurements, acquired by the human eye, combined with other instruments to determine the relative position. These missions also partially relied on the human eye for relative attitude determination. This approach fit with the United States preference for manual verses automatic control, and, without the need for as elaborate sensor and algorithm development, allowed the United States to develop the ability to perform complex proximity operations more quickly than the autonomous approach taken by the Russians. This early achievement of complex proximity operation may have been instrumental in winning the race to the moon [5].

As time went on spacecraft proximity operations techniques and hardware became progressively more complex. Though Russia took much longer to develop its far more autonomous spacecraft, Soyuz has become known for its high level of dependability [5]. Soyuz relies on multiple radars to determine range, range rate, relative angle, and relative attitude [11]. The Space Shuttle primarily uses radar for relative navigation, and is also equipped with a laser ranging device and a center-line camera. Unlike Soyuz, Space Shuttle proximity operations are flown manually [12]. The radar based systems used on Soyuz and the Space Shuttle are too heavy and power intensive for many smaller spacecraft. Soyuz requires active communication and cooperation from the targeted spacecraft, and the methods used by the Space Shuttle to capture non-cooperative satellites are done manually.

A series of experimental spacecraft have been launched in an attempt to develop new technology for proximity operations that would be more fitting for smaller unmanned spacecraft. The XSS-11 (eXperimental Satellite System-11) was a micro-satellite (dry/wet weight 105/145 kg) used to successfully demonstrate rendezvous and proximity operations (RPO) with various derelict (no way of assisting XSS-11) resident space objects (RSO). The XSS-11 system primarily uses LIDAR (light detection and ranging) for relative position measurements [1]. The Demonstration of Au-

tonomous Rendezvous and Technology (DART) spacecraft was a modified Pegasus fourth stage equipped with an Advanced Video Guidance Sensor (AVGS), which had a camera and used a laser to illuminate reflectors strategically placed on the target [2]. The intent was for DART to use AVGS to perform proximity operations around a Multiple Paths, Beyond-Line-of-Sight Communications (MUBLCOM) satellite. Unfortunately software errors and inadequacies in the GN&C systems caused DART to crash into MUBLCOM before it could accomplish its mission objectives [13]. A third rendezvous experiment, Orbital Express was equipped with the three cameras that made up the Autonomous Rendezvous and Capture Sensor System (ARCSS), and the same laser based AVGS system used on DART and a laser range-finder [3]. Orbital Express was able to successfully complete several proximity and docking maneuvers.

3.2 Angles-Only Navigation for Proximity Operations

In 1801 Carl Friedrich Gauss used angle measurements to successfully determine the orbit of the planetoid Ceres [14]. This proved that as few as three pairs of angle measurements taken close together can accurately determine all orbital elements [15]. Relative-angle-navigation has also been shown to be a viable solution for satellite navigation [16]. However at closer ranges ($<$ 100 km) Gauss's method runs into difficulty. For two spacecraft near each other with similar orbits, there exist whole families of possible relative trajectories that share nearly the same angular measurements and differ only by range [4]. This makes it impossible to determine range information from unassisted angle measurements [17]. There have been several attempts to overcome this limitation. When the chaser is close enough it has been shown that range can be determined by measuring the angle between optical beacons placed on the target spacecraft or other target features [18][19]. It has also been shown that range can be determined if angle measurements to the target are taken from two cooperating spacecraft [20]. There has also been attempts to improve angles-only navigation by changing the coordinate system [21], and to combine angle measurements with other measurements [22]. All these methods have there advantages and disadvantages. The focus of this study is on using maneuvers executed by the chaser to enhance range detectability. In 2001 Raja Chari and David Geller used linear covariance to show that range information could be generated from angle measurements alone if assisted by appropriate maneuvers [4]. In 2008 Dave Woffinden expanded on this work by creating a six degree-of-freedom simulation with angles-only navigation. This

simulation modeled a maneuvering chaser spacecraft that used angle measurements to achieve range information to a target spacecraft [23]. In 2010 Jason Schmidt examined the effect of accelerometer measurement error, accelerometer bias, misalignment, and noise, on the range observability problem [6].

3.3 A Brief Introduction to Low-Thrust Propulsion

Electric propulsion systems use electric and/or magnetic fields to accelerated propellant. Because they are not limited by the amount of energy stored in a fuel they can achieve a much higher Δv with the same amount of propellant. While electrical systems can be very fuel efficient, thrust is limited by the amount of electric power the spacecraft can provide. Electric propulsion systems were first tested in space in the 1960s [24]. Since then the number and diversity of electric propulsion systems has grown and there are now hundreds in use [7]. There are a wide variety of electric propulsion systems each best suited for different missions or tasks. Ion propulsion systems have had significant success in deep space exploration missions such as NASA's Deep Space 1 and Dawn spacecraft [25]. Here very high efficiencies allow for missions with high total Δv [26]. Work to develop more advanced ion thrusters for even more ambitions missions is on going [27]. Hall effect thrusters are commonly used for spacecraft station-keeping [28]. Some types of electric propulsion systems such as pulsed plasma thrusters (PPT) [29], field emission electric propulsion (FEEP) [30], and colloid thrusters [31] can be used on small scales where more traditional propulsion systems would be impractical.

3.4 Motivation for Proposed Work

The maneuver assisted angles-only navigation studies discussed above have focused on maneuvers executed with thrusters that give relatively high levels of thrust over a short time period or burst. No studies have looked at the effect of nominal operational maneuvers or low-thrust maneuvers on range observability.

This project aims to expand on past work by investigating maneuvers and filtering techniques that may generate range information when combined with low levels of continuous thrust as would be produced by an electric thruster. Continuous thrust can be used to gradually move from one orbit to another or to modify or displace orbits [32] (like hovering directly below a another spacecraft etc.). This study will focus in particular on range information that can be gained from one of these

modified/displaced orbits. Many of the maneuvers and filtering techniques explored here may also be appropriate for a a low powered chemical or cold gas propulsion system.

Chapter 4

Orbital Relative Motion

In many space applications it is convenient to express position and velocity relative to a point other than the central body. For relative motion problems it is often particularly useful to center the coordinate system on the target. The Clohessy-Wiltshire (CW) are a linearization of orbital motion of the chaser in target centered coordinates. This allows the various relative motion trajectories used in this thesis to be analyzed much more intuitively than would be possible in Earth centered coordinates.

This chapter begins by defining three important reference frames used in this thesis. Then the CW equations will be developed. Finally key relative orbital paths will be defined using the CW equations.

4.1 Reference Frames

Depending on which is most appropriate to a given task, three different reference frames may be used. Earth centered inertial (ECI) frame is defined with the origin at the center of the earth. Unit vectors describing the ECI axis are defined as:

$$\bar{i}_x = \text{unit vector parallel to mean equinox}$$

$$\bar{i}_z = \text{unit vector parallel to Earth's spin axis} \tag{4.1}$$

$$\bar{i}_y = \bar{i}_z \times \bar{i}_x$$

The local vertical local horizontal (LVLH) frame is defined with the origin at the target spacecraft. Unit vectors describing the LVLH axis are defined as:

$$\bar{i}_z = \frac{\bar{r}_t}{|\bar{r}_t|} \quad \text{(local vertical direction)}$$

$$\bar{i}_y = \frac{\bar{r}_t \times \bar{v}_t}{|\bar{r}_t \times \bar{v}_t|} \quad \text{(cross-track direction)} \tag{4.2}$$

$$\bar{i}_x = \bar{i}_y \times \bar{i}_z \quad \text{(local horizonal direction)}$$

where $\bar{r}_t$ is the vector from the center of the Earth to the target, and $\bar{v}_t$ is the velocity vector of the target.

The boresight frame is defined with the origin at the chaser spacecraft. Unit vectors describing the boresight frame are defined as:

$$\bar{i}_x = \frac{\bar{r}_{rel}}{|\bar{r}_{rel}|}$$

$$\bar{i}_y = \frac{\bar{h}_p \times \bar{r}_{rel}}{|\bar{h}_p \times \bar{r}_{rel}|} \tag{4.3}$$

$$\bar{i}_z = \bar{i}_x \times \bar{i}_y$$

where:

$$\bar{r}_{rel} = \bar{r}_c - \bar{r}_t \tag{4.4}$$

$$\bar{h}_p = r_t \times v_t \tag{4.5}$$

Coordinate transformations

Often it will be necessary to transform vectors coordinatized in one reference frame into another reference frame. If only position vectors need to be transformed this can be done by the rotation matrix:

$$R_{c2\to c1} = \begin{bmatrix} \left(\bar{i}_{c1x}^{c2}\right)^T \\ \left(\bar{i}_{c1y}^{c2}\right)^T \\ \left(\bar{i}_{c1z}^{c2}\right)^T \end{bmatrix} \tag{4.6}$$

where $\bar{i}_{c1x}^{c2}$, $\bar{i}_{c1y}^{c2}$, and $\bar{i}_{c1z}^{c2}$ are unit vectors describing the $c1$ coordinate system axes coordinatized in the $c2$ frame. Position vectors can then be rotated into the new coordinate system using:

$$\bar{r}^{c1} = R_{c2\to c1}\bar{r}^{c2} \tag{4.7}$$

This rotation matrix can also be used to transform any vector in $c1$ to $c2$. However, the time derivative of vectors must be handled differently. Regardless of what frame a vector is coordinatized in, its time derivative as viewed in $c1$, is related to its time derivative as viewed in $c2$, through the following relationship.

$$\frac{d\bar{b}}{dt}|_{c1} = \frac{d\bar{b}}{dt}|_{c2} + \bar{\omega}_{c2/c1} \times \bar{b} \tag{4.8}$$

where $\bar{\omega}_{c2/c1}$ is the rotation of the $c2$ frame relative to the $c1$ frame. When $\bar{b}$ is a position vector, the above equation is:

$$\bar{v}_{c1} = \bar{v}_{c2} + \bar{\omega}_{c2/c1} \times \bar{r} \tag{4.9}$$

where $\bar{v}_{c1}$ is the derivative of the position vector $\bar{r}$ as observed from the $c1$ frame and $\bar{v}_{c2}$ is the derivative of $\bar{r}$ as observed from the $c2$ frame. The vectors in this expression can then be coordinatized in the frame $c1$:

$$\bar{v}_{c1}^{c1} = \bar{v}_{c2}^{c1} + \bar{\omega}_{c2/c1}^{c1} \times \bar{r}^{c1} \tag{4.10}$$

or in frame $c2$:

$$\bar{v}_{c1}^{c2} = \bar{v}_{c2}^{c2} + \bar{\omega}_{c2/c1}^{c2} \times \bar{r}^{c2} \tag{4.11}$$

Combining Equations 4.7 and 4.10 gives:

$$\begin{bmatrix} \bar{r}^{c1} \\ \bar{v}^{c1}_{c1} \end{bmatrix} = T_{c2\to c1} \begin{bmatrix} \bar{r}^{c2} \\ \bar{v}^{c2}_{c2} \end{bmatrix} = \begin{bmatrix} R_{c2\to c1} & 0_{3x3} \\ \left[\bar{\omega}^{c1}_{c2/c1}\times\right] R_{c2\to c1} & R_{c2\to c1} \end{bmatrix} \begin{bmatrix} \bar{r}^{c2} \\ \bar{v}^{c2}_{c2} \end{bmatrix} \tag{4.12}$$

where $[\bar{\omega}\times]$ is the cross-product matrix:

$$\left[\bar{\omega}^{c1}_{c2/c1}\times\right] = \begin{bmatrix} 0 & -\omega_3 & \omega_2 \\ \omega_3 & 0 & -\omega_1 \\ -\omega_2 & \omega_1 & 0 \end{bmatrix} \tag{4.13}$$

4.2 Derivation of the Clohessy-Wiltshire Equations

When dealing with the relative motion between two spacecraft, it is often convenient to work in a coordinate system fixed to one of the vehicles, such as the LVLH coordinate system. The Clohessy-Wiltshire (CW) equations are a linearization of the relative motion dynamics in the LVLH coordinate system. This allows many relative orbital motion problems to be solved directly in LVLH coordinates.

4.2.1 Time Derivatives in a Rotating Frame

Let $\mathcal{S}_0$ be an inertial frame and $\mathcal{S}$ be a frame rotating with angular velocity $\bar{\omega}$. For clarity in this section only, subscript $\mathcal{S}_0$ and $\mathcal{S}$ will be used to indicate which frame a derivative is being observed from. For example $\left(\frac{d\bar{o}}{dt}\right)_{\mathcal{S}_0}$ is the derivative of the vector $\bar{o}$ as observed from the inertial frame $\mathcal{S}_0$, and $\left(\frac{d\bar{o}}{dt}\right)_{\mathcal{S}}$ is the derivative of $\bar{o}$ as observed from the rotating frame $\mathcal{S}$.

Let $\begin{bmatrix} \bar{e}_1 & \bar{e}_2 & \bar{e}_3 \end{bmatrix}$ be a set of orthonormal unit vectors fixed in the rotating $\mathcal{S}$ frame. The derivative of each unit vector as observed from the inertial $\mathcal{S}_0$ frame can be expressed as:

$$\left(\frac{d\bar{e}_i}{dt}\right)_{\mathcal{S}_0} = \bar{\omega} \times \bar{e}_i \tag{4.14}$$

A vector $\bar{u}$ can be expressed as $\bar{u} = \sum_i u_i \bar{e}_i$. The time derivative of $\bar{u}$ as observed from $\mathcal{S}_0$ can now be written as:

$$\left(\frac{d\bar{u}}{dt}\right)_{\mathcal{S}_0} = \sum_i \frac{du_i}{dt}\bar{e}_i + \sum_i u_i \left(\frac{d\bar{e}_i}{dt}\right)_{\mathcal{S}_0} \tag{4.15}$$

Recognizing that the first summation is the derivative of $\bar{u}$ as observed from $\mathcal{S}$ and substituting in Equation 4.14:

$$\left(\frac{d\bar{u}}{dt}\right)_{\mathcal{S}_0} = \left(\frac{d\bar{u}}{dt}\right)_{\mathcal{S}} + \bar{\omega} \times \bar{u} \tag{4.16}$$

To apply these results to the relative orbital motion problem, let $\bar{r}_{rel}$ be the vector from a target spacecraft to a chaser spacecraft. Using Equation 4.16, the derivative of $\bar{r}_{rel}$ as observed from $\mathcal{S}_0$ (i.e. the velocity of the chaser relative to the target as observed from an inertial frame) can be expressed as:

$$\left(\frac{d\bar{r}_{rel}}{dt}\right)_{\mathcal{S}_0} = \left(\frac{d\bar{r}_{rel}}{dt}\right)_{\mathcal{S}} + \bar{\omega} \times \bar{r}_{rel} = \bar{v}_{rel} + \bar{\omega} \times \bar{r}_{rel} \tag{4.17}$$

where $\bar{v}_{rel}$ is velocity of the chaser relative to the target as observed from the rotating frame $\mathcal{S}$. Applying Equation 4.16 again:

$$\left(\frac{d^2\bar{r}_{rel}}{dt^2}\right)_{\mathcal{S}_0} = \bar{a}_{rel} + \dot{\bar{\omega}} \times \bar{r}_{rel} + 2\bar{\omega} \times \bar{v}_{rel} + \bar{\omega} \times \bar{\omega} \times \bar{r}_{rel} \tag{4.18}$$

where $\bar{a}_{rel}$ is acceleration as observed from the rotating frame $\mathcal{S}$.

4.2.2 Linearization of Relative Orbital Motion

Assuming a point mass gravity model, the chaser's and target's orbital dynamics can be expressed as:

$$\ddot{\bar{r}}_c = -\mu \frac{\bar{r}_c}{|\bar{r}_c|^3} + \bar{a}_{thrust} \tag{4.19}$$

$$\ddot{\bar{r}}_t = -\mu \frac{\bar{r}_t}{|\bar{r}_t|^3} \tag{4.20}$$

where $\bar{r}_c$ and $\bar{r}_t$ are the position of the chaser and target spacecraft relative to the earth's center, and $\bar{a}_{thrust}$ is the thrust produced by the chaser's engines. Letting $\bar{r}_{rel}$ be the vector from the target to the chaser. The chaser's position can then be expressed as:

$$\bar{r}_c = \bar{r}_t + \bar{r}_{rel} \tag{4.21}$$

Substituting Equation 4.21 into Equation 4.19:

$$\ddot{\bar{r}}_t + \ddot{\bar{r}}_{rel} = -\mu \frac{\bar{r}_t + \bar{r}_{rel}}{|\bar{r}_t + \bar{r}_{rel}|^3} + \bar{a}_{thrust} \tag{4.22}$$

Expanding Equation 4.22 as a Taylor series and neglecting the higher order terms:

$$\ddot{\bar{r}}_t + \ddot{\bar{r}}_{rel} = -\mu \frac{\bar{r}_t}{|\bar{r}_t|^3} - \frac{\mu}{|\bar{r}_t|^3} \left[I_{3x3} - 3 \frac{\bar{r}_t \bar{r}_t^T}{|\bar{r}_t|^2} \right] \bar{r}_{rel} + \bar{a}_{thrust} \tag{4.23}$$

and substituting in Equation 4.20:

$$\ddot{\bar{r}}_{rel} = -\frac{\mu}{|\bar{r}_t|^3} \left[I_{3x3} - 3 \frac{\bar{r}_t \bar{r}_t^T}{|\bar{r}_t|^2} \right] \bar{r}_{rel} + \bar{a}_{thrust} \tag{4.24}$$

4.2.3 The Clohessy-Wiltshire Equations

Substituting Equation 4.18 into Equation 4.24 gives:

$$-\frac{\mu}{|\bar{r}_t|^3} \left[I_{3x3} - 3 \frac{\bar{r}_t \bar{r}_t^T}{|\bar{r}_t|^2} \right] \bar{r}_{rel} + \bar{a}_{thrust} = \bar{a}_{rel} + \dot{\bar{\omega}} \times \bar{r}_{rel} + 2\bar{\omega} \times \bar{v}_{rel} + \bar{\omega} \times \bar{\omega} \times \bar{r}_{rel} \tag{4.25}$$

where $\bar{\omega}$ in now the target's orbital angular rate vector. If a circular orbit is assumed: $\dot{\bar{\omega}} = 0$ and $|\bar{\omega}|^2 = \frac{\mu}{|\bar{r}_t|^3} = \text{constant}$, then the above equation can be written as:

$$-|\bar{\omega}|^2 \left[I_{3x3} - 3 \frac{\bar{r}_t \bar{r}_t^T}{|\bar{r}_t|^2} \right] \bar{r}_{rel} + \bar{a}_{thrust} = \bar{a}_{rel} + 2\bar{\omega} \times \bar{v}_{rel} + \bar{\omega} \times \bar{\omega} \times \bar{r}_{rel} \tag{4.26}$$

Expressing all the vectors in the equation above in LVLH coordinates:

$$\bar{r}_{rel} = \begin{pmatrix} x \\ y \\ z \end{pmatrix}, \quad \bar{v}_{rel} = \begin{pmatrix} \dot{x} \\ \dot{y} \\ \dot{z} \end{pmatrix}, \quad \bar{a}_{rel} = \begin{pmatrix} \ddot{x} \\ \ddot{y} \\ \ddot{z} \end{pmatrix}, \quad \bar{r}_t = \begin{pmatrix} 0 \\ 0 \\ r_t \end{pmatrix}, \quad \bar{\omega} = \begin{pmatrix} 0 \\ \omega \\ 0 \end{pmatrix}, \quad \bar{a}_{thrust} = \begin{pmatrix} a_x \\ a_y \\ a_z \end{pmatrix}$$

yields three scalar equations:

$$\ddot{x} = -2\omega\dot{z} + a_x \tag{4.27}$$

$$\ddot{y} = -\omega^2 y + a_y \tag{4.28}$$

$$\ddot{z} = 3\omega^2 z + 2\omega\dot{x} + a_z \tag{4.29}$$

where a_x, a_y, and a_z are the components of the chaser thrust $\bar{a}_{thrust}$. These are the Clohessy-Wiltshire equations.

In the absence of any thrust accelerations ($a_x = a_y = a_z = 0$), the CW equations can also be written as:

$$x(t) = \left[6z_0 + \frac{4\dot{x}_0}{\omega}\right]\sin(\omega t) + \left[\frac{2\dot{z}_0}{\omega}\right]\cos(\omega t) - [6\omega z_0 + 3\dot{x}_0]\,t + \left[x_0 - \frac{2\dot{z}_0}{\omega}\right] \tag{4.30}$$

$$y(t) = [y_0]\cos(\omega t) + \left[\frac{\dot{y}_0}{\omega}\right]\sin(\omega t) \tag{4.31}$$

$$z(t) = \left[\frac{\dot{z}_0}{\omega}\right]\sin(\omega t) - \left[3z_0 + \frac{2\dot{x}_0}{\omega}\right]\cos(\omega t) + \left[4z_0 + \frac{2\dot{x}_0}{\omega}\right] \tag{4.32}$$

$$\dot{x}(t) = [6\omega z_0 + 4\dot{x}_0]\cos(\omega t) - [2\dot{z}_0]\sin(\omega t) - [6\omega z_0 + 3\dot{x}_0] \tag{4.33}$$

$$\dot{y}(t) = [\dot{y}_0]\cos(\omega t) - [\omega y_0]\sin(\omega t) \tag{4.34}$$

$$\dot{z}(t) = [\dot{z}_0]\cos(\omega t) + [3\omega z_0 + 2\dot{x}_0]\sin(\omega t) \tag{4.35}$$

4.3 Relative Orbital Trajectories

In this thesis, several types of relative orbital motion are used to analyze the effectiveness

of angles only navigation. Proximity operations are often described in terms of the R-bar (radial vector) and V-bar (velocity vector) directions. In LVLH coordinates the R-bar (the z position) is in the local-vertical direction and the V-bar (the x position) is in the local-horizontal direction. The chaser is said to be on the V-bar or R-bar if it is only displaced from the target in that direction. For example, if the chaser is "on the V-bar" this is equivalent to saying it is only displaced in the local horizontal direction relative to the target.

4.3.1 Station-Keeping

Several cases will be considered where the chaser is station-keeping relative to the target in LVLH coordinates. By setting the first and second derivatives in Equations 4.27, 4.28, and 4.29 to zero, the necessary thrust needed to maintain a constant position in LVLH coordinates can be calculated as:

$$a_x = 0 \tag{4.36}$$

$$a_y = \omega^2 y \tag{4.37}$$

$$a_z = -3\omega^2 z \tag{4.38}$$

It can easily be seen from the above equations that if the chaser is station-keeping on the V-bar ($y = 0$ and $z = 0$) then no thrust is required to maintain position (though thrust still may be required to correct disturbances).

4.3.2 Co-elliptic Approach

In a co-elliptic approach the chaser's local vertical position is constant, $z(t) = z_0$. Looking at Equation 4.32 it can be seen that this happens when $\dot{x}_0 = -\frac{3}{2}\omega z_0$ and $\dot{z}_0 = 0$. Applying these assumptions to the Clohessy Wiltshire equations for the local vertical and horizontal positions and velocities gives:

$$x(t) = -\frac{3}{2}\omega z_0 t \tag{4.39}$$

$$z\left(t\right) = z_0 = \text{constant} \tag{4.40}$$

$$\dot{x}\left(t\right) = -\frac{3}{2}\omega z_0 = \text{constant} \tag{4.41}$$

$$\dot{z}\left(t\right) = 0 = \text{constant} \tag{4.42}$$

4.3.3 Football Orbit

Another type of relative orbital motion is a football orbit. If the chaser is placed close to the target and put in an orbit with the same period but slightly different eccentricity than the target the relative motion will trace out a 2x1 ellipse around the target over the course of one orbit. This is illustrated in Figure 4.1.

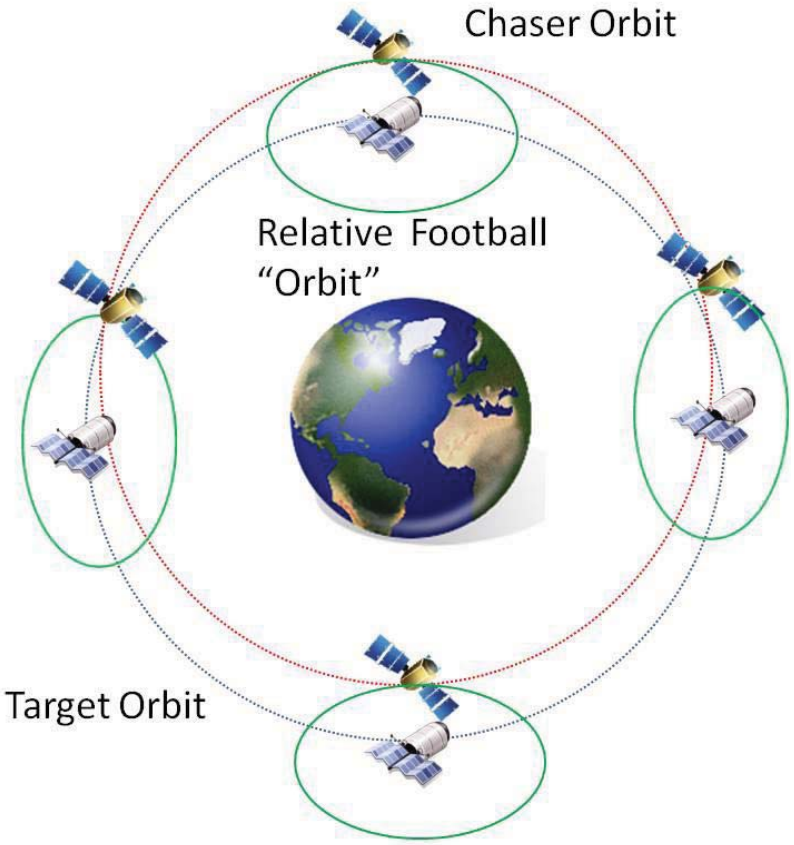

Fig. 4.1: Chaser in football orbit around target.

This relative orbit requires no thrusting by either spacecraft and can be analyzed in terms of Equations 4.30 through 4.35. For example if the chaser is starting directly below the target, $x_0 = 0$, with no local vertical velocity, $\dot{z}_0 = 0$, and a local horizontal velocity $\dot{x}_0 = -2\omega z_0$ then Equations 4.30 and 4.32 simplify to:

$$x(t) = -2z_0 \sin(\omega t) \tag{4.43}$$

$$z(t) = z_0 \cos(\omega t) \tag{4.44}$$

which will trace out a z_0 by $2z_0$ ellipse. To get velocity, the same assumptions are applied to Equations 4.33 and 4.35.

$$\dot{x}(t) = -2z_0\omega \cos(\omega t) \tag{4.45}$$

$$\dot{z}(t) = -z_0\omega \sin(\omega t) \tag{4.46}$$

Alternately, thrust can be used to modify the football motion, either to change the rate at which the chaser goes around the target, modify the football shape, or both.

Chapter 5

Simulation Development

A Matlab/Simulink satellite rendezvous simulation is used to determine whether or not low-thrust assisted angle measurements can determine relative range. The simulation models a maneuvering chaser spacecraft and a target spacecraft in earth orbit. The chaser attempts to use angle measurements and maneuvers to determine the range to the target. The simulation includes 6 degrees of freedom vehicle dynamics, star camera, gyro, and line of sight camera models, as well as reaction wheels, and thruster models. The focus of this project will be on developing a Kalman filter appropriate for determining relative position from angle measurements. Simple translational and pointing control laws are also be included. An overview of the chaser in Simulink can by seen in Figure 5.1.

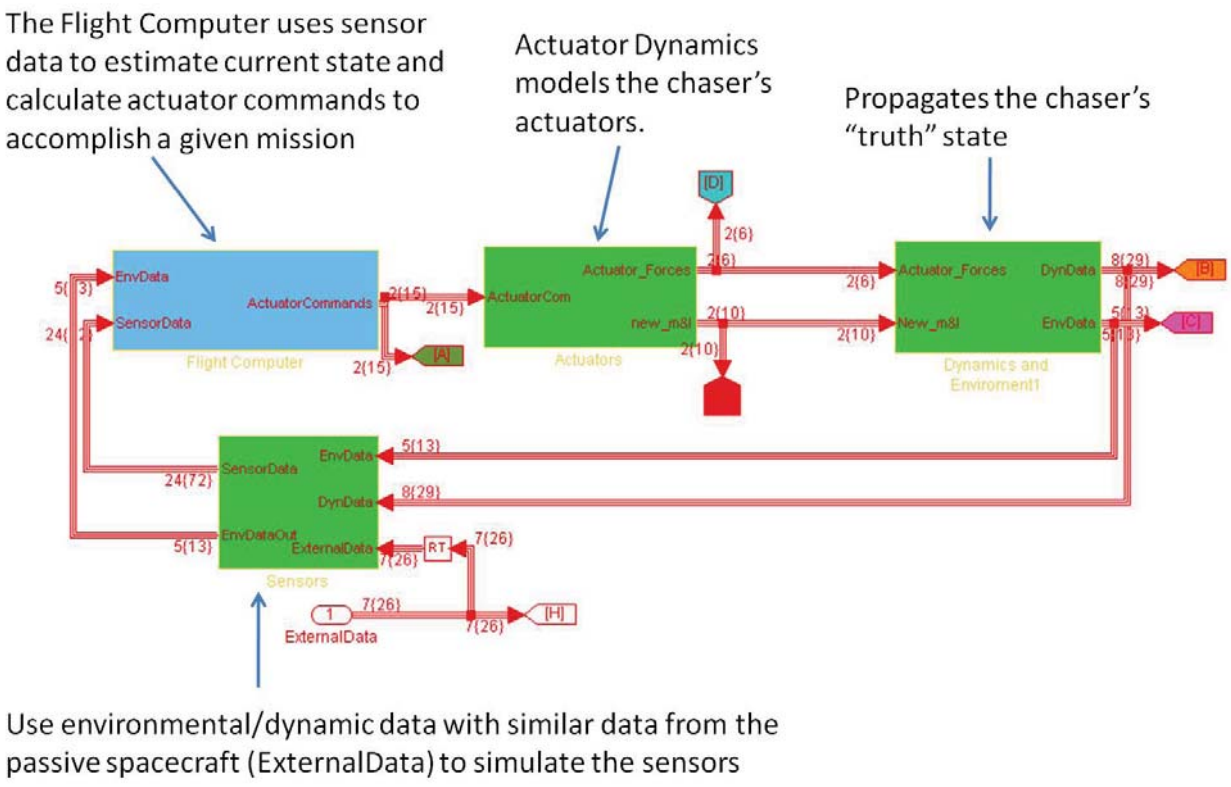

Fig. 5.1: High level model of the chaser in Simulink.

5.1 Environmental Model

The environmental model includes a point mass gravity model. White process noise is used to simulate unmodeled acceleration perturbations such as higher order gravity terms, solar pressure, aerodynamic drag, Lunar perturbations, and so forth. Higher fidelity models of these disturbances are not required for this study.

5.2 Vehicle Dynamics

Translational Dynamics

The spacecraft orbits are propagated in ECI coordinates using an Runge-Kutta fourth order integrator, and the dynamics:

$$\dot{\bar{r}}_t = \bar{v}_t$$

$$\dot{\bar{v}}_t = \bar{a}_t \tag{5.1}$$

$$\dot{\bar{r}}_c = \bar{v}_c$$

$$\dot{\bar{v}}_c = \bar{a}_c$$

The target and chaser accelerations are calculated using:

$$\bar{a}_t = \frac{\mu \bar{r}_t}{|\bar{r}_t|^3} + \bar{w}_{proc} \tag{5.2}$$

$$\bar{a}_c = \frac{\mu \bar{r}_c}{|\bar{r}_c|^3} + T_{body \to I} \bar{a}_{com}^{body} + \bar{w}_{thrust} \tag{5.3}$$

where $\bar{a}_{com}$ is the force that would be produced by perfect thrusters, $\bar{\omega}_{thrust}$ is process noise added to simulated thruster errors, and $T_{body \to I}$ is the transformation from body to inertial frame. It has been shown previously that, for simulation relative motion, placing all of the process noise ($\bar{\omega}_{proc}$) on the target is exactly the same as placing process noise on both vehicles [6].

Rotational Dynamics

Rotational dynamics are propagated using Euler's equation and a Simulink integrator. Angular velocity ($\bar{\omega}$) is calculated by integrating the angular acceleration, which is given by:

$$\dot{\bar{\omega}} = \mathbf{I}^{-1}\left(\bar{T} - \bar{\omega} \times \mathbf{I}\bar{\omega}\right) \tag{5.4}$$

where the inertia is:

$$\mathbf{I} = \begin{bmatrix} 1 & 0 & 0 \\ 0 & 1 & 0 \\ 0 & 0 & 1 \end{bmatrix} \; kg\, m^2 \tag{5.5}$$

The rotational kinematics are described by:

$$\dot{q} = \frac{1}{2}\Omega\left(\bar{\omega}\right) q \tag{5.6}$$

where q is the rotational position and:

$$\Omega\left(\bar{\omega}\right) = \begin{bmatrix} -\left[\bar{\omega}\times\right] & \bar{\omega} \\ -\bar{\omega} & 0 \end{bmatrix} \tag{5.7}$$

$$\left[\bar{\omega}\times\right] = \begin{bmatrix} 0 & -\omega_3 & \omega_2 \\ \omega_3 & 0 & -\omega_1 \\ -\omega_2 & \omega_1 & 0 \end{bmatrix} \tag{5.8}$$

The quaternion derivative is then integrated to obtain the attitude quaternion q.

5.3 Actuator Models

Because the purpose of this simulation is to explore navigation concepts and not attitude control, the momentum wheels are assumed to give the commanded torque without delay and

without error. The thruster model consist of 12 thrusters (two on each side of a cube, all equal distance for the center of mass). Although this configuration of thrusters can be used to control attitude, in this study attitude is always controlled with the momentum wheels. Thrusters are only used for translational control, and two thrusters pointing in the same direction on opposite sides of the spacecraft always fire with equal thrust and are perfectly coupled. This arrangement of thrusters will also allow the chaser to accelerate in any direction. For most cases the thrusters and momentum wheels will be considered perfect. The effect of thruster noise and angular acceleration process noise will be studied briefly in Chapter 8.

5.4 Sensor Models

An on board star-camera gives the current attitude of the chaser in the form of a quaternion and gyros provide the current angular velocity of the spacecraft in the form of a vector. A line-of-sight camera returns the azimuth and elevation angles of the target in the body frame. The camera model includes azimuth and elevation white noise to represent camera inaccuracies such as measurement bias, misalignment, and pixelation.

Line-of-sight Camera

The line-of-sight camera provides elevation and azimuth angles corrupted by zero-mean white noise n_{cam}.

$$\theta_{elevation} = sin^{-1}\left(i_{rel,z}\right) + n_{cam} \tag{5.9}$$

$$\theta_{azimuth} = tan^{-1}\left(\frac{i_{rel,y}}{i_{rel,x}}\right) + n_{cam} \tag{5.10}$$

where $i_{rel,x}$, $i_{rel,y}$ and $i_{rel,z}$ are the x y z components of the unit vector $\bar{i}_{rel}^{cam} = \bar{r}_{rel}^{cam} / |\bar{r}_{rel}^{cam}|$ and $\bar{r}_{rel}^{cam}$ is the vector from the chaser to the target in the camera frame.

Star-Tracker

For this simulation, a perfect star-tracker is used to define the orientation of the chasers body frame. The effect of any non-zero tracker errors can be easily modeled as LOS-camera error.

Gyros

For this simulation, perfect gyros are used to measure the attitude rate of the body/chaser frame. These measurements are used by the attitude control law. The attitude rate error in the control law is the difference between the desired angular velocity, as given by the pointing algorithm, and the attitude rate measured by the gyros.

5.5 Flight Algorithms (GN&C)

The chaser's simulated flight computer must accomplish the following: translational guidance; translational estimation; translational control; pointing; attitude determination; and attitude control. Algorithms are implemented for each of these tasks. A summary of these task is given in Figure 5.2.

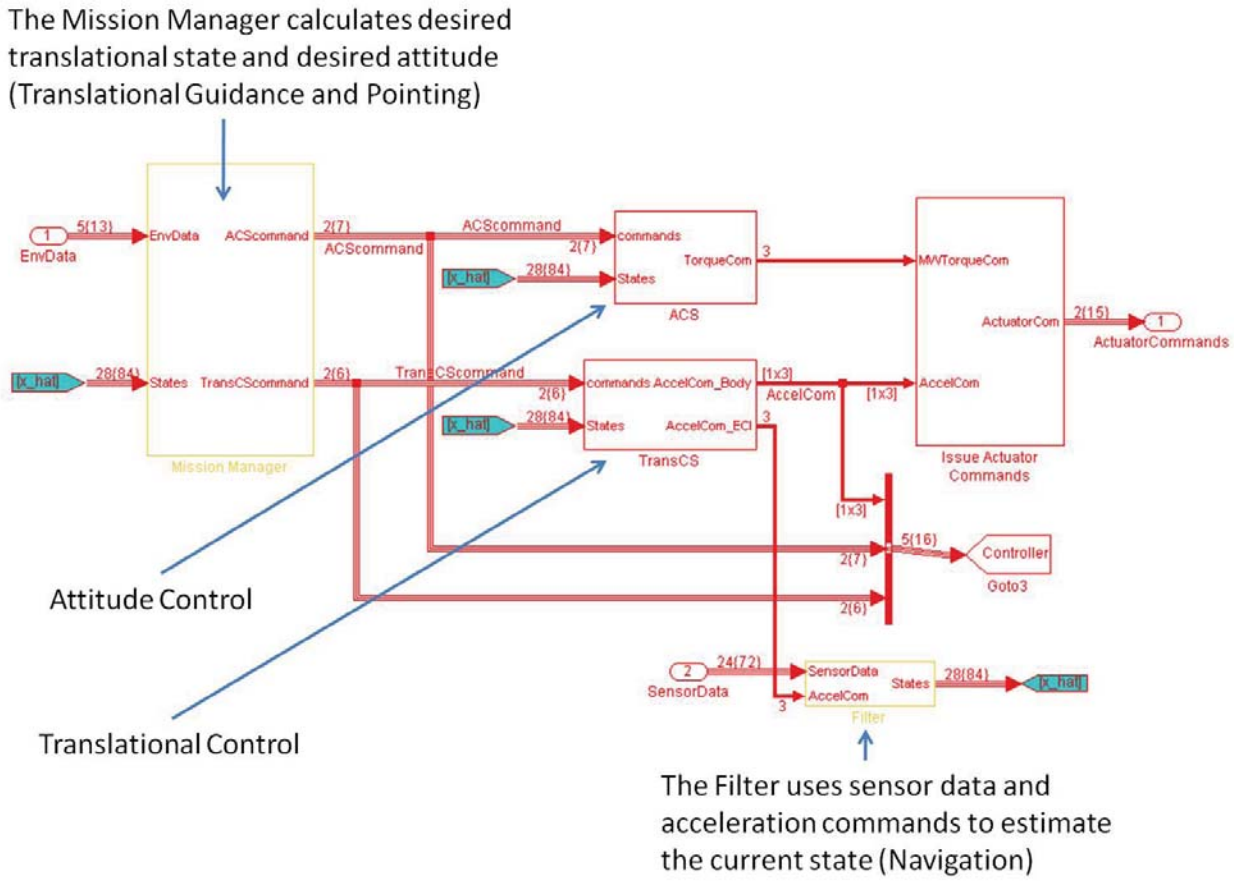

Fig. 5.2: Flight computer in Simulink.

Translational Guidance

A summary of the translational guidance is given in Figure 5.3. The translational guidance is based upon a preplanned relative path. The preplanned path is specified by a function that takes time as an input and returns desired position and velocity. The simplest case is when the chaser is commanded to station keep:

$$\bar{r}_{des}^{lvlh} = \bar{r}_{start}^{lvlh} = \text{constant} \tag{5.11}$$

$$\bar{v}_{des}^{lvlh} = 0 \tag{5.12}$$

where $\bar{r}_{start}^{lvlh}$ and $\bar{r}_{des}^{lvlh}$ are the initial and current desired relative positions in the LVLH frame, and $\bar{v}_{des}^{lvlh}$ is the desired current velocity in the LVLH frame.

Another type of preplanned path is the case where the chaser travels in a straight line relative to the target (as observed from the LVLH frame). The equation for desired position can then be written as:

$$\bar{r}_{des}^{lvlh} = t\bar{v}_{des}^{lvlh} + \bar{r}_{start}^{lvlh} \tag{5.13}$$

The desired velocity is then the derivative of the desired position:

$$\bar{v}_{des}^{lvlh} = \bar{v}_{start}^{lvlh} = \text{constant} \tag{5.14}$$

It is sometimes desirable for the chaser to follow a linear path relative to the target, but at a non-constant velocity. For example the chaser may start in a natural co-elliptical approach, use thrust to accelerate its approach (still following the same path), and then decelerate at the end to station-keep below the target. This more complex maneuver requires that a few more parameters and stages be added to the above equations. The maneuver will be divided into three stages; the "acceleration stage," the "main stage," and the "deceleration stage." The acceleration stage runs while $t < \tau_{accel}$ where τ_{accel} is the length of the acceleration stage. The desired velocity for this stage is:

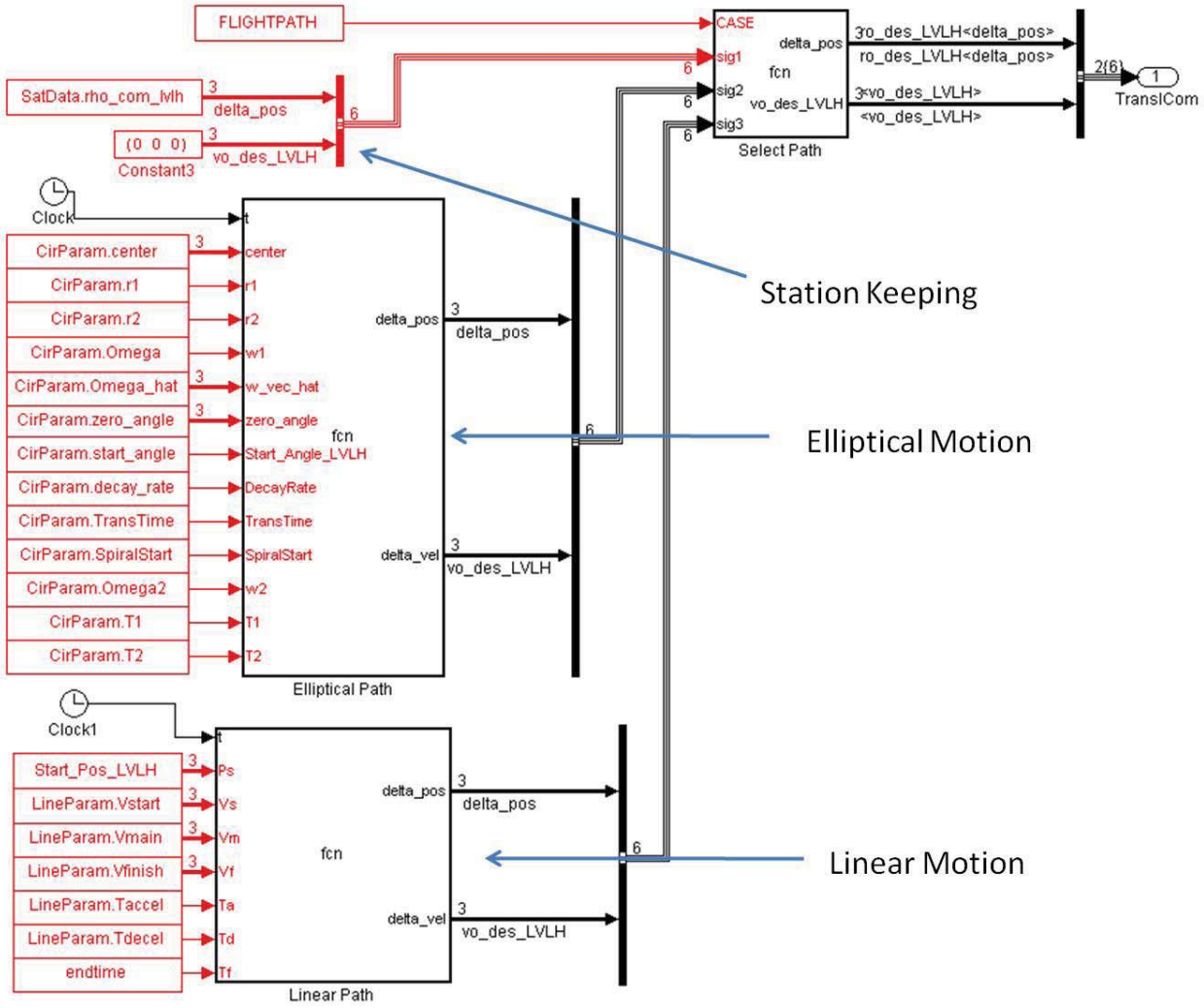

Fig. 5.3: Translational guidance in Simulink.

$$\bar{v}_{des}^{lvlh} = \bar{v}_{start}^{lvlh} + \frac{t}{\tau_{accel}} \left(\bar{v}_{main}^{lvlh} - \bar{v}_{start}^{lvlh} \right) \tag{5.15}$$

where $\bar{v}_{start}^{lvlh}$ and $\bar{v}_{main}^{lvlh}$ are the desired initial and main stage velocities. It can be seen that Equation 5.15 will return $\bar{v}_{int}^{lvlh}$ at the beginning of the simulation and then gradually increase the desired velocity until $\bar{v}_{des}^{lvlh} = \bar{v}_{main}^{lvlh}$ at $t = \tau_{accel}$ at which point the chaser enters in to the main stage. The desired velocity during the main stage is then given by:

$$\bar{v}_{des}^{lvlh} = \bar{v}_{main}^{lvlh} \tag{5.16}$$

The chaser enters the deceleration stage when $t > \tau_{dec}$. The desired velocity for this stage is given by:

$$\bar{v}_{des}^{lvlh} = \bar{v}_{main}^{lvlh} + \frac{(t - \tau_{dec})}{(t_f - \tau_{dec})} \left(\bar{v}_{final}^{lvlh} - \bar{v}_{main}^{lvlh} \right) \tag{5.17}$$

The desired positions for each stage is then given by the integrals of the above equations with the appropriate constants of integration. Desired position during the acceleration stage is given by:

$$\bar{r}_{des}^{lvlh} = t\bar{v}_{start}^{lvlh} + \frac{t^2}{2\tau_{accel}} \left(\bar{v}_{main}^{lvlh} - \bar{v}_{start}^{lvlh} \right) + \bar{r}_{start}^{lvh} \tag{5.18}$$

Desired position during the main stage is given by:

$$\bar{r}_{des}^{lvh} = t\bar{v}_{main}^{lvh} + \frac{\tau_{accel}}{2} \left(\bar{v}_{start}^{lvh} - \bar{v}_{main}^{lvh} \right) \tag{5.19}$$

And finally desired position during the deceleration stage is given by:

$$\bar{r}_{des}^{lvlh} = c_1 \bar{v}_{main}^{lvlh} + c_2 \bar{v}_{final}^{lvlh} + c_3 \bar{v}_{start}^{lvlh} \tag{5.20}$$

where:

$$c_1 = t - t\frac{\frac{t}{2} - \tau_{dec}}{t_f - \tau_{dec}} - \frac{\tau_{dec}^2}{2\left(t_f - \tau_{dec}\right)} - \frac{\tau_{accel}}{2} \tag{5.21}$$

$$c_2 = t\frac{\frac{t}{2} - \tau_{dec}}{t_f - \tau_{dec}} + \frac{\tau_{dec}^2}{2\left(t_f - \tau_{dec}\right)} \tag{5.22}$$

$$c_3 = \frac{\tau_{accel}}{2} \tag{5.23}$$

If $\bar{v}_{start}^{lvlh} = \bar{v}_{main}^{lvlh} = \bar{v}_{final}^{lvlh}$, then these equation simplify to Equations 5.13 and 5.14 above. It is worth noting that, depending on the values the variables are set to, the chaser can decelerate in the "acceleration stage" and accelerate in the "deceleration stage" as easily as the other way around.

A third type of preplanned path considered is an elliptical path. Once again the translational guidance is a function that takes time as an input and returns desired position and velocity in LVLH. Also, once again, this maneuver with be divided into stages. In this case there will be an initial stage, an acceleration stage, and a final stage. This will represent an ellipse that maintains one speed

for a while, accelerates/decelerates to another speed, and then maintains that speed. Additionally, this type of path can be set us so that the chaser will spiral in towards the target. This is done by adding a variable that gradually decreases the dimensions of the base football orbit.

Let α_{des} be the the desired angular position relative to the target, as observed from the LVLH frame. The initial stage desired angular position and rate can then be written as:

$$\dot{\alpha}_{des} = \omega_{init} \tag{5.24}$$

$$\alpha_{des} = t\omega_{init} \tag{5.25}$$

where ω_{init} is the initial desired angular velocity. For the acceleration stage the equation is then written as:

$$\dot{\alpha}_{des} = \frac{\tau_2 - t}{\tau_2 - \tau_1}\omega_{init} + \frac{t - \tau_1}{\tau_2 - \tau_1}\omega_{final} \tag{5.26}$$

$$\alpha_{des} = \frac{t\tau_2 - \frac{1}{2}t^2}{\tau_2 - \tau_1}\omega_{init} + \frac{\frac{1}{2}t^2 - t\tau_1}{\tau_2 - \tau_1}\omega_{final} + c_1 \tag{5.27}$$

where τ_1 and τ_2 are the beginning and ending time of the acceleration stage, and c_1 is a constant of integration and is given by:

$$c_1 = -\frac{\tau_1\tau_2 - \frac{1}{2}\tau_1^2}{\tau_2 - \tau_1}\omega_{init} + \frac{\frac{1}{2}\tau_1^2}{\tau_2 - \tau_1}\omega_{final} + \tau_1\omega_{init} \tag{5.28}$$

For the final stage, the desired angular positions and rates are given by:

$$\dot{\alpha}_{des} = \omega_{final} \tag{5.29}$$

$$\alpha_{des} = t\omega_{final} + c_1 + c_2 \tag{5.30}$$

where the second integration constant is given by:

$$c_2 = \frac{\frac{1}{2}\tau_2^2}{\tau_2 - \tau_1}\omega_{init} + \frac{\frac{1}{2}\tau_2^2 - \tau_2\tau_1}{\tau_2 - \tau_1}\omega_{final} - \tau_2\omega_{final} \tag{5.31}$$

When the size of the ellipse is held constant, the desired positions and velocities are given by:

$$\bar{r}_{des}^{lvlh} = r_{minor}\cos(\alpha_{des})\,\bar{i}_x^{lvlh} + r_{major}\sin(\alpha_{des})\,\bar{i}_y^{lvlh} \tag{5.32}$$

$$\bar{v}_{des}^{lvlh} = -\dot{\alpha}_{des} r_{min}\sin(\alpha_{des})\,\bar{i}_x^{lvlh} + \dot{\alpha}_{des} r_{major}\cos(\alpha_{des})\,\bar{i}_y^{lvlh} \tag{5.33}$$

where $\bar{i}_x^{lvlh}$ and $\bar{i}_y^{lvlh}$ are unit vectors in the LVLH local vertical and local horizontal directions, and r_{minor} and r_{major} are the magnitudes of the ellipse the chaser is moving in ($r_{major} = 2r_{minor}$). If the chaser is spiraling in towards the target, the above values are modified. The chaser starts in an ellipse and then accelerates in the relative radial direction. This radial acceleration stage can be expressed as:

$$\bar{r}_{des}^{lvlh} = \left(1 - \frac{(t-\tau_{s1})^2}{2\tau_{trans}} d_{radial}\right)\bar{r}_{base}^{lvlh} \tag{5.34}$$

$$\bar{v}_{des}^{lvlh} = \left(1 - \frac{(t-\tau_{s1})^2}{2\tau_{trans}} d_{radial}\right)\bar{v}_{base}^{lvlh} + \frac{(t-\tau_{s1})}{\tau_{trans}} d_{radial}\bar{r}_{base}^{lvlh} \tag{5.35}$$

where d_{radial} has units of inverse seconds and determines how fast the ellipse gets smaller. For example the chaser will follow a spiral path that decrease to half its original size over one 24 hour period (86400s) if $d_{radial} = 0.5/86500s$. Here $\bar{r}_{base}^{lvlh}$ and $\bar{v}_{base}^{lvlh}$ are the position and velocity given by Equations 5.32 and 5.33. In these equations, τ_{s1} is the beginning time of the acceleration stage and τ_{trans} is the length of the acceleration stage. Once the chaser enters the final stage, the desired position and velocity can be expressed as:

$$\bar{r}_{des}^{lvlh} = \left(1 - \left[t - \tau_{s1} - \frac{1}{2}\tau_{trans}\right] d_{radial}\right)\bar{r}_{base}^{lvlh} \tag{5.36}$$

$$\bar{v}_{des}^{lvlh} = \left(1 - \left[t - \tau_{s1} - \frac{1}{2}\tau_{trans}\right] d_{radial}\right)\bar{v}_{base}^{lvlh} - d_{radial}\bar{r}_{base}^{lvlh} \tag{5.37}$$

Pointing

The pointing algorithm is a simple target tracking algorithm. This algorithm computes an attitude command and attitude rate command to align the line-of-sight of the camera with the

relative position of the target as estimated by the translational navigation Kalman filter. First a commanded direction cosine matrix and commanded angular rate are calculated using:

$$R_{com} = \begin{bmatrix} \left(\bar{i}_x^{eci}\right) \\ \left(\bar{i}_y^{eci}\right) \\ \left(\bar{i}_z^{eci}\right) \end{bmatrix} \tag{5.38}$$

$$\bar{i}_x^{eci} = \frac{\left(\bar{r}_t^{eci} - \bar{r}_c^{eci}\right)}{|\bar{r}_{rel}|}$$

$$\bar{i}_y^{eci} = \frac{\left(\bar{r}_c^{eci} \times \bar{v}_c^{eci}\right) \times \bar{i}_x^{eci}}{|\left(\bar{r}_c^{eci} \times \bar{v}_c^{eci}\right) \times \bar{i}_x^{eci}|}$$

$$\bar{i}_z^{eci} = \bar{i}_x^{eci} \times \bar{i}_y^{eci}$$

$$\bar{\omega}_{com}^{eci} = \frac{\left(\bar{r}_t^{eci} - \bar{r}_c^{eci}\right) \times \left(\bar{v}_t^{eci} - \bar{v}_c^{eci}\right)}{\left|\left(\bar{r}_t^{eci} - \bar{r}_c^{eci}\right)\right|^2} \tag{5.39}$$

where $\bar{r}_c^{lvlh}$, $\bar{r}_t^{lvlh}$, $\bar{v}_c^{lvlh}$, $\bar{v}_t^{lvlh}$ are the position of the chaser, the position of the target, the velocity of the chaser and the velocity of the target in ECI coordinates.

Navigation

Navigation is based on a Kalman filter and will be discussed in detail in Chapter 6. The Kalman filter estimates 12 states, the position and velocity of chaser in the ECI frame and the position and velocity of target in the ECI frame. The filter uses a point mass gravity model and the acceleration commands given by the translational guidance algorithm to propagate the states, and azimuth and elevation angular measurements to update the states.

Attitude Determination

The attitude determination algorithm uses a star-tracker directly (no processing) to determination attitude. Gyros are used directly for attitude rate determination.

Translational Control

A linear quadratic regulator (LQR) is developed for translational control [33]. Many of the maneuvers that will be used in this study will often take place over time frames on the order of an orbital period with relatively low levels of thrust. It is therefore desirable to use a controller that takes orbital mechanics into account. As it is shown below, an LQR controller uses knowledge of the system dynamics (in the form of dynamic constraints) to determine the appropriate gains. While minimizing Δv is not the primary goal of this thesis, it is desirable to keepΔv low so that it can be better estimated how useful the maneuvers may be. Being derived from optimization theory, an LQR control should produce fuel efficient control profiles. The LQR controller is the solution to the following optimization problem:

$$\text{minimize: } J = \int_0^\infty \left((\mathbf{x} - \mathbf{x_p})^T A (\mathbf{x} - \mathbf{x_p}) + \mathbf{u}^T B \mathbf{u} \right) dt \tag{5.40}$$

where $\mathbf{x_p}$ is the planned state, $\mathbf{x}$ is the current state, and $\mathbf{u}$ is the thrust control, subject to the dynamic constraints:

$$\dot{\mathbf{x}} = F\mathbf{x} + G\mathbf{u} \tag{5.41}$$

The LQR is a good fit for the problems explored here, because it attempts to minimize the integral of the control $\bar{a}$. This is important because the type of thrusters studied here tend to have very low maximum thrust levels and because it is desirable to minimize the total Δv. The LQR also takes orbital dynamics into account via the dynamic constraints. This is particularly important since the low powered maneuvers used here can often span whole orbital periods, giving plenty of time for orbital dynamics to affect the trajectory and the control acceleration is often the same order of magnitude as the relative gravity acceleration.

For this application, $\mathbf{x_p}$ is the planned/desired relative position and velocity in LVLH coordinates:

$$\mathbf{x_p} = \begin{bmatrix} \bar{r}_{des}^{lvlh} \\ \\ \bar{v}_{des}^{lvlh} \end{bmatrix} \tag{5.42}$$

and $\mathbf{x}$ is the relative position and velocity in LVLH coordinates:

$$\mathbf{x} = \begin{bmatrix} \bar{r}_{rel}^{lvlh} \\ \\ \bar{v}_{rel}^{lvlh} \end{bmatrix} \tag{5.43}$$

and the control $\mathbf{u}$ is the thrust acceleration $\bar{a}_{thrust}$.

During proximity operations, the relative motion of 2 vehicles in near circular orbits is given by the Clohessy-Wiltshire (CW) equations [34].

$$\ddot{\bar{r}}_{rel}^{lvlh} = F_r \bar{r}_{rel} + F_v \bar{v}_{rel} + \bar{a}_{thrust} \tag{5.44}$$

where:

$$F_r = \begin{bmatrix} 0 & 0 & 0 \\ 0 & -\omega^2 & 0 \\ 0 & 0 & 3\omega^2 \end{bmatrix} \tag{5.45}$$

$$F_v = \begin{bmatrix} 0 & 0 & -2\omega \\ 0 & 0 & 0 \\ 2\omega & 0 & 0 \end{bmatrix} \tag{5.46}$$

Thus the F and G matrices in Equation 5.41 are given by:

$$F = \begin{bmatrix} 0_{3x3} & I_{3x3} \\ \\ F_r & F_v \end{bmatrix} \tag{5.47}$$

$$G = \begin{bmatrix} 0_{3x3} \\ \\ I_{3x3} \end{bmatrix} \tag{5.48}$$

One strategy for selecting the LQR weights[33] is to make them diagonal matrices using:

$$A_{ii} = \frac{1}{(max\,(\mathbf{x} - \mathbf{x_p})_i)^2}, \quad A_{ij} = 0 \quad \text{for} \quad j \neq i \tag{5.49}$$

$$B_{ii} = \frac{1}{(max\,\mathbf{u}_i)^2}, \quad B_{ij} = 0 \quad \text{for} \quad j \neq i \tag{5.50}$$

where $max\,(\mathbf{x} - \mathbf{x_p})_i$ is the maximum allowable error in state, and $max\,\mathbf{u}_i$ is the maximum desirable control. The solution to this optimization problem is:

$$\bar{a}^{lvlh}_{thrust}(t) = -B^{-1}G^T S_0\,(\mathbf{x}(t) - \mathbf{x_p}(t)) \tag{5.51}$$

where S_0 is computed via the algebraic Riccati equation:

$$0 = -S_0 F - F^T S_0 + S_0 G B^{-1} G^T S_0 - A \tag{5.52}$$

The thrust command is then rotated into body coordinates using:

$$\bar{a}^{body}_{thrust} = R_{lvlh \to body} \bar{a}^{lvlh}_{thrust} \tag{5.53}$$

where $R_{lvlh \to body}$ is defined as in Equation 4.6.

Attitude Control

The chasers attitude dynamics are simpler than the translational/orbital dynamics. Also the momentum wheels do not use fuel/Δv . For these reasons a simple position-derivative (PD) controller was implement. The torque command for the momentum wheels is given by:

$$\bar{T}^{body}_{com} = K_P \bar{k}^{body}_E + K_D \bar{w}^{body}_E \tag{5.54}$$

where $\bar{k}_E$ is the attitude error and $\bar{w}_E$ is the attitude rate error. The gains are given by:

$$K_P = I\omega_n^2 \tag{5.55}$$

$$K_D = I\omega_n^2 \zeta \tag{5.56}$$

where I is the inertia matrix. The damping ratio ζ is set to 0.707 to create a system that responds quickly and has a reasonable overshoot. The controller frequency ω_n is set to $2\pi/2000$ rad/s so that the controller is stable at the nominal 100 second step sized used. Both the desired and actual attitudes are represented by quaternions in the simulation to avoid singularity issues associated with other attitude representations. An error quaternion is calculated from these and then converted to a rotation vector. The angular rotation rate error is just the difference between the desired angular rate computed by the pointing algorithm and actual angular rate as measured by the gyros.

Chapter 6

Kalman Filter Design

The chaser will use an extended Kalman filter (EKF) to generate estimates of relative position and velocity from angle measurements [35]. There are several different varieties of Kalman filters that have been developed to deal with different types of problems and situations. The conventional Kalman filter requires a linear system. The extended Kalman filter (EKF) was developed to extend the conventional Kalman filter to deal appropriately with many non-linear systems, like the one dealt with here. There are also separate Kalman filter formulations depending on whether the system dynamics and measurements are continuous or discrete. The EKF developed here is a hybrid that uses continuous system dynamics and discrete measurements.

6.1 Overview of the Kalman Filter

Figure 6.1 is a graphical representation of the Kalman filter. A Kalman filter is used to estimate a predetermined set of system states. These states can be any variable of interest such as position, velocity, bias, etc. The Kalman filter stores the current state estimates as elements in the state vector $\hat{\mathbf{x}}$. The Kalman filter also maintains a state covariance matrix P that represents both how good the current estimate is and how changes in one state co-vary with other states. Upon initialization the Kalman filter has to be given an initial estimate of the system state $\hat{\mathbf{x}}_0$ and a

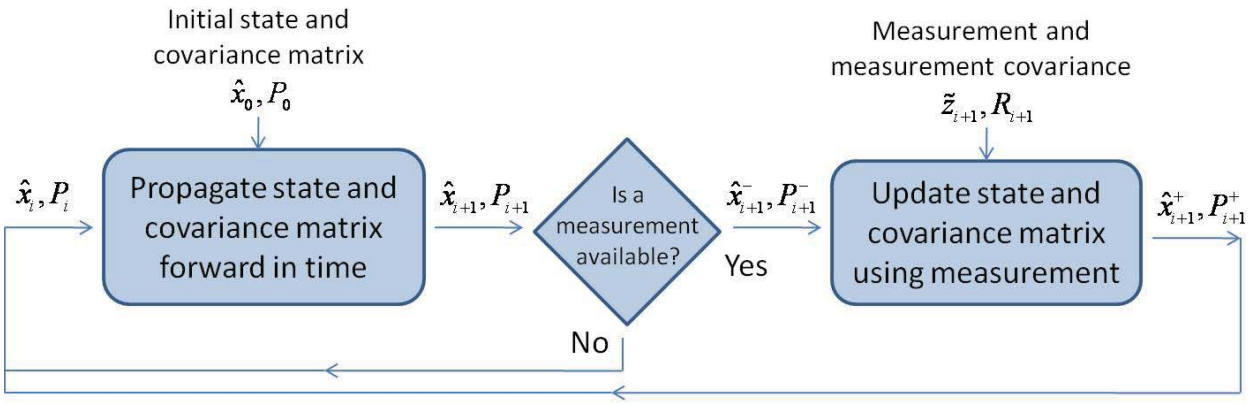

Fig. 6.1: Basic Kalman filter algorithm.

covariance matrix P_0 associated with it. The Kalman filter then updates and maintains the state estimate and covariance matrix with a two step process.The first step is to propagate the state vector and covariance matrix in time using a model of the system dynamics. As the state vector is propagated it will tend to drift away from the true state. This is due both to imperfections in the original state estimate and unknown/unmodeled effects in the system dynamics. The covariance matrix will also be propagated to reflect the reduced accuracy of the state estimates. The second step process any measurements and updates the state and covariance. The Kalman filter is given noise covariance terms to represent inaccuracies in the measurements. The filter combines the current state estimate with the information gained from the measurements to generate a new and better estimate. When generating the new estimate, the filter uses the state covariance and the sensor noise levels to weight the estimate towards the more accurate source. The Kalman filter does this in such a way that, at least for Gaussian linear systems, the resulting state estimate is optimal with respect to virtually any criterion that makes sense. The Kalman filter is summarized in Figure 6.2. More details for each of these steps will be given below.

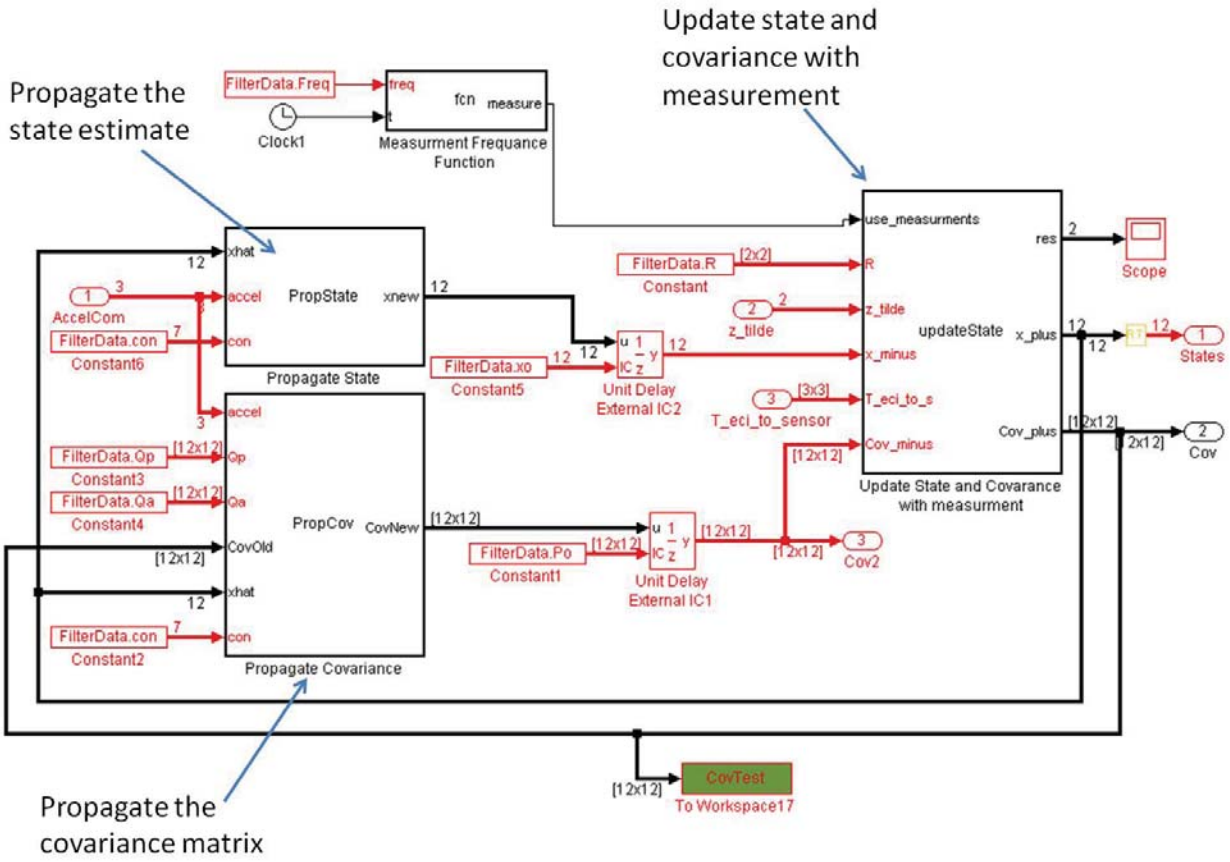

Fig. 6.2: Kalman Filter in Simulink.

6.2 Filter States and State Covariance

The EKF used here maintains the state vector:

$$\hat{\mathbf{x}} = \begin{bmatrix} \hat{\bar{r}}_c^{eci} \\ \hat{\bar{v}}_c^{eci} \\ \hat{\bar{r}}_t^{eci} \\ \hat{\bar{v}}_t^{eci} \end{bmatrix}_{12x1} \tag{6.1}$$

which is composed of the current estimate of the position of the chaser, the velocity of the chaser, the position of the target, and the velocity of the target, all in earth centered inertial (ECI) coordinates. The EKF also maintains a state covariance matrix P that represents the level of uncertainty in the state estimate. The covariance matrix P is given by:

$$P = E\left[(\mathbf{x} - \hat{\mathbf{x}})(\mathbf{x} - \hat{\mathbf{x}})^T\right] = \begin{bmatrix} \sigma_1^2 & \rho_{12}\sigma_1\sigma_2 & \cdots & \rho_{1n}\sigma_1\sigma_n \\ \rho_{12}\sigma_1\sigma_2 & \sigma_2^2 & & \vdots \\ \vdots & & \ddots & \vdots \\ \rho_{1n}\sigma_1\sigma_n & \cdots & \cdots & \sigma_n^2 \end{bmatrix} \tag{6.2}$$

where E is the expectation operator (note that here $\hat{o}$ is used to represent the estimated/expected value) and:

$$\sigma_i^2 \equiv E\left[\delta x_i^2\right] = \text{the variance of } \delta x_i \tag{6.3}$$

where $\delta x_i = x_i - \hat{x}_i =$ the error between the true state x_i and the estimated state $\hat{x}_i$ and:

$$\sigma_{ij} \equiv E\left[\delta x_i \delta x_j\right] = \text{the covariance of } \delta x_i \text{ and } \delta x_j \tag{6.4}$$

$$\rho_{ij} \equiv \frac{\sigma_{ij}}{\sigma_i \sigma_j} = \text{the correlation of } \delta x_i \text{ and } \delta x_j \tag{6.5}$$

Here it is clear that the diagonal elements represent the variance of the state estimates. For example, if σ_i is ten times as large as σ_j, then the estimate $\hat{x}_j$ is expected to be on the order of ten times as accurate as the estimate $\hat{x}_i$. The correlation ρ_{ij} tells us how the errors in x_i are correlated to x_j; i.e. if knowledge in x_i will tell us anything about x_j. The correlation ranges between -1 and 1. A positive correlation means that the two errors tend to move together, and a negative correlation means that the two errors tend to move opposed of each other. A correlation of zero ($\rho_{ij} = 0$) means that information about x_i or x_j reveals nothing about the other variable. A correlation of 1 ($|\rho_{ij}| = 1$) means $x_i$and x_j are perfectly correlated and that any information about one variable reveals just as much about the other. In other words if x_i is determined, then x_j is known just as well.

6.2.1 Filter Dynamics and Sensor Models:

The filter design is based on a set of design models. These models account for the dynamics of the chaser and target spacecraft, as well as camera measurements. Process noise is used in the velocity channel to account for any unmodeled accelerations and any uncertainties in thruster acceleration. The filter state dynamics model can be expressed as:

$$\dot{\mathbf{x}} = f(\mathbf{x}, \bar{a}_{com}) + \mathbf{w} \tag{6.6}$$

where $\mathbf{w}$ is the process noise, and:

$$f\left(\mathbf{x}, \bar{a}_{com}\right) = \begin{bmatrix} \bar{v}_c^{eci} \\ -\mu \frac{\bar{r}_c^{eci}}{|\bar{r}_c|^3} + \bar{a}_{com} \\ \bar{v}_t^{eci} \\ -\mu \frac{\bar{r}_t^{eci}}{|\bar{r}_t|^3} \end{bmatrix}_{12x1} \tag{6.7}$$

Notice that the commanded acceleration vector $\bar{a}_{com}$ in the state dynamics equation. Adding the thruster generated acceleration is important not only for accurately propagating the chaser state, but it is also essential for determining the range to the target. For example, if the chaser is station keeping directly below the target, the level of thrust required is directly related to how far the chaser

is below the target. The chaser can determine whether it is directly below the target from angle measurements, and adjust its thrust levels based on whether it is falling behind or moving ahead of the target. As the chaser position stabilizes, the required thrust should indicate how far the chaser is from the target. This is illustrated in Figure 6.3.

The sensor model can be expressed as:

$$\tilde{\mathbf{z}} = \mathbf{h}(\mathbf{x}) + \mathbf{n}_{cam} \tag{6.8}$$

Here $\mathbf{h}$ is the true relative azimuth and elevation angles as would be given by a perfect sensor and $\mathbf{n}_{cam}$ is sensor noise on the camera. Using a small angle approximation, $\mathbf{h}$ can be written as:

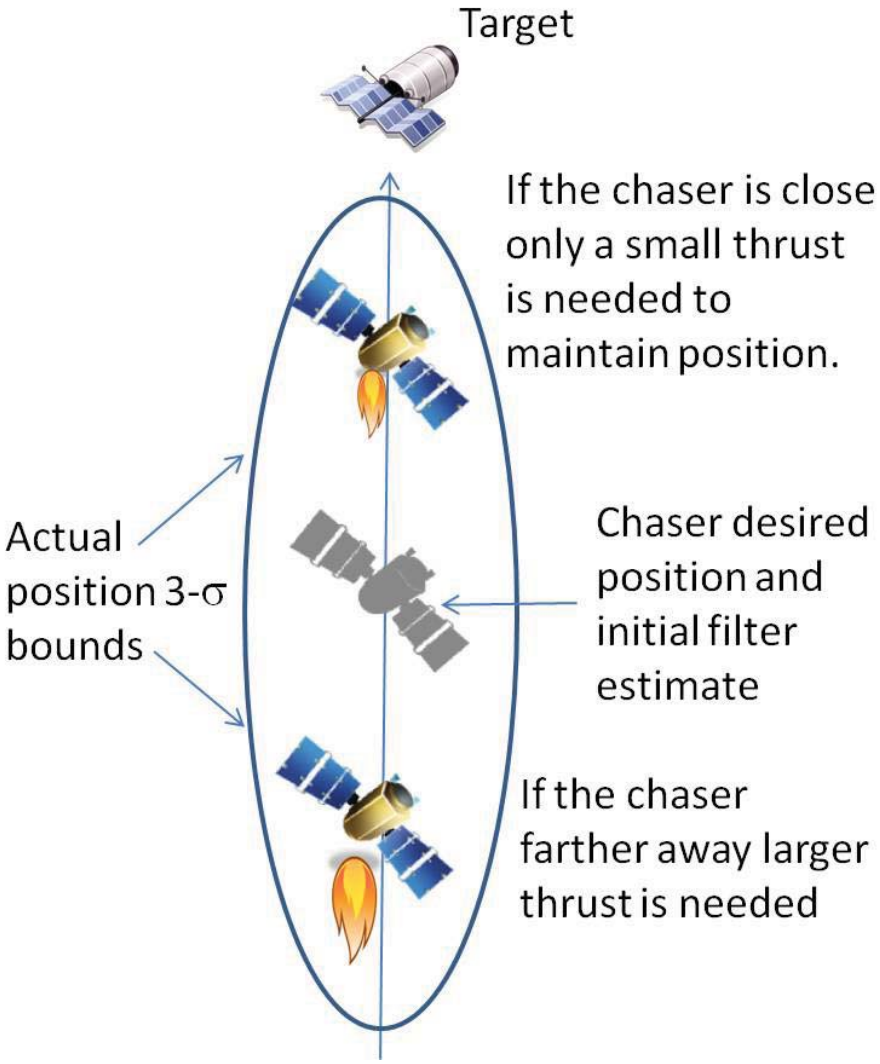

Fig. 6.3: Determining range from commanded thrust.

$$\mathbf{h} = \begin{bmatrix} \theta_{azimuth} \\ \\ \theta_{elevation} \end{bmatrix} \approx \begin{bmatrix} p_y/p_x \\ \\ p_z/p_x \end{bmatrix} \tag{6.9}$$

where $\bar{p}^{cam}$ is the relative position vector from the target to the chaser in camera fixed coordinates:

$$\bar{p}^{cam} = R_{eci \to cam}\left(r_t^{eci} - r_c^{eci}\right) \tag{6.10}$$

where the ECI to camera rotation matrix is determined from the ECI to camera quaternion:

$$R_{eci \to cam} = R_{eci \to cam}\left(q_{cam}^{eci}\right) \tag{6.11}$$

and q_{cam}^{eci} is given by the star tracker and the body to camera rotation.

6.2.2 State and Covariance Propagation

Before considering the extended Kalman filter propagation step, it is useful to take a moment to review the conventional Kalman filter propagation step. The conventional Kalman filter was derived for linear systems. These systems can be represented by the matrix equation:

$$\dot{\mathbf{x}} = F\mathbf{x} + B\mathbf{u} + G\mathbf{w} \tag{6.12}$$

where $\mathbf{x}$ is the true state $\mathbf{u}$ is the control input and $\mathbf{w}$ is process noise and $F,\ B,$ and G are specified by the associated dynamics. The same dynamic system can also be expressed in terms of a state transition matrix:

$$\mathbf{x}_{i+1} = \Phi_i \mathbf{x}_i + \int_{t_i}^{t_{i+1}} \Phi_i B\mathbf{a}\, d\tau + \int_{t_i}^{t_{i+1}} \Phi_i G\mathbf{w}\, d\tau \tag{6.13}$$

where $\triangle t$ is the discrete time step, and Φ_i is given by:

$$\Phi_i = e^{F_i \triangle t} = I + F_i \triangle t + \frac{F^2 \triangle t^2}{2!} + \frac{F^3 \triangle t^3}{3!} ..... \tag{6.14}$$

The Kalman filter state can then be propagated using either the differential equation or the state transition form of the system dynamics. If the differential form is used for state propagation,

the Kalman filter will integrate the following differential equation forward in time:

$$\dot{\hat{\mathbf{x}}} = F\hat{\mathbf{x}} + B\mathbf{u} \tag{6.15}$$

Using Equation 6.13 and the theory of stochastic processes, the state covariance can be propagated as follows:

$$P_{i+1} = \Phi_i P_i \Phi_i^T + Q_{d,i} \tag{6.16}$$

where:

$$Q_{d,i} = \int_{t_i}^{t_{i+1}} \Phi_i G \mathbf{w} G^T \Phi_i^T \, d\tau \approx GQG^T \Delta t \tag{6.17}$$

$$\Delta t = (t_{i+1} - t_i) \tag{6.18}$$

and Q is the strength of the process noise.

The dynamics represented by Equation 6.7 are not linear however. The process outlined above will have to be modified to "extend" it to a nonlinear case. The state estimate can still be propagated using the dynamic model directly. Each time step, the Kalman filter propagates its state estimate by integrating the state differential equation using a fourth-order Runge-Kutta integrator:

$$\dot{\hat{\mathbf{x}}} = f(\hat{\mathbf{x}}, \bar{a}_{com}) \tag{6.19}$$

where f is given by Equation 6.7. Propagating the covariance matrix still requires linear equations though, thus linearized system dynamics are used to propagate the covariance matrix. Using:

$$\frac{\partial}{\partial r}\left(\frac{r}{|r|^3}\right) = \frac{1}{|r|^3} I_{3x3} - r\frac{3}{|r|^4}\frac{\partial |r|}{\partial r} = \frac{1}{|r|^3} I_{3x3} + r\frac{3}{|r|^4} i_r^T = \frac{1}{|r|^3} I_{3x3} - \frac{3}{|r|^3} i_r i_r^T \tag{6.20}$$

the partial of the dynamics with respect to the state can be calculated as:

$$F = \frac{\partial f}{\partial \mathbf{x}} = \begin{bmatrix} 0_{3x3} & I_{3x3} & 0_{3x3} & 0_{3x3} \\ \frac{\mu}{|\bar{r}_c|^3}\left(3\bar{i}_c^{eci}\left(\bar{i}_c^{eci}\right)^T - I_{3x3}\right) & 0_{3x3} & 0_{3x3} & 0_{3x3} \\ 0_{3x3} & 0_{3x3} & 0_{3x3} & I_{3x3} \\ 0_{3x3} & 0_{3x3} & \frac{\mu}{|\bar{r}_t|^3}\left(3\bar{i}_t^{eci}\left(\bar{i}_t^{eci}\right)^T - I_{3x3}\right) & 0_{3x3} \end{bmatrix}_{12x12} \tag{6.21}$$

The vectors $\bar{i}_c^{eci}, \bar{i}_t^{eci}$ are the unit vectors of r_c^{eci}, r_t^{eci}, respectively. Using Equation 6.14 and the F matrix, the state transition matrix can be computed and used to propagate the state covariance matrix as in Equation 6.16.

$$P_{i+1} = \Phi_i P_i \Phi_i^T + Q_d \tag{6.22}$$

where Q_d is given in Equation 6.17.

6.2.3 State and Covariance Update

When a real measurement $\widetilde{\mathbf{z}}_i$ is received from the sensors, a predicted measurement and a Kalman gain are calculated:

$$\hat{\mathbf{z}}_i = \begin{bmatrix} \hat{p}_y/\hat{p}_x \\ \\ \hat{p}_z/\hat{p}_x \end{bmatrix}_{2x1}, \quad \hat{p} = \frac{\hat{r}_c^{cam} - \hat{r}_t^{cam}}{|\hat{r}_c - \hat{r}_t|} \tag{6.23}$$

$$K_i = P_i^- H_i^T \left(H_i P_i^- H_i^T + R_i\right)^{-1} \tag{6.24}$$

where the measurement sensitivity matrix H is given by:

$$H_i = \frac{\partial h_i}{\partial x_i} = \frac{\partial h}{\partial \bar{p}} \frac{\partial \bar{p}}{\partial x_i} = \begin{bmatrix} -\frac{p_y}{p_x^2} & \frac{1}{p_x} & 0 \\ \\ -\frac{p_z}{p_x^2} & 0 & \frac{1}{p_x} \end{bmatrix}_{3x3} T_{eci \to cam} \begin{bmatrix} -I_{3x3} & 0_{3x3} & I_{3x3} & 0_{3x3} \end{bmatrix}_{3x12} \tag{6.25}$$

The state and state covariance are then updated using:

$$\hat{\mathbf{x}}_i^+ = \hat{\mathbf{x}}_i^- + K_i \left(\widetilde{\mathbf{z}}_i - \hat{\mathbf{z}}_i\right) \tag{6.26}$$

$$P_i^+ = \left(I_{3x3} - K_i H_i\right) P_i^- \left(I_{3x3} - K_i H_i\right)^T + K_i R_i K_i^T \tag{6.27}$$

where $R = E[\mathbf{n}_{cam}\mathbf{n}_{cam}^T]$ is the variance of the camera measurements, and where the Joseph form for the update equation was chosen for its increased numerical stability over the standard Kalman Filter update equation [36].

Chapter 7

Results - Proof of Concept

To determine the effect of thrust assisted angles-only navigation on range observability several different scenarios were run. Natural motion cases are also run for comparison. The natural motion cases include football orbits, co-elliptic approaches, and V-bar station-keeping. The thrust-modified-trajectories include modified football orbits (modified speed and/or shape), modified co-elliptic approaches (non-natural approach speed and/or displaced in the cross track direction), non-V-bar station-keeping, and spiral approaches. The resulting navigation filter state uncertainties are analyzed to determine the effectiveness of low-thrust assisted angles-only navigation in determining the LOS range to target.

7.1 Metrics

The covariance matrix is used to derive 3-σ bounds on relative position. These 3-σ bounds are used as a metric to determine the quality of range information generated by the chaser. The Δv used by the chaser is also be recorded.

The covariance matrix used by the Kalman filter is used to determine how well the chaser is able to determine relative position. Relative position can be calculated from the state vector by:

$$\mathbf{x}_{rel} = H_{rel}\mathbf{x} \tag{7.1}$$

where $H_{rel} = \begin{bmatrix} I_{3x3} & 0_{3x3} & -I_{3x3} & 0_{3x3} \end{bmatrix}$. This transformation centers the coordinate system on the target. The covariance associated with this relative position estimate can be calculated as:

$$P_{rel} = H_{rel} P H_{rel}^T \tag{7.2}$$

In order to gain a more intuitive understanding of the problem $\hat{\mathbf{x}}_{rel}$ and P_{rel} are also rotated into the LVLH and boresight frames. This is done by creating a rotation matrix:

$$R_{eci\rightarrow frame} = \begin{bmatrix} \left(\bar{i}_x^{eci}\right)^T \\ \left(\bar{i}_y^{eci}\right)^T \\ \left(\bar{i}_z^{eci}\right)^T \end{bmatrix} \tag{7.3}$$

where $\bar{i}_x$, $\bar{i}_y$, and $\bar{i}_z$ unit vectors that describe either the LVLH or boresight coordinates as defined in Section 4.1. The relative states and associated covariance matrices can then be transformed in LVLH or boresight coordinates.

$$\hat{\mathbf{x}}_{rel}^{lvlh} = R_{eci\rightarrow lvlh}\hat{\mathbf{x}}_{rel}^{eci} \tag{7.4}$$

$$P_{rel}^{lvlh} = R_{eci\rightarrow lvlh}P_{rel}^{eci}\left(R_{eci\rightarrow lvlh}\right)^T \tag{7.5}$$

$$\hat{\mathbf{x}}_{rel}^{bore} = R_{eci\rightarrow bore}\hat{\mathbf{x}}_{rel} \tag{7.6}$$

$$P_{rel}^{bore} = R_{eci\rightarrow bore}P_{rel}^{eci}\left(R_{eci\rightarrow bore}\right)^T \tag{7.7}$$

The 3-σ values derived from these relative covariance matrices are used as metrics to determine the quality of relative position information obtained by the chaser's filter. It can be recalled from Section 6.2 that a covariance matrix can be represented by:

$$P = \begin{bmatrix} \sigma_1^2 & \rho\sigma_1\sigma_2 & \rho\sigma_1\sigma_2 & \cdots & \rho\sigma_1\sigma_n \\ \rho\sigma_2\sigma_1 & \sigma_2^2 & & & \vdots \\ \vdots & & \ddots & & \vdots \\ \vdots & & & \ddots & \vdots \\ \rho\sigma_n\sigma_1 & \cdots & \cdots & \cdots & \sigma_n^2 \end{bmatrix} \tag{7.8}$$

where: $\sigma_i^2 \equiv E\left[\delta x_i^2\right]$ = the variance of δx_i. Since δx_i is the error in the estimate of the state,

the standard deviation σ_i represents how close the estimate is likely to be to the true value. The standard deviation has the same units as its respective state estimate, and it can be shown that the estimate $\hat{x}_i$ will be within one standard deviation, $(\hat{x}_i - \sigma_i) \leq x_i \leq (\hat{x}_i + \sigma_i)$, approximately 68% of the time. However, rather than using the standard deviation directly here, 3-σ values are used. The 3-σ value of a variable is three times the standard deviation (3-$\sigma = 3 \times \sigma_i$). If the Kalman filter is properly constructed the estimate $\hat{x}_i$ will be within the 3-σ bounds ($\pm$3-σ) of the true value approximately 99.7% of the time

The Δv used during maneuvers is also recorded. While no attempt has been made to minimize fuel use according to any specific criterion, the Δv used should give some idea of the practicality of using these maneuvers to generate range information for fuel limited mission.

7.2 True State and Filter State Initialization

While the values of the initial conditions will vary from scenario to scenario, the method of generating them will largely stay the same. Let $\hat{\mathbf{x}}_c^{eci}$ represent the estimate of chaser's state (position and velocity) and $\hat{\mathbf{x}}_t^{eci}$ be the estimate of the target's initial state. Also let $\hat{\mathbf{x}}_{rel}^{eci} = \left(\hat{\mathbf{x}}_t^{eci} - \hat{\mathbf{x}}_c^{eci}\right)$. The initial estimate of the target state in ECI coordinates $\hat{\mathbf{x}}_t^{eci}$ is a given point (position and velocity) in geosynchronous orbit. The desired initial relative position and velocity (the relative state the controller will try and drive the system to) as observed and coordinatized in LVLH, referred to here as $\hat{\mathbf{x}}_{des}^{lvlh}$, is determined by the scenario that will be run. This is either a constant desired relative position and velocity for a station-keeping mission or the desired relative position an velocity of the first point of a nominal relative trajectory.

To determine the initial filter state, the initial desired relative state is transformed into ECI coordinates using $\hat{\mathbf{x}}_{des}^{eci} = T_{lvlh \to eci} \hat{\mathbf{x}}_{des}^{lvlh}$ where the transformation matrix is defined as outline in Section 4.1. Then, the initial chaser state estimate used by the filter is given by:

$$\hat{\mathbf{x}}_c^{eci} = \hat{\mathbf{x}}_t^{eci} + \hat{\mathbf{x}}_{des}^{eci} \tag{7.9}$$

The covariances for the target and chaser are also initially defined in LVLH. Standard deviations σ_i^{lvlh} and correlations ρ_{ij}^{lvlh} are selected according to the scenario and are used to populate the state covariance matrix P_c^{lvlh} and P_t^{lvlh}. These covariance matrices are then transformed into ECI coordinates using:

$$P_{c/t}^{eci} = T_{lvlh \to eci} P_{lvlh} \left(T_{lvlh \to eci}\right)^T \tag{7.10}$$

The initial filter state estimate and state covariance are then given by:

$$\hat{\mathbf{x}} = \begin{bmatrix} \hat{\mathbf{x}}_c^{eci} \\ \\ \hat{\mathbf{x}}_t^{eci} \end{bmatrix} \tag{7.11}$$

$$P = \begin{bmatrix} P_c^{eci} & 0_{6x6} \\ \\ 0_{6x6} & P_t^{eci} \end{bmatrix} \tag{7.12}$$

True states are then generated by adding random error to the estimated states. These random errors must be selected so that the true states will lie in their respective covariance ellipses in a way that would be expected by the probabilistic definition of the covariance matrix. Any covariance matrix is diagonal when coordinated in a principle axis. Here that frame will be referred to as a "prime" frame. The axes of a prime frame are the eigenvectors of the respective covariance matrix. A rotation from ECI to the prime frame can be written as:

$$T_{eci \to prime} = \begin{bmatrix} \left(\bar{e}_1^{eci}\right)^T \\ \\ \left(\bar{e}_2^{eci}\right)^T \\ \\ \vdots \\ \\ \left(\bar{e}_n^{eci}\right)^T \end{bmatrix} \tag{7.13}$$

where $\bar{e}_1$, $\bar{e}_2$, ... $\bar{e}_n$ are the unit eigenvectors of the covariance matrix. Let ϵ_1, ϵ_2, ... ϵ_n be the eigenvalues associated with the eigenvectors. To generate a set of random state errors, a random vector with a mean of zero and a variance of one is created. Each element is then multiplied by one of the eigenvalues. This creates an random vector, $\mathbf{x}_{error}^{prime}$ that lies appropriately in the covariance ellipse in the prime frame. This vector is then rotated into inertial coordinates using:

$$\mathbf{x}_{error}^{eci} = \left(T_{eci \to prime}\right)^T \mathbf{x}_{error}^{prime} = T_{prime \to eci} \mathbf{x}_{error}^{prime} \tag{7.14}$$

The true states of the chaser and target are then calculated using:

$$\mathbf{x}_c^{eci} = \hat{\mathbf{x}}_c^{eci} + \mathbf{x}_{c,error}^{eci} \tag{7.15}$$

$$\mathbf{x}_t^{eci} = \hat{\mathbf{x}}_t^{eci} + \mathbf{x}_{t,error}^{eci} \tag{7.16}$$

7.3 Process Noise

When studying orbital relative motion, adding acceleration perturbation in the form of process noise to one spacecraft is equivalent to putting a lesser amount of noise on both spacecraft[6]. It was empirically determined that adding zero-mean white process noise with a covariance matrix: $Q_d = (1.014\mu m/s^2)^2 I_{3x3}$ on the velocity of the target every 100 s causes the relative position to increase by approximately 300 m 3-σ every orbit if uncorrected by measurements. This was done by running the simulation with zero initial errors and an zero initial filter covariance. The line of sight camera was turned off so that the resulting state covariance would be purely the result of the filter process noise. This process noise was then selected so that after 5 days simulation time the final filter covariance would have 1500 m 3-σ in its local horizontal direction.

Figure 7.1 shows that uncertainty in the local horizontal direction increases much faster than in the cross-track or local vertical direction. Based on orbital mechanics, this is as to be expected. The process noise is just as likely to create a disturbance in any direction; however, once there is some uncertainty in the local vertical direction there is a possibility that the target is in a higher or lower orbit that the current estimate. If the target is in a higher or lower orbit it will gradually fall behind or move ahead of the estimated position because lower orbits move faster than higher ones. This can be observed mathematically using the CW equations.

It can be clearly seen from 4.30 through 4.35 that any differences between the estimate and actual state will create cyclic or constant errors in that are bounded by the size of the initial error. However, the equation for local horizontal position $x(t)$ has a term $[6\omega z_0 + 3\dot{x}_0]\,t$ that is that is proportional to time. Thus an error in the estimate of either z_0 or $\dot{x}_0$ will create secular error in the estimate of $x(t)$. In Figure 7.1 the gradual accumulation of uncertainty in the local vertical direction due to process noise then creates a constantly growing uncertainty in the local horizontal direction that quickly outpaces the magnitude of the uncertainty for the other states.

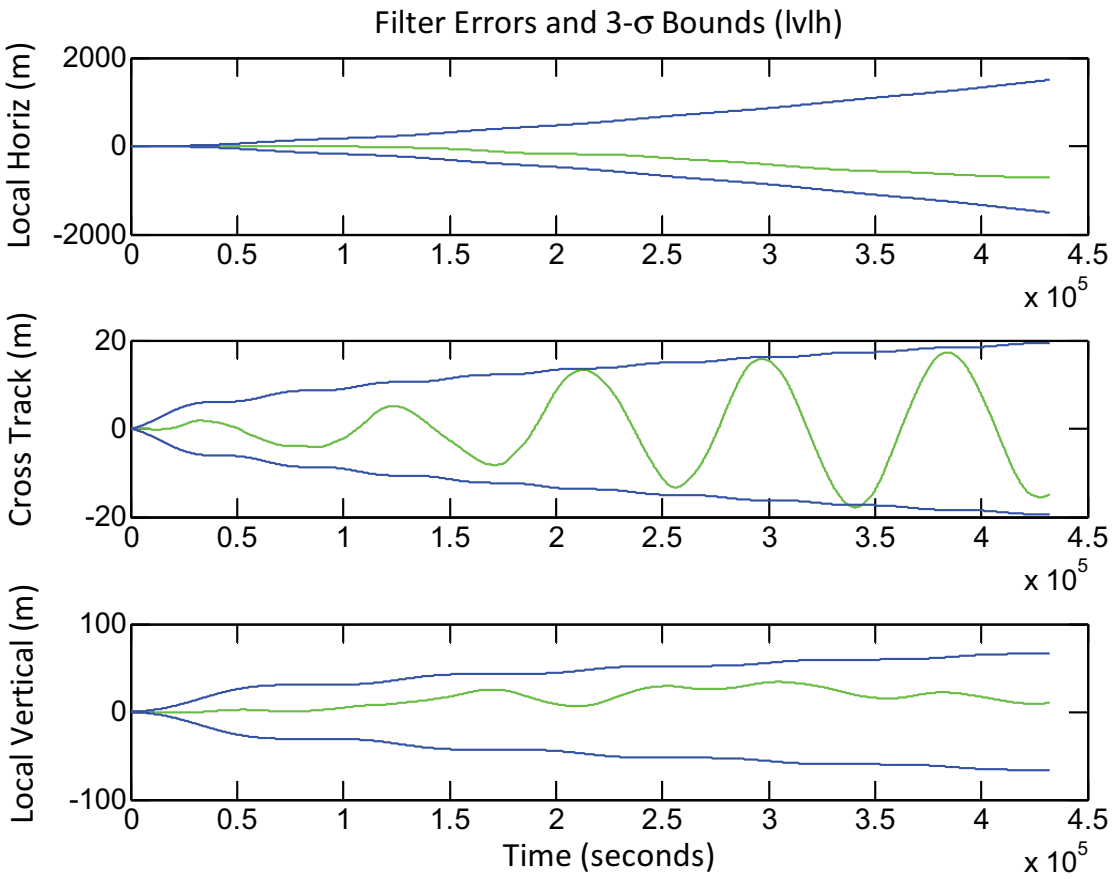

Fig. 7.1: Filter errors and 3-σ bounds while station-keeping 500m behind over 5 days (no measurements).

7.4 LQR Weights

As explained in Section 5.5, the LQR control law is created by selecting maximum allowed position and velocity errors and maximum allowed control accelerations. The goal in setting the weights for the LQR controller is to stay as close a possible to the desired trajectory, while not waisting to much Δv tracking noise.

For the scenarios studied below, the maximum desired acceleration was generally set to be a little larger than the thrust levels that would be needed to perform the desired maneuvers. The maximum allowable position error was set to be on the same order as the position uncertainty for most of the run. The allowable maximum velocity was then set to $max\, v_{rel,i} = \sqrt{(max\, r_{rel,i})\,(max\, a_i)}$.

A notable exception to the above method is the second fixed throttle case in Section 7.6.2. Because of the relatively high minimum thrust in that case the $max\, a_i$ had to be raised quite a bit in order to maintain a similar position error to the other station-keeping cases. This was necessary

so that the commanded acceleration would be higher than the thruster minimum impulse.

Some trial an error was used in selecting these parameters. Each case was first run with a low gain, low bandwidth controller. The case would then be re-run with higher and higher bandwidth controllers until theΔv started increasing significantly due to noise tracking. The values of the LQR weights for each scenario are summarized in Table 7.1.

Table 7.1: LQR Controller Parameters

Scenario	$max\, r_{rel,i}$	$max\, v_{rel,i}$	$max\, a_i$
V-bar Station-Keeping	$20\,m$	$0.02\,m/s$	$20\,\mu m/s^2$
Below Station-Keeping (Throttleable)	$20\,m$	$0.02\,m/s$	$20\,\mu m/s^2$
Below Station-Keeping (Low Minimum Impulse)	$20\,m$	$0.02\,m/s$	$20\,\mu m/s^2$
Below Station-Keeping (High Minimum Impulse)	$20\,m$	$2\,m/s$	$0.002\,m/s^2$
Natural Football	$10\,m$	$0.001\,m/s$	$0.1\mu m/s^2$
Accelerated Football	$10\,m$	$0.01\,m/s$	$10\,\mu m/s^2$
Rounded Accelerated Football	$10\,m$	$0.0032\,m/s$	$1\,\mu m/s^2$
Forced Linear Approach	$10\,m$	0.0316	$10\,\mu m/s^2$
Spiral Approach	10	$0.01\,m/s$	$10\,\mu m/s^2$

7.5 Other Important Parameters

Unless otherwise stated all scenarios used the parameters given in Table 7.2.

7.6 Station-Keeping

Missions often require one spacecraft to station-keep with respect to another. If the chaser's station-keeping position is not on the targets V-bar, then a small amount of thrust will be required to maintain position. Here it will be shown that this thrust can make range to the target detectable. It will also be shown that while angle measurements alone cannot generate new range information without some sort of thrust, they can slow the growth of the range covariance by helping to better estimate relative velocity.

7.6.1 V-bar Station-Keeping

In the first scenario the chaser is commanded to station-keep 500 m behind (local horizontal)

Table 7.2: Simulation Parameters

Parameter	Units
Integration step size	100 s
Optical camera process noise	3 $mrads$ 3-σ/axis
Optical camera bias	0 $mrads$ 3-σ/axis
Star-camera noise	0 $mrads$ 3-σ/axis
Gyro noise	0 $deg/\sqrt{hr}$ 3-σ/axis
Thruster noise strength	0 m^2/s^3 3-σ/axis
Dynamics process noise strength	$1.0282 \times 10^{-14} m^2/s^3$ 3-σ/axis
Gravitational constant	398600 km^3/s^2
Filter Propagation step size	100 s
Measurement frequencies	100 s

the target. Because the chaser is on the V-bar, thrust is needed only to correct position and velocity errors. In this example the initial relative position errors are 75 m 3-σ in the local horizontal direction, 3 m 3-σ in the cross track and local vertical directions, and the velocity errors are 3 cm/s 3-σ in each component of velocity.

Even though the filter starts with a good estimate of relative cross-track and local-vertical directions, it is able to improve its estimate in these directions very quickly because these directions are perpendicular to line-of-sight. Figure 7.2 shows the cross-track filter error and 3-σbounds for the first 10,000 seconds of the simulation. For the first 100 seconds the variance and estimate increase due to process noise. However, after the first angle measurement at 100 seconds the filter is able to quickly refine its estimate in this direction. Figure 7.3 shows all three components of the filter error.

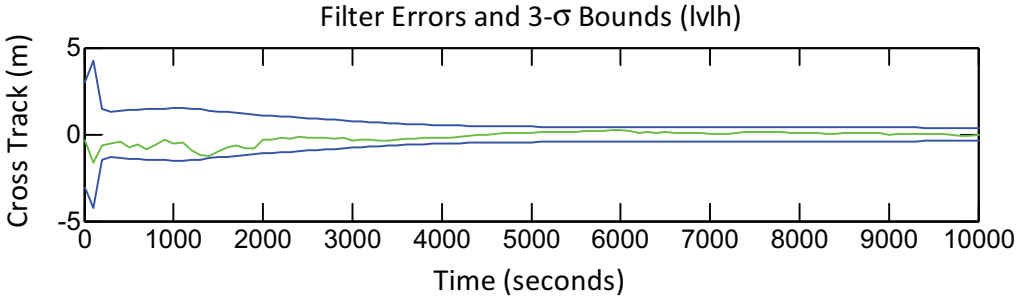

Fig. 7.2: Cross-track filter position error and 3-σ bounds while station-keeping 500m behind.

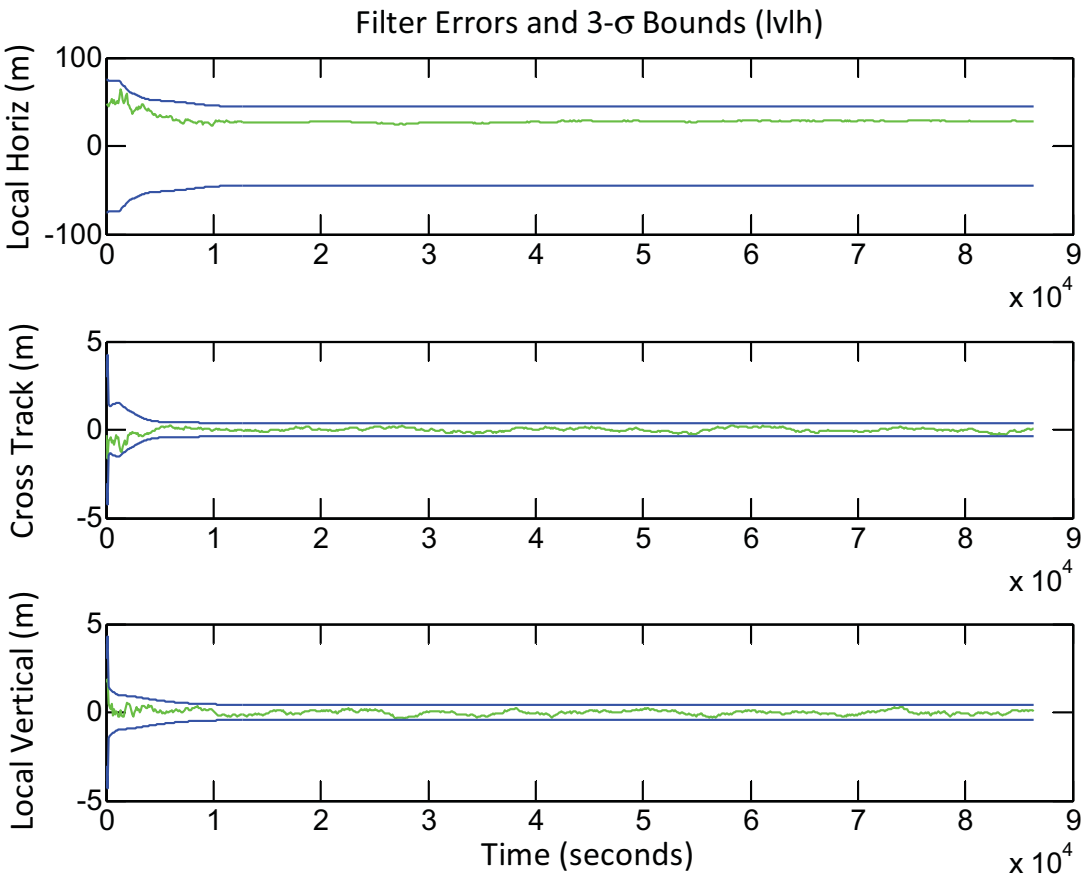

Fig. 7.3: Filter position errors and 3-σ bounds while station-keeping 500m behind over 24 hours.

Because the filter can detect errors in non-boresight directions, the chaser uses some thrust to correct initial errors. Figure 7.4 shows small but significant accelerations due to these corrections. After these initial errors are corrected, the thruster acceleration drops almost to zero as would be expected for V-bar station-keeping. Because the chaser is executing small correction maneuvers at the beginning of the simulation, the filter is able to glean some range information. As can be seen in Figure 7.3, the local-horizontal 3-σ decreases a little at the very beginning of the simulation. However once the chaser stops thrusting to correct initial errors at about 10,000 seconds into the simulation the filter stops gaining any more information in this direction.

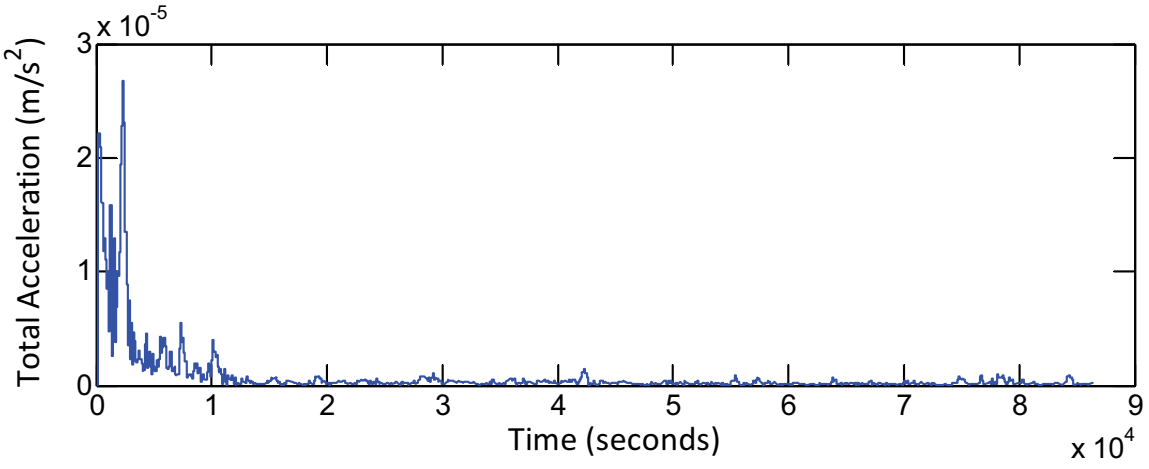

Fig. 7.4: Total acceleration while station-keeping 500m behind over 24 hours.

Even though the filter is not able to reduce the LOS 3-σ bounds after the initial improvements, it is able to keep the range 3-σ bounds from growing significantly. This is because whereas only two relative position states are detectable, all three relative velocity states are detectable. Figure 7.5 shows that the filter is able to estimate all elements of relative velocity. Cross-track and local-vertical can of course be detected by measuring the resulting change in cross-track and local-vertical position. Similarly, a different velocity in the relative local-horizontal direction means the target is in an orbit with a different eccentricity. This different eccentricity means that the target will soon be moving in the local-vertical direction relative to the chaser, making local-horizontal velocity detectable.

Table 7.3 summarizes the results of this scenario. The filter was able to significantly improve the initial estimation of all relative states except for local-horizontal position. However, even in this case, the filter was able to keep the error in its estimate from growing too much due to the accuracy of the horizontal velocity estimate.

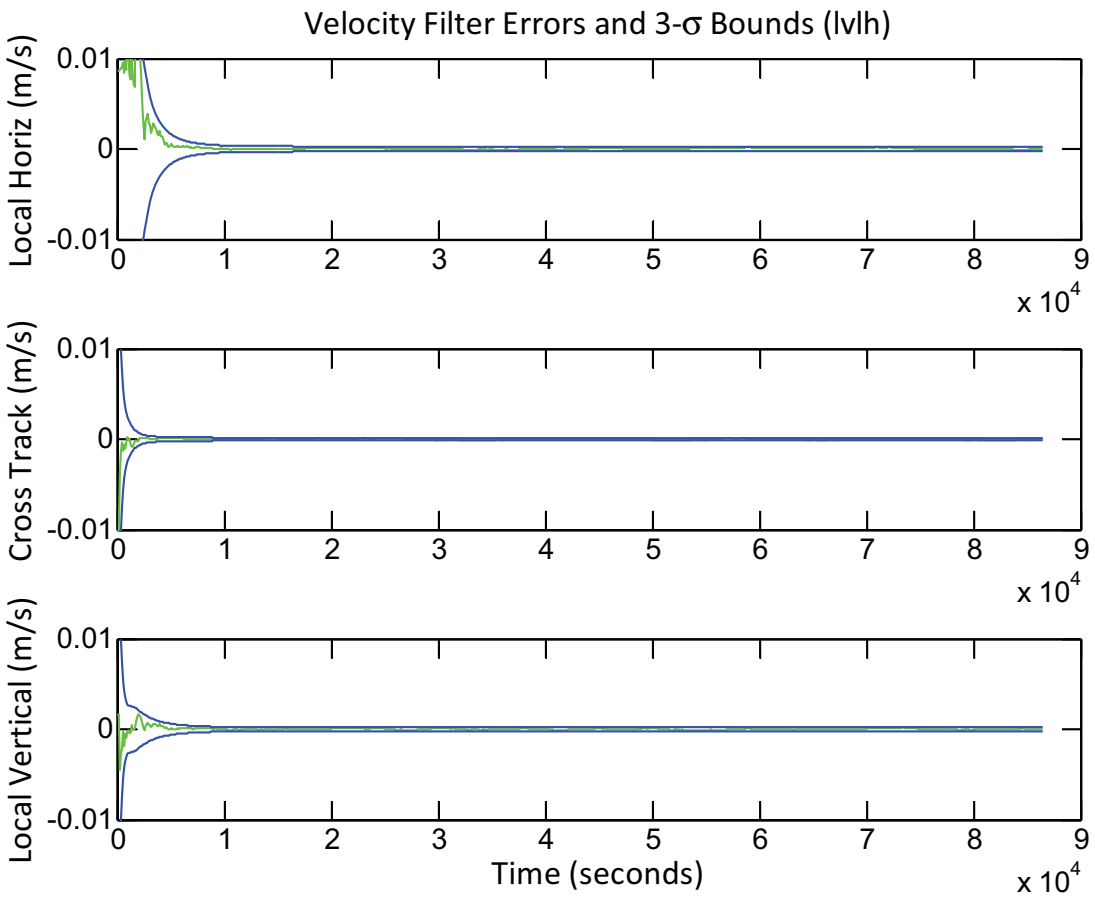

Fig. 7.5: Filter velocity errors and 3-σ bounds while station-keeping 500m behind over 24 hours.

Table 7.3: Filter Error 3-σ Bounds While Station-Keeping 500 Meters Behind for 24 Hours

	Initial	**After 24 hr**
Horizontal 3-σ Bounds (m)	75	45
Cross-track 3-σ Bounds (m)	3	0.4
Vertical 3-σ Bounds (m)	3	0.4
Horizontal Velocity 3-σ Bounds (m/s)	0.03	0.0003
Cross-track Velocity 3-σ Bounds (m/s)	0.03	0.0002
Vertical Velocity 3-σ Bounds (m/s)	0.03	0.0002
Δv (m/s)	—	0.07

To further investigate the ability of relative angle measurements to control covariance growth the above scenario was re-run, but this time the LOS camera was shut off at 10,000 seconds simula-

tion time. Figure 7.6 shows that as soon at the camera is turned off the filter estimate 3-σ bounds begin to grow like they did in the no measurements scenario.

7.6.2 Station-Keeping Below

If the chaser is commanded to station-keep 500 m below (local vertical) the target, it will require a small thrust to hold its position. This displacement allows range information to be extracted from angle measurements. In this scenario the initial relative position errors are 75 m 3-σ in the local vertical direction, 3 m 3-σ in the cross track and local horizontal directions, and the initial velocity errors are 3 cm/s 3-σ in each component of velocity. The thrust profile for this case is illustrated in Figure 7.7. The initial thrust is on the order of 10-35 um/s^2 as the controller corrects the initial random errors. After about 10,000 seconds the thrust stabilizes to about $8um/s^2$.

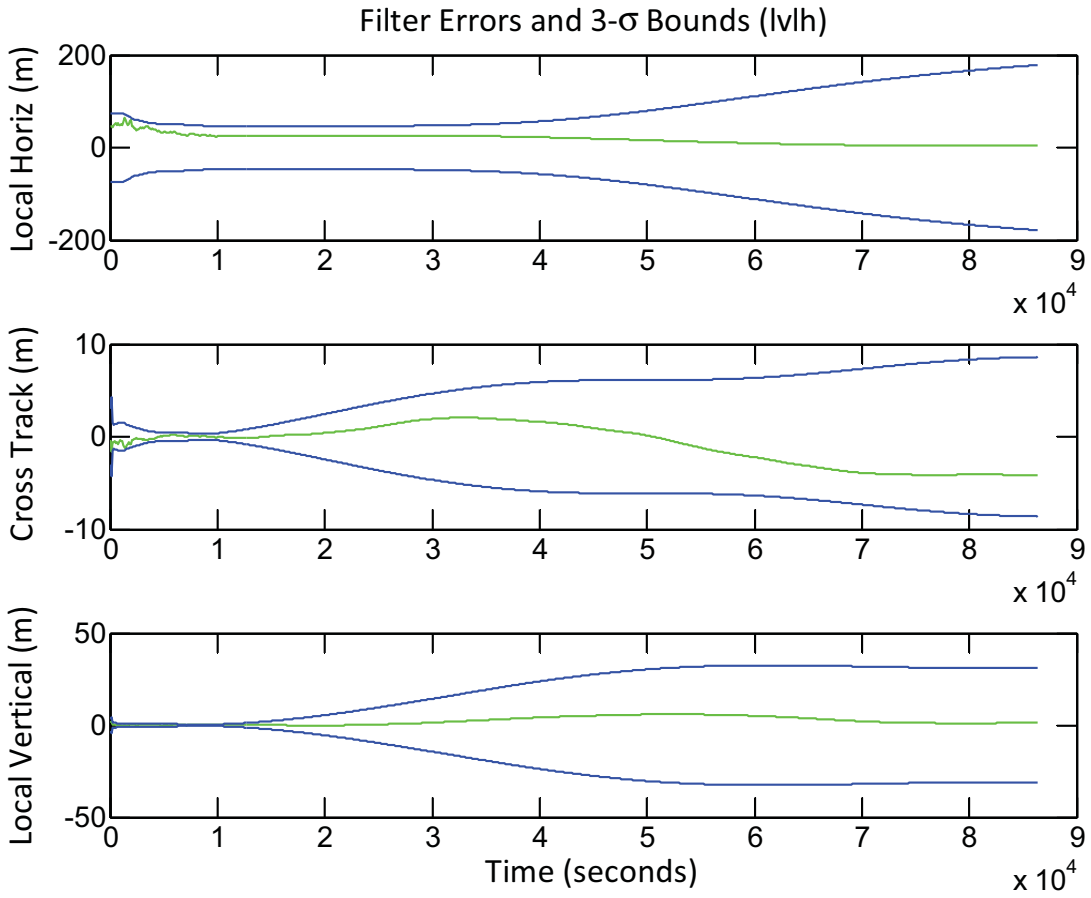

Fig. 7.6: Filter position errors and 3-σ bounds (24 hr) while station-keeping 500m behind.

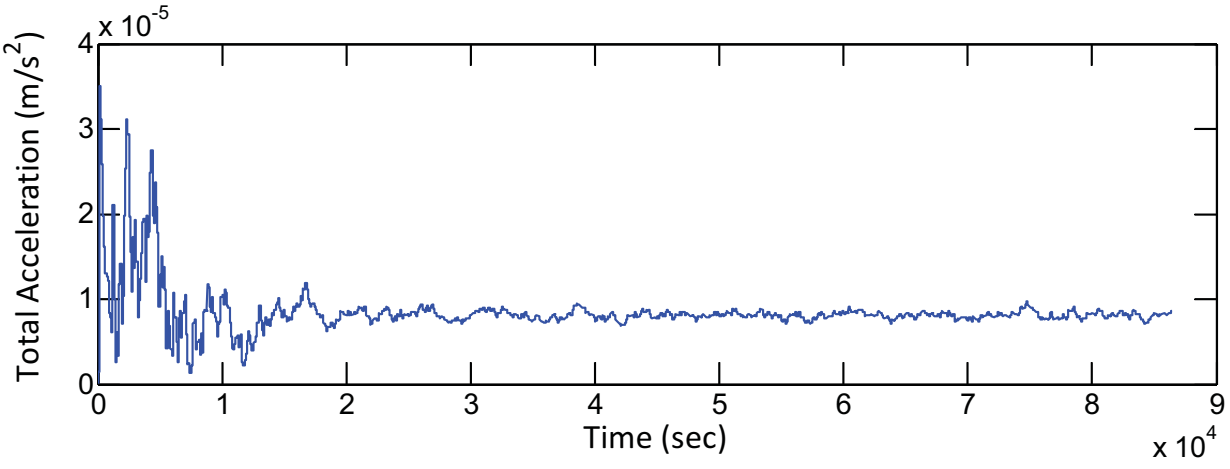

Fig. 7.7: Thruster acceleration (24 hr) while station-keeping 500m below.

Figure 7.8 shows how the filter errors and 3-σ error bounds evolve over the first 7200 seconds (2 hours) of the simulation.

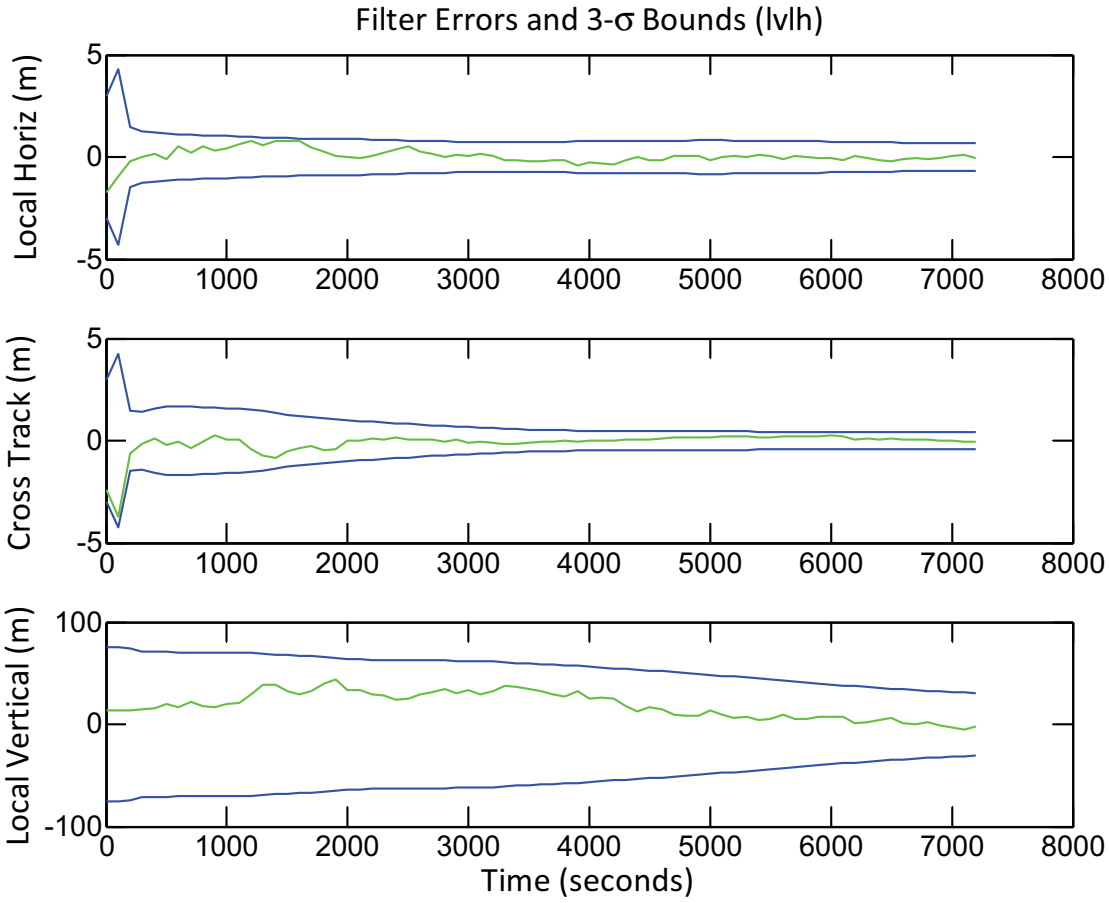

Fig. 7.8: Filter errors and 3-σ bounds (2 hr) while station-keeping 500m below.

The errors and uncertainty in the local horizontal and cross track direction drop very dramatically after the first relative angle measurement. This is expected since relative position in these directions can be directly calculated from angle measurements. Relative range, which in this case happens to be in the local vertical direction, takes longer to determine, but the filter is able to gradually remove errors and uncertainty here as well, though at this point they still may be largely due to the initial error correcting thrust. However, as time goes on, the filter continues to refine its estimates as it receives additional measurements as shown in Figure 7.9. In this case, the range uncertainty stabilizes at less than 1 percent of the total range after about 10 hours of station-keeping. The filter can then maintain this level of range knowledge indefinitely as long as the chaser is continuing to thrust and hold this position. This is illustrated in Figure 7.10. A comparison of the final errors is shown in Table 7.4.

Table 7.4: Filter Error 3-σ Bounds While Station-Keeping 500 Meters Below for 24 Hours

	Initial	**After 2 hr**	**After 24 hr**
Vertical Error (m)	75	23	4
Cross-track Error (m)	3	0.4	0.4
Horizontal Error (m)	3	0.6	0.5
Δv (m/s)	—	0.17	0.80

Thus far every scenario has been run with variable throttle thrust. This means the chaser's thrusters are able to provide any level of thrust commanded by the flight computer. The above simulation was repeated with two levels of fixed throttle thrusters instead of variable throttle thrusters. The first had a minimum impulse of 1 mm/s and the second has a minimum impulse 10 cm/s. The

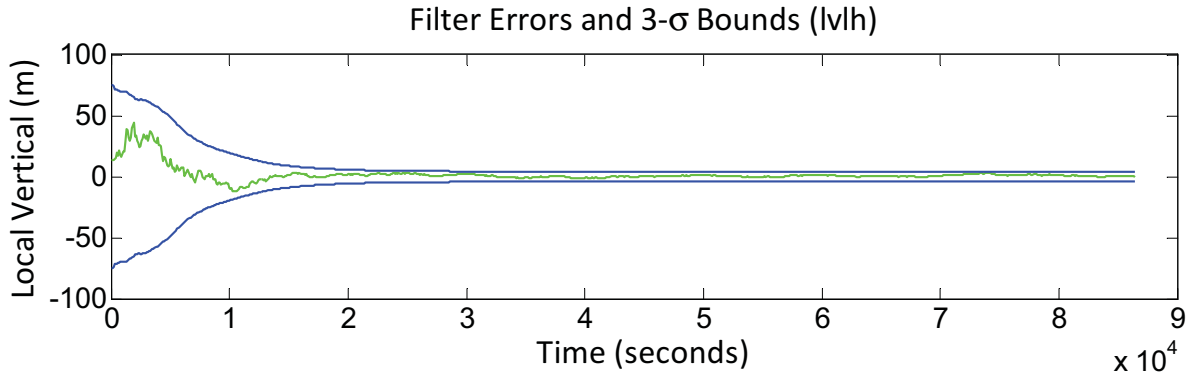

Fig. 7.9: Local-vertical filter errors and 3-σ bounds while station-keeping 500m below over 24 hours.

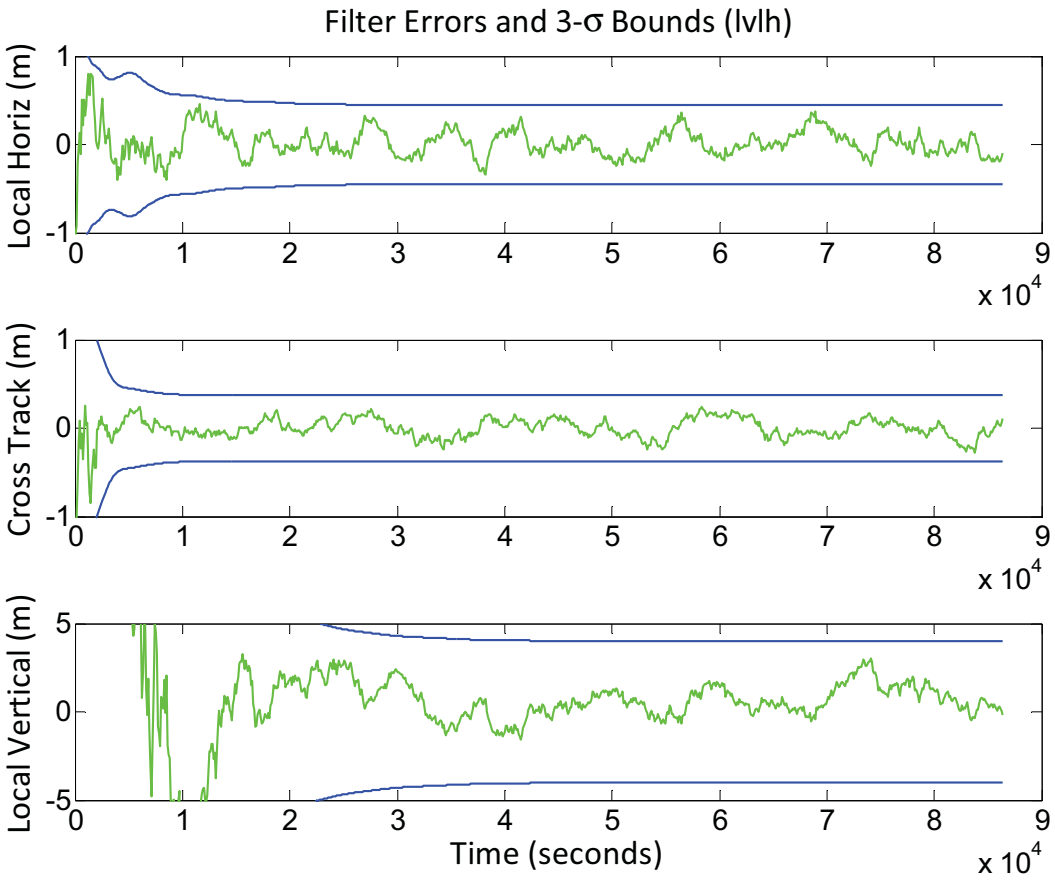

Fig. 7.10: Filter errors and 3-σ bounds while station-keeping 500m below over 24 hours.

initial state and uncertainties were exactly the same as the above case. The variable thrust and the two fixed thrust cases all produced very similar range detectability characteristics. Figure 7.11 and Table 7.5 show that the low minimum impulse case is nearly identical to the variable thrust case. The higher minimum impulse requires more Δv to maintain position, and the time history of the LOS 3-σ error bounds has a jagged appearance since each high impulsive thrust generates more range information, but the uncertainty then grows as the chaser coasts between impulsive maneuvers. Nonetheless, the 3-σ error bounds for the high impulsive case are still very close to the variable and low impulsive cases.

Table 7.5: Filter Error 3-σ Bounds While Station-Keeping 500 Meters Below for 6 Hours (Variable vs Fixed Thrust)

			Fixed Thrust	
	Initial Error	**Variable Thrust**	**Low Minimum Impulse**	**High Minimum Impulse**
Vertical Error (m)	75	5.2	5.3	5.0
Cross-track Error (m)	3	0.4	0.4	0.4
Horizontal Error (m)	3	0.5	0.4	0.4
Δv (m/s)	—	0.21	0.2	12

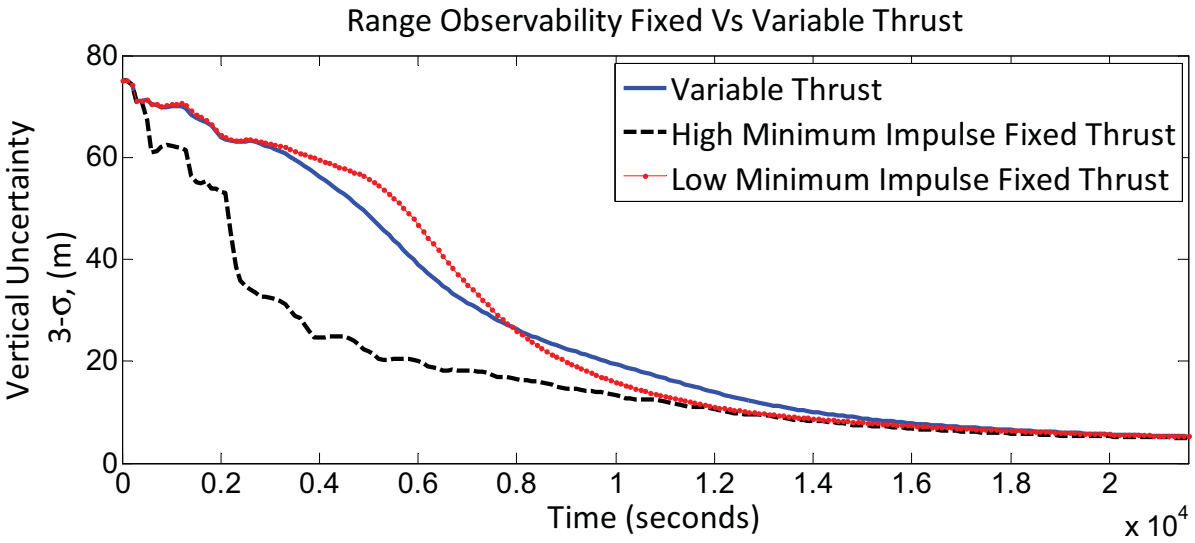

Fig. 7.11: Filter error 3-σ bounds while station-keeping 500m below over 6 hours (variable vs. fixed thrust).

Table 7.6 shows that these results still hold when the simulation is run for longer periods of time. After 24 hours of simulation time all the relative position information from all three thrust types is almost identical. The only real difference between these cases is the much higher Δv for the 10 cm/s minimum impulse case. Since there seems to be no significant difference in navigation performance between the low impulsive and variable thrust cases, only the variable thrust case will be considered in further cases.

Table 7.6: Filter Error 3-σ Bounds While Station-Keeping 500 Meters Below for 24 Hours (Variable vs Fixed Thrust)

			Fixed Thrust	
	Initial Error	**Variable Thrust**	**Low Minimum Impulse**	**High Minimum Impulse**
Vertical Error (m)	75	4	4	4
Cross-track Error (m)	15	0.4	0.4	0.4
Horizontal Error (m)	15	0.4	0.5	0.4
Δv (m/s)	—	0.73	0.73	44

7.7 Football Orbits

Many mission may require the chaser to move around the target in some manner. It may be necessary to look at multiple side of the target for an observation/inspection mission, or to get on the same side as a port for a docking/service operation. Football orbits can be very useful for these situations. They can also be useful for staying in the general area of the target with out using much fuel.

7.7.1 Natural Football Orbit Motion

In Figure 7.12 the chaser is in a football orbit around the target starting 250 meters below the target in the local vertical direction. The initial chaser 3-σ errors are 30 m in the local vertical direction and 3 m in the cross-track and local horizontal directions. The initial velocity errors are 6 mm/s 3-σ in every direction. The thrusters were turned off for this first case. Due to the initial errors and process noise, the chaser did not come back to the initial position after one orbital period as it would in the ideal case. As can be seen in Figure 7.13, no range information was gained in this case.

The same case was run again but the chaser was allowed to use its thrusters to correct trajectory errors as indicated by the navigation filter. Using about 6 mm/s of Δv, the chaser was able to follow an almost perfect football orbit around the target. As can be seen in Figure 7.14, most of the Δv was expended at the beginning of the run to counteract the initial trajectory error. The final line-of-sight filter error in this case is 24 m 3-σ which is slightly less than the previous case. This is again due to orbit correction generating range information.

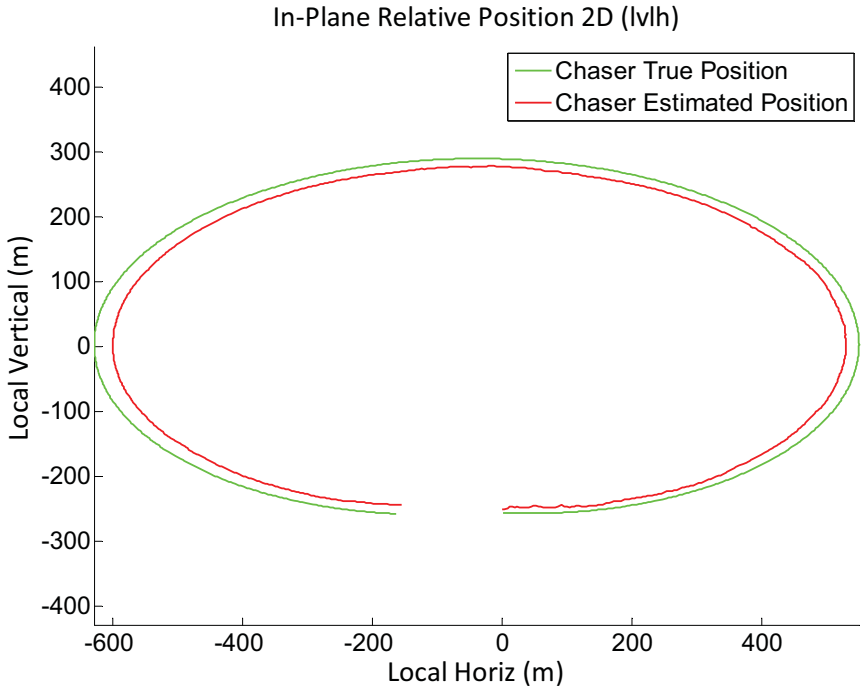

Fig. 7.12: A natural football orbit (no thrust) with errors.

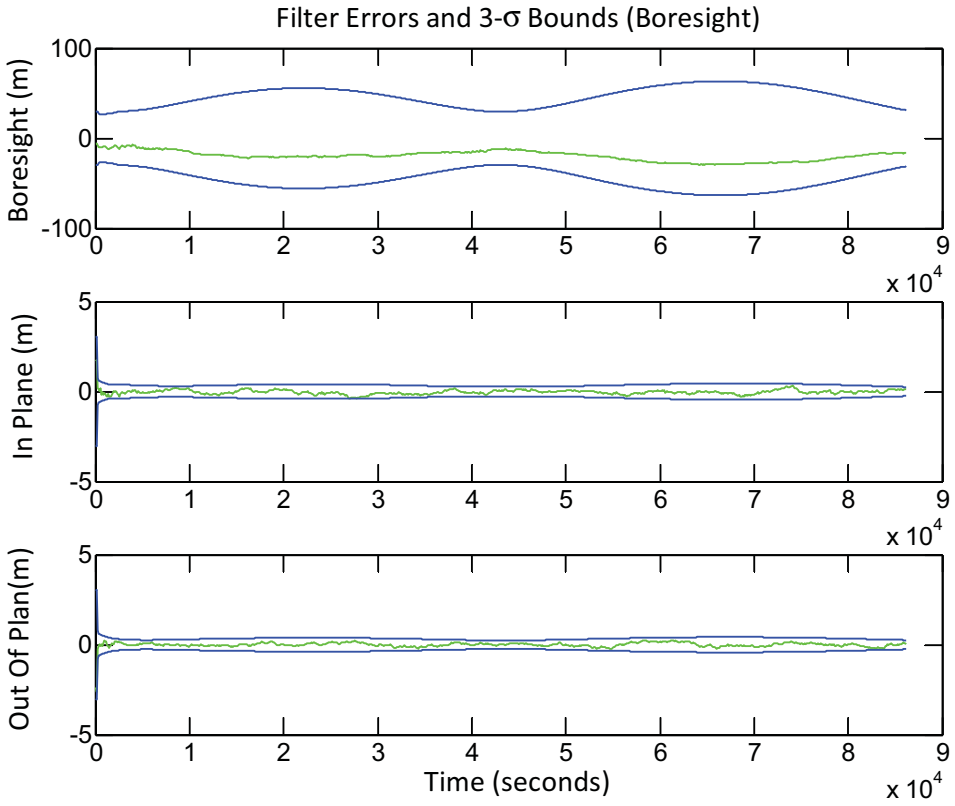

Fig. 7.13: Filter errors and 3-σ bounds while in a football orbit (no thrust).

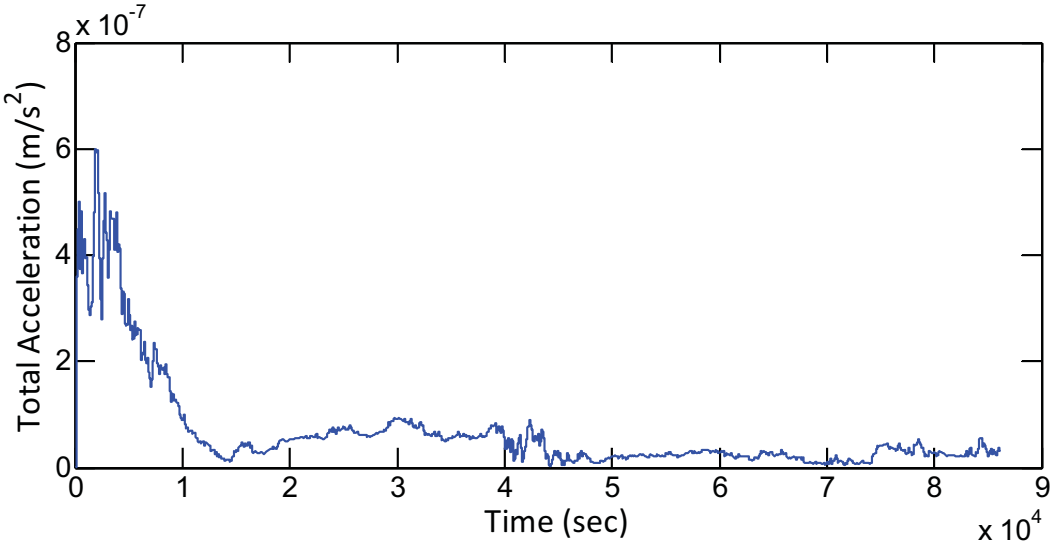

Fig. 7.14: Corrective thrust for a football orbit with small initial uncertainty.

To further investigate the range information gained by correcting initial errors, another case was run with a larger initial velocity error, 60 mm/s 3-σ. The only difference between this run and the last is the greater uncertainty in initial velocity. Figure 7.15 shows that the chaser used a maximum thrust about 10 times greater than in the previous case to correct trajectory errors due to initial uncertainty. These higher levels resulted in a line-of-sight filter error of only 9.6 3-σ. Figure 7.16 and 7.17 show that the 3-σ error bounds dropped significantly at the beginning while the chaser was experiencing the largest thrust. Once the initial errors were removed and the thrust levels dropped to near zero, the uncertainty stopped improving and started increasing.

Table 7.7: Boresight Error 3-σ Bounds and Δv After One Football Orbit (Various Initial Uncertainty and Thrust Levels)

	Final Error			
	Small Initial Uncertainty With No Thrust	**Small Initial Uncertainty With Thrust**	**Large Initial Uncertainty With Thrust**	**Small Initial Uncertainty Forced Motion**
Bore-sight Error 3-σ (m)	31	24	9.6	3.4
Δv (m/s)	0	0.006	0.04	0.1

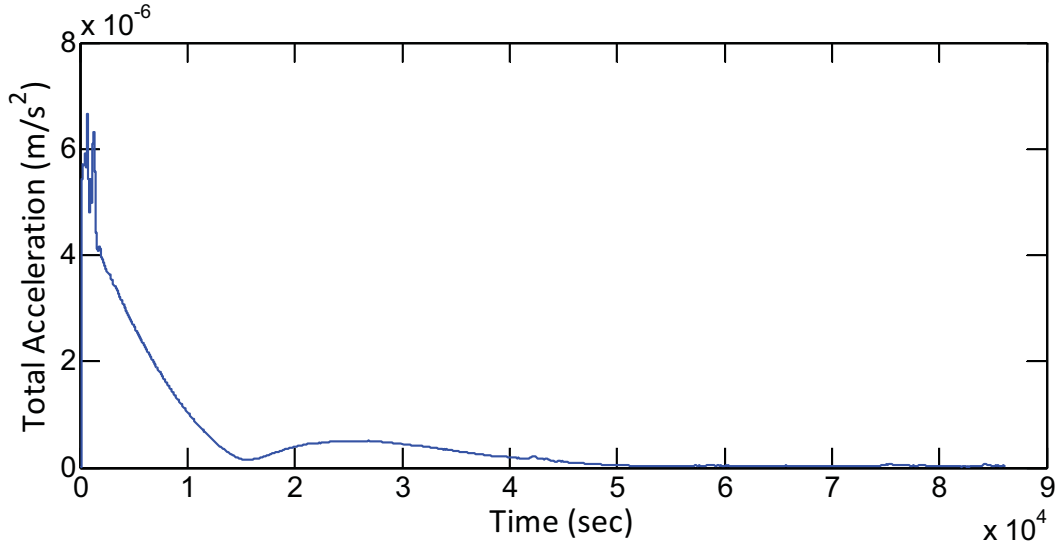

Fig. 7.15: Corrective thrust for a football orbit with large initial uncertainty.

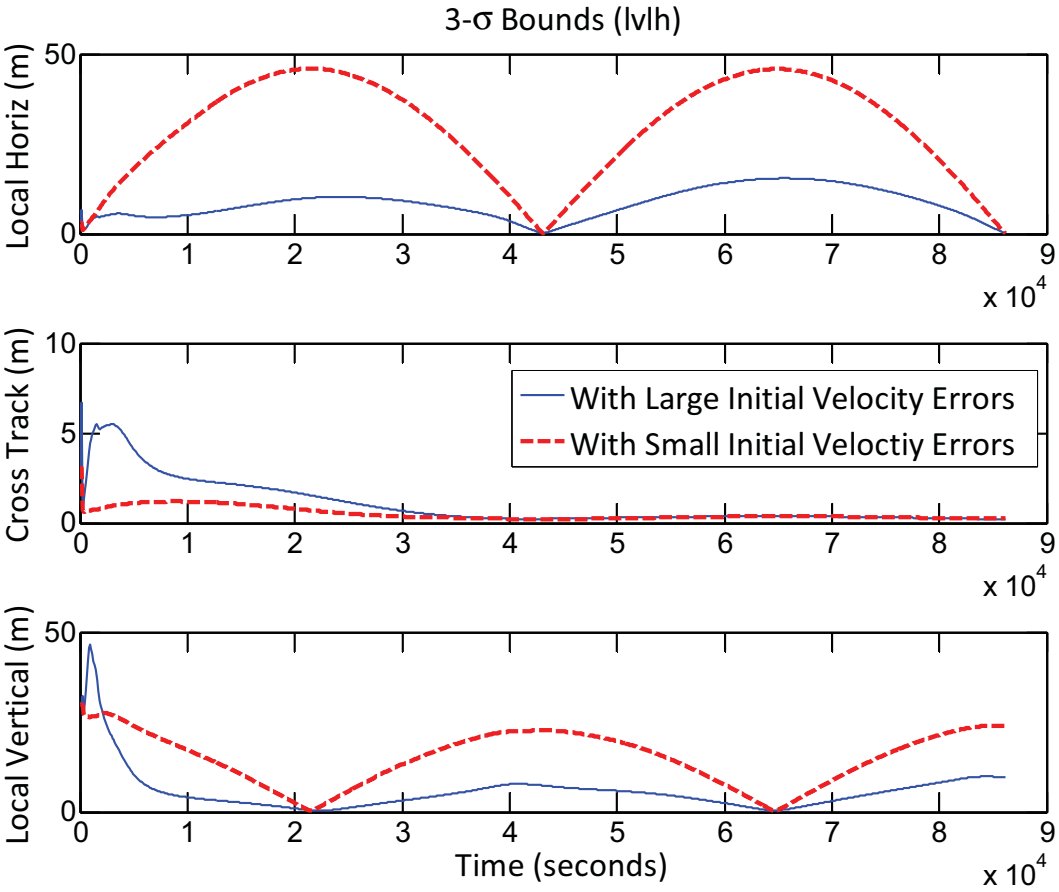

Fig. 7.16: Filter error 3-σ bounds while in a football orbit(lvlh, large initial uncertainty).

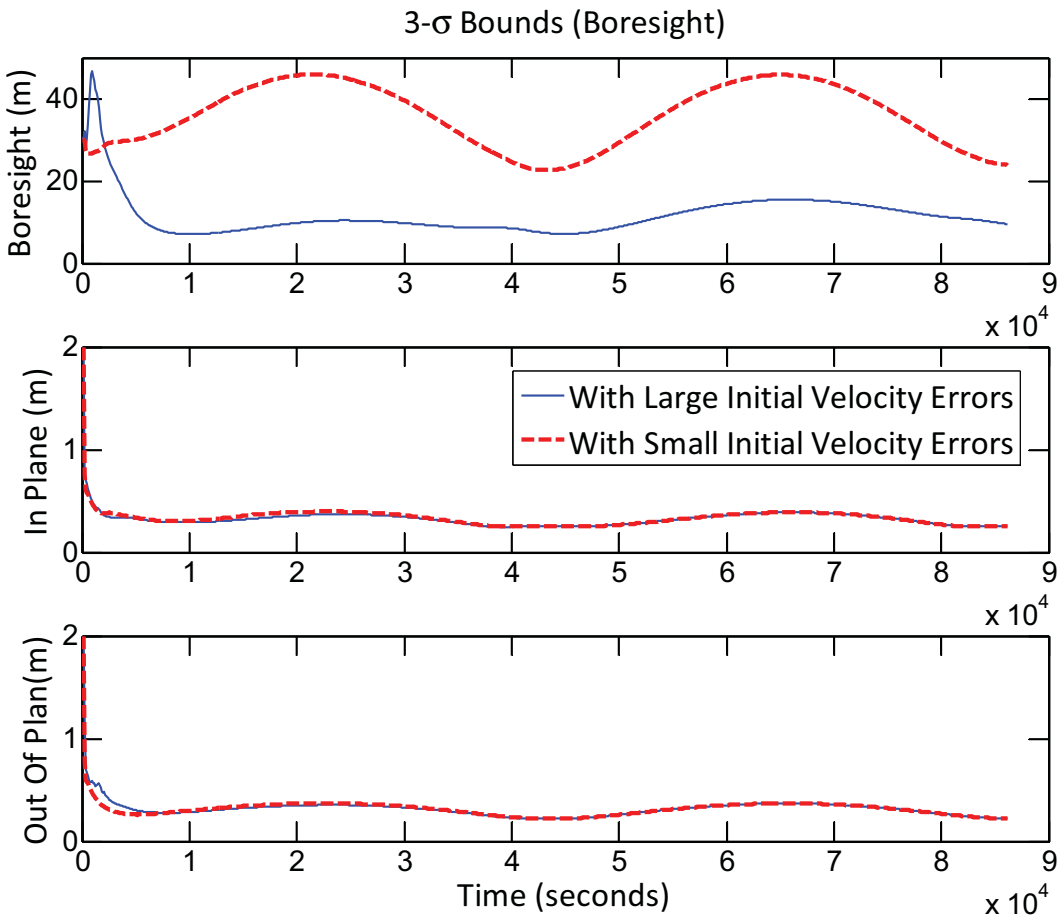

Fig. 7.17: Filter 3-σ bounds while in a football orbit (boresight, large initial uncertainty).

7.7.2 Accelerated Football

Range information can also be generated by using thrust to alter the football orbit. Starting with the same initial uncertainty as the first case above (the "small uncertainty" case), the chaser was forced to follow the path of a football orbit at 150% the natural speed. This maneuver used 0.1 m/s Δv and reduced the final line of sight error to 3.4 m 3-σ. Where the high-initial-uncertainty case gains most of its range information early in the simulation, the more constant thrust needed to force the chaser around the football orbit generates a more gradual decrease in uncertainty as seen in Figure 7.18. Figure 7.19 illustrates the thrust profile required for this orbit.

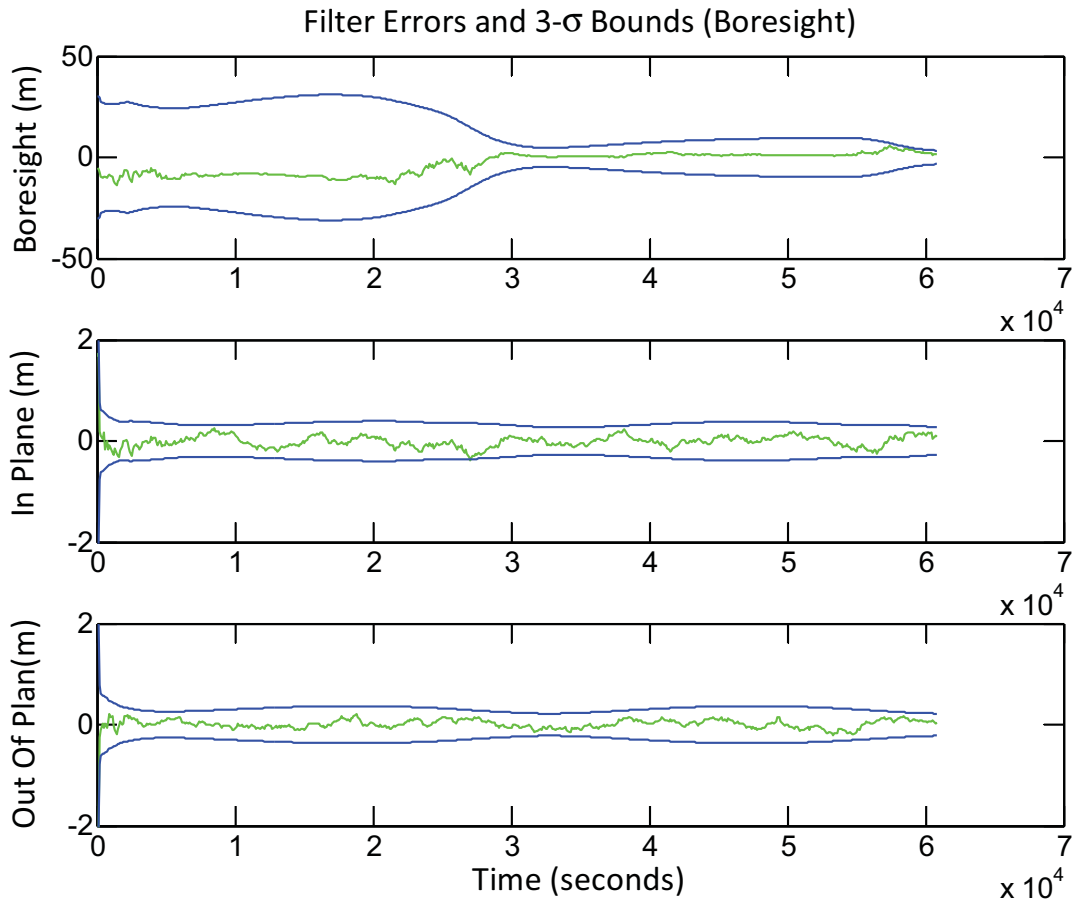

Fig. 7.18: Filter errors and 3-σ bounds while in an accelerated football (1.5X natural speed).

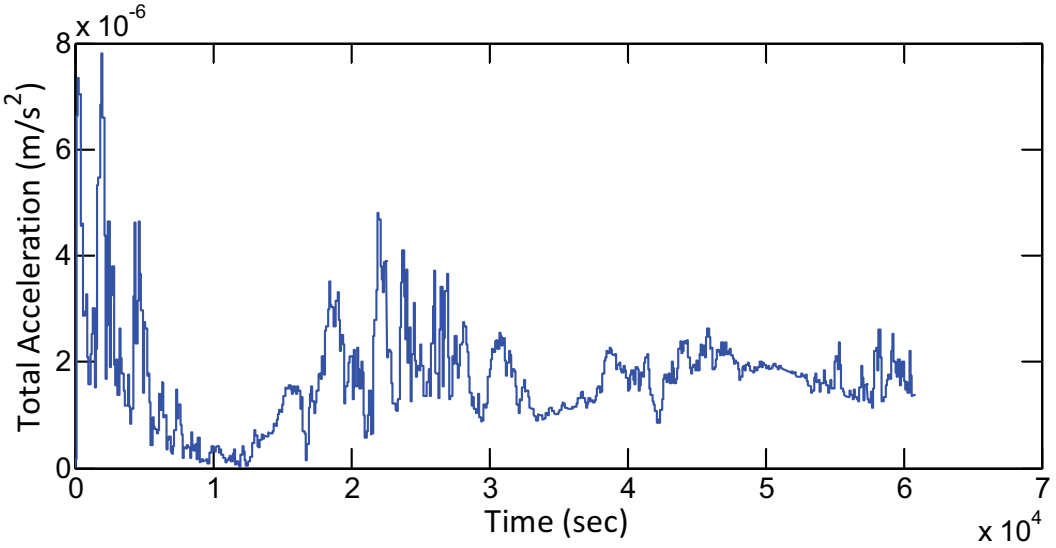

Fig. 7.19: Thruster acceleration while in an accelerated football (1.5X natural speed).

7.7.3 Rounded Accelerated Football

While running the accelerated football orbit scenarios, it was found to be significantly more fuel efficient to command the chaser to follow a slightly rounded orbit. Figures 7.20 and 7.21 show a forced 250x400 m modified football orbit. The period of this orbit and the initial uncertainties are the same as the accelerated football above, but the Δv is only about 0.06 m/s. However because less thrust is used in this case, the filter is not able to determine quite as much range information. Table 7.8 summarizes the LOS range uncertainty andΔv of the football orbits investigated here.

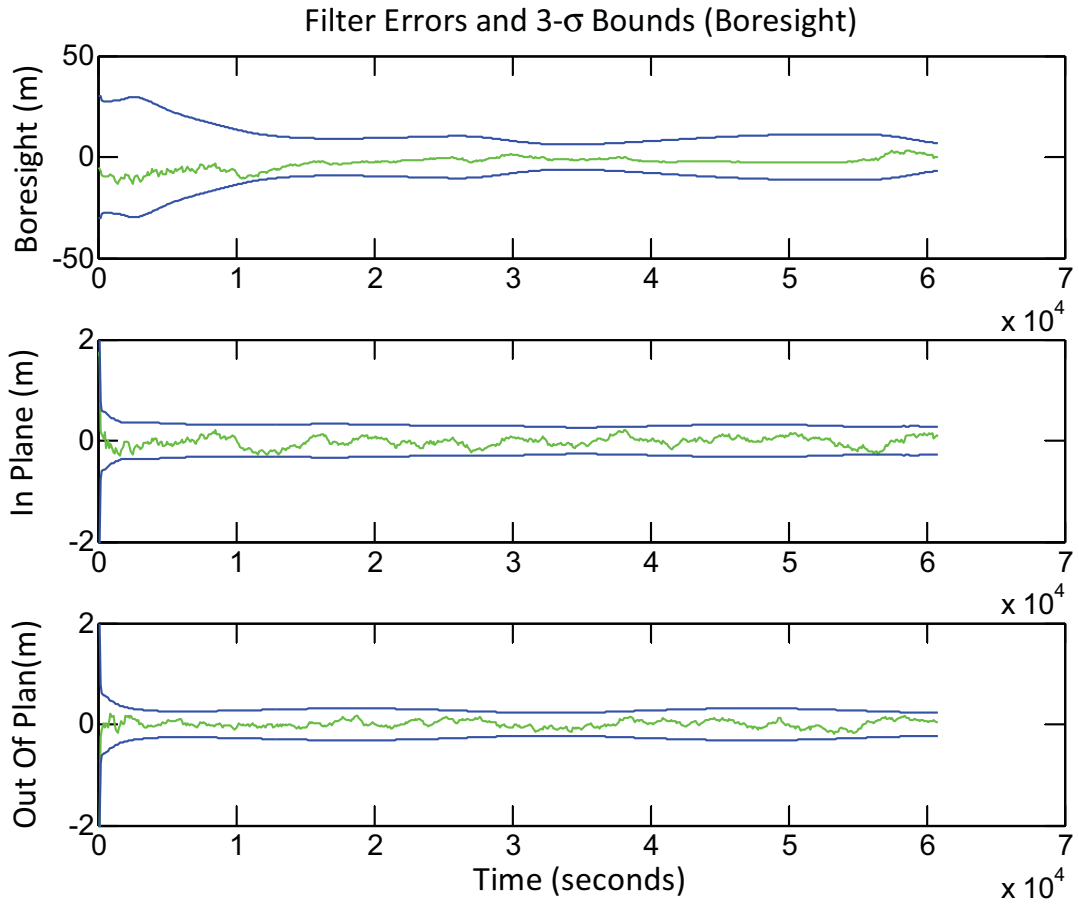

Fig. 7.20: Filter errors and 3-σ bounds while in an accelerated rounded football orbit (1.5X natural speed).

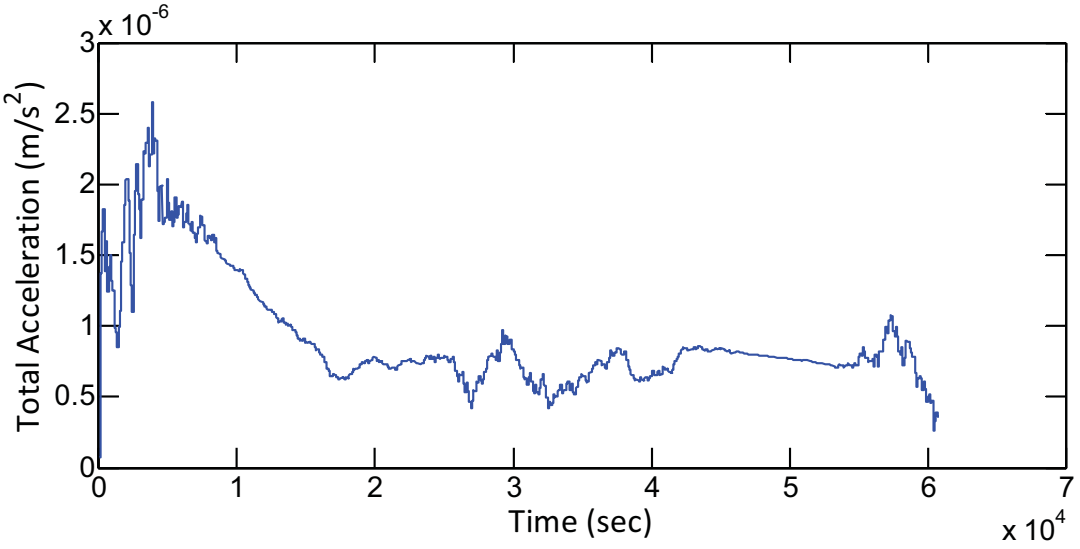

Fig. 7.21: Thruster acceleration while in an accelerated rounded football orbit (1.5X Natural Speed).

Table 7.8: Boresight Error 3-σ Bounds and Δv After One Football Orbit (Natural, Accelerated, and Rounded)

	Final Error		
	Natural	**Accelerated**	**Accelerated and Rounded**
Bore-sight Error 3-σ (m)	24	3.4	6.9
Δv (m/s)	0.006	0.1	0.06

7.8 Sample Mission

This section illustrates an example of how angles-only navigation and low-level-thrust can be used to successfully approach a spacecraft through a series of maneuvers. Each thrusting maneuver will move the chaser closer to the target and provide more range information. The chaser is able to maintain reasonable navigation accuracy through all parts of the mission using only angle measurements.

The chaser starts 20 km behind the target. A natural co-elliptic approach is used to move to 10 km behind the target. The chaser then uses a forced co-elliptic approach to move directly under the target. Finally a spiral approach is used to get closer to the target. An overview of the mission is shown in Figure 7.22.

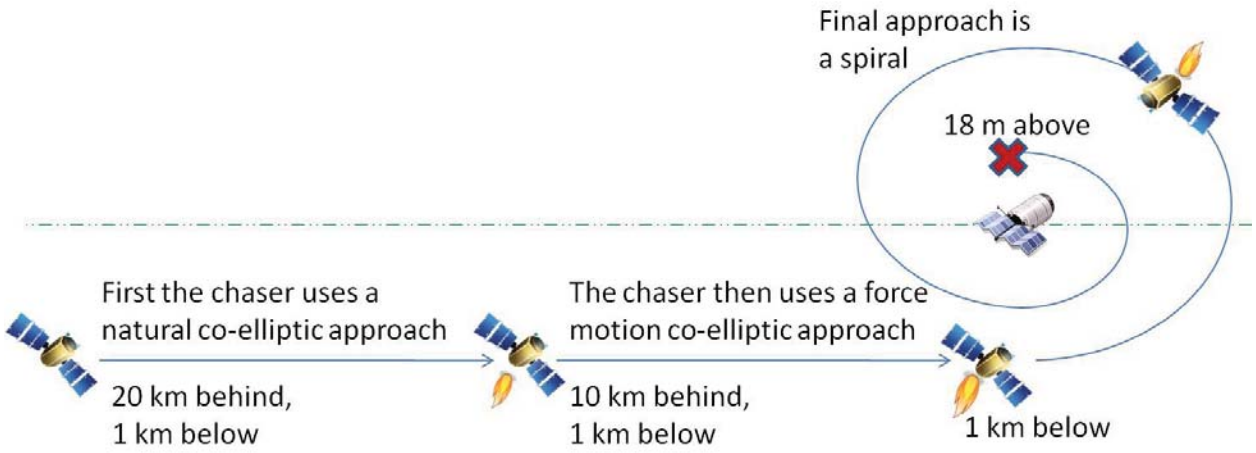

Fig. 7.22: Mission Overview.

7.8.1 Between Maneuver Transitions

For simulation purpose this mission is divided into various phases. Each phase corresponds to one of the sections below. For the first phase, the "Natural Linear Approach," the initial conditions, filter estimates, and 3-σ bounds are initialized using the same methods as the previous scenarios. The true initial state is generated randomly from a given initial desired position and initial covariance. However for each subsequent phase the initial conditions including filter variables are set equal to the end conditions of the previous phase. This way the maneuvers string together to form one mission that demonstrates how angles only navigation may be used by the chaser to approach the target from over 20 km away all the way to within 20 m.

7.8.2 Natural Linear Approach

For the natural linear approach, the chaser is initialized 20 km behind and 1 km below the target. This requires a relative velocity of $\dot{x} = \frac{3}{2}\omega_{geo}(1\,km)$ (see Equation 4.39). The starting relative position errors are 1500 m 3-σ/axis. Velocity errors are 3 m/s 3-σ/axis. For approximately one orbital period, the chaser approaches the target through a natural motion co-elliptic approach. This moves the chaser to a point 10 km behind the target, and 1 km below.

It is worth noting that the 3-σ bounds in Figure 7.23 decrease as the chaser gets closer to the target despite there being no significant thrusting. This is actually to be expected based on the orbital dynamics and the shape of the 3-σ bounds in this problem. The position 3-σ error starts out spherical, but as measurements are processed the 3-σ bounds quickly become a long ellipse. If the

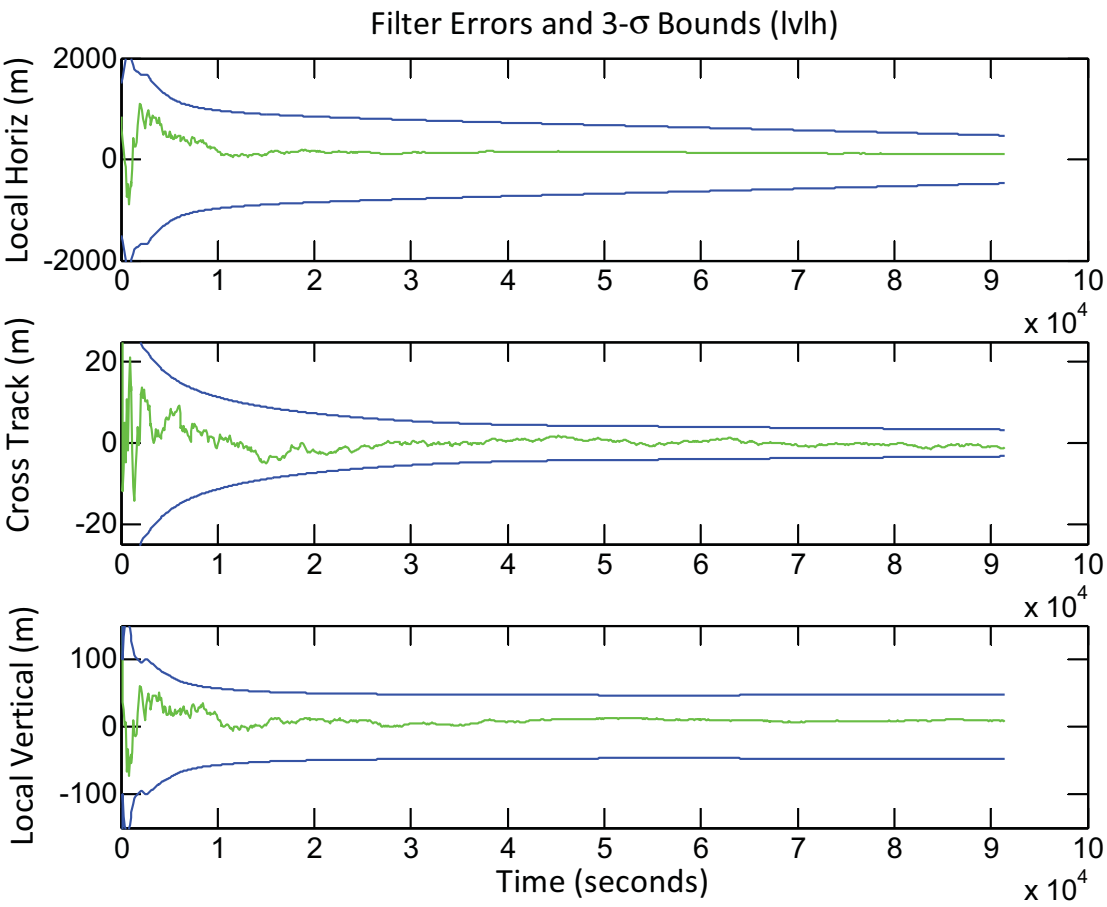

Fig. 7.23: Filter errors and 3-σ bounds while in a natural co-elliptic approach from 20 km to 10 km behind.

chaser position is closer to the target, it will also be have to be in a higher orbit, and if the chaser is farther from the target, it will also be in a lower orbit. Possible chaser positions farther away will in a sense catch up with a closer possible chaser positions. Even though the filter still can not distinguish between the different possible relative positions of the target, these possible positions move closer together so that the magnitude of the 3-σ bounds gets smaller. Despite the fact that all 3-σ bounds including range get smaller, no actual range information is gained. This is illustrated in Figure 7.24.

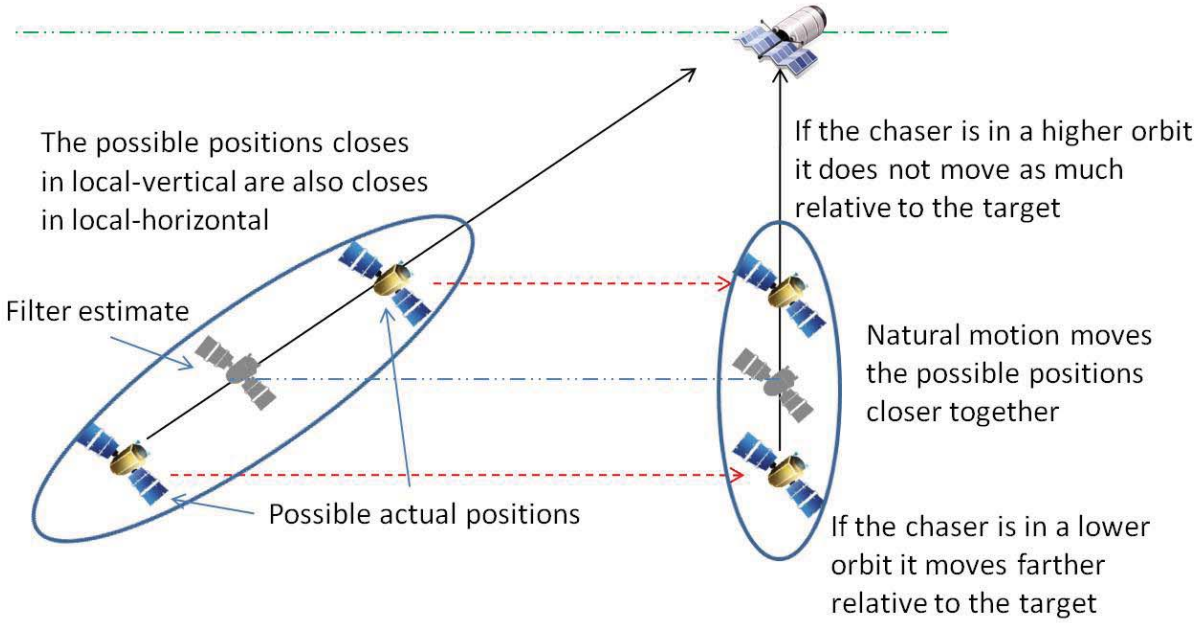

Fig. 7.24: Natural-motion evolution of the 3-σ bounds.

7.8.3 Forced Linear Approach

Once the chaser is 10 km behind it begins using thrust to accelerate its approach. Over 20,000 seconds of simulation time the chaser accelerates from the natural co-elliptic speed, $\frac{3}{2}\omega_{geo}$ (at 1 km below), to 4/3 the natural speed $2\omega_{geo}$. The chaser then maintains this speed, moving in a straight line, until it is 1 km below the target. This approach takes a total of 71200 seconds or just under 20 hours. As the chaser approaches the 1 km below position there is a decrease in local vertical uncertainty. This is clearly seen in Figure 7.25.

In order to better determine how much of the variance decrease comes from thrusting and how much is due to the effects of orbital motion described in Section 7.8.2, another simulation was run where the chaser was allowed to approach the target at natural speed. As can be seen in Figure 7.26, there is no improvement in local vertical information the natural speed case. The chaser is also less able to determine relative local horizontal position. Table 7.9 compares the natural and forced co-elliptic approaches.

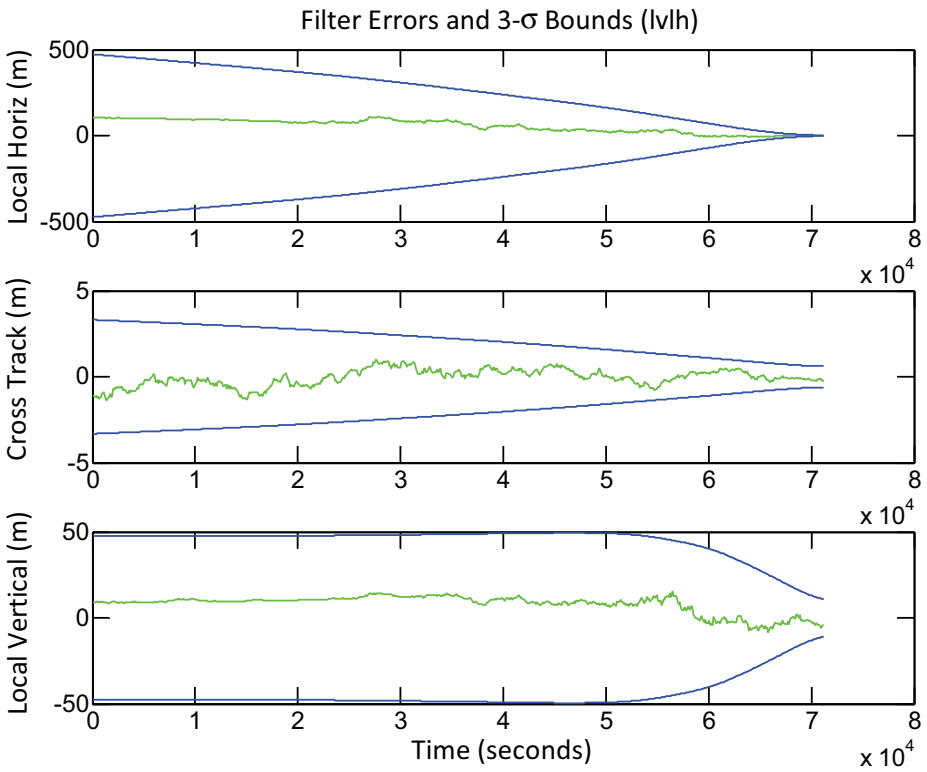

Fig. 7.25: Filter errors and 3-σ bounds while in a 4/3X speed co-elliptic approach.

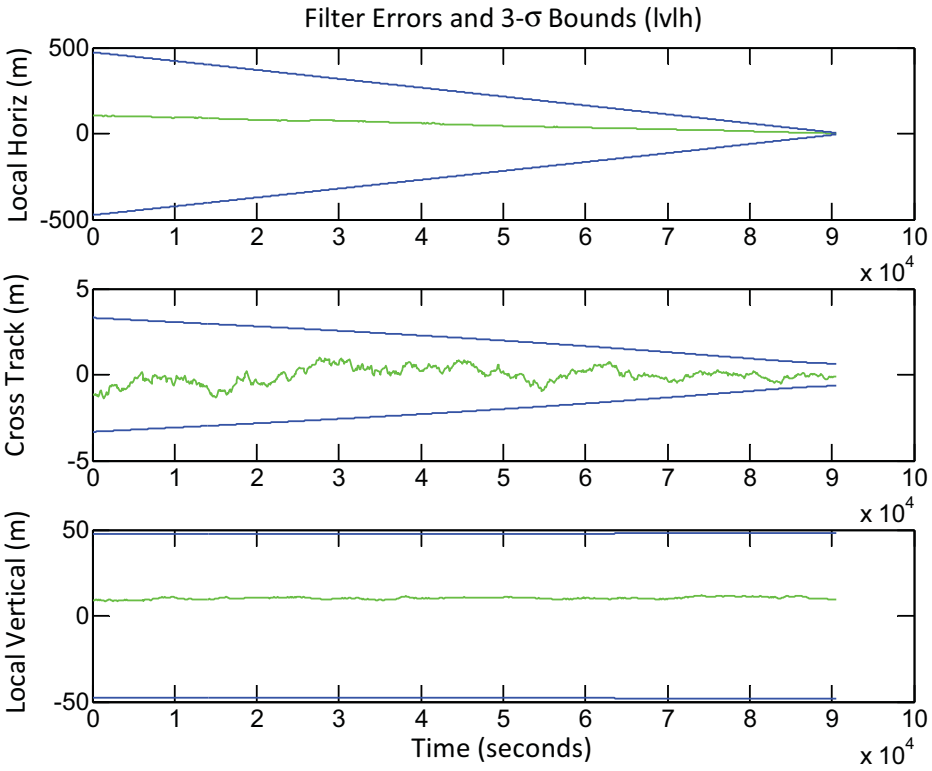

Fig. 7.26: Filter errors and 3-σ bounds while in a natural speed co-elliptic approach.

Table 7.9: Filter Error 3-σ Bounds and Δv for Natural and 4/3X Speed Co-elliptic Approaches

	Start (m)	**Natural Speed (m)**	**4/3X Speed (m)**
Vertical	47	48	11
Cross-track	3.3	0.6	0.6
Horizontal	474	4.9	0.8
Δv (m/s)	—	0.015	0.4

7.8.4 Spiral Approach

Once the chaser arrives at the position 1 km directly below the target from the 4/3X speed co-elliptic approach it begins to spiral towards the target. As can be seen from Equation 4.45, a natural 2x1 km football orbit would have the chaser traveling $2\omega_{geo}$(when $1\,km$ below) in the local horizontal direction. This means that when the chaser arrives at the point 1 km below the target it is already traveling the right speed and in the right direction for a natural football orbit. However, rather than going into a natural football orbit, the chaser gradually accelerates its relative angular speed to 20% faster than a natural football orbit. It takes the chaser 6 hours to reach the maximum speed. Over this same period of time the chaser also starts moving closer to the target. This maneuver can by thought of as a football orbit that gets smaller over time, the exact path being defined by Equations 5.34 through 5.37. Here the football decay rate is $d_{radial} = 0.875/\omega_{geo}$, the spiral is started immediately, $\tau_{s1} = 0$, and maximum radial velocity is reached after 6 hours, $\tau_{s2} = 6\,hr = 21600\,sec$. This maneuver takes the chaser from 1000 m below to just about 10 m above the target over about 110,000 seconds (just over 30 hours). This approach is illustrated in Figure 7.27. With an initial range error of 11 m 3-σ, this phase starts with a very good estimate of relative position. However, as is clearly shown in Figure 7.28, the filter is able to use this approach to further refine its estimates and bring the range error down to 2.6 m 3-σ. This phase uses about 0.26 m/s Δv. Table 7.10 summarizes the relative position 3-σ errors for each phase of this scenario. Table 7.11 illustrates that the filter is also able to accurately estimate relative velocity over the course of this scenario.

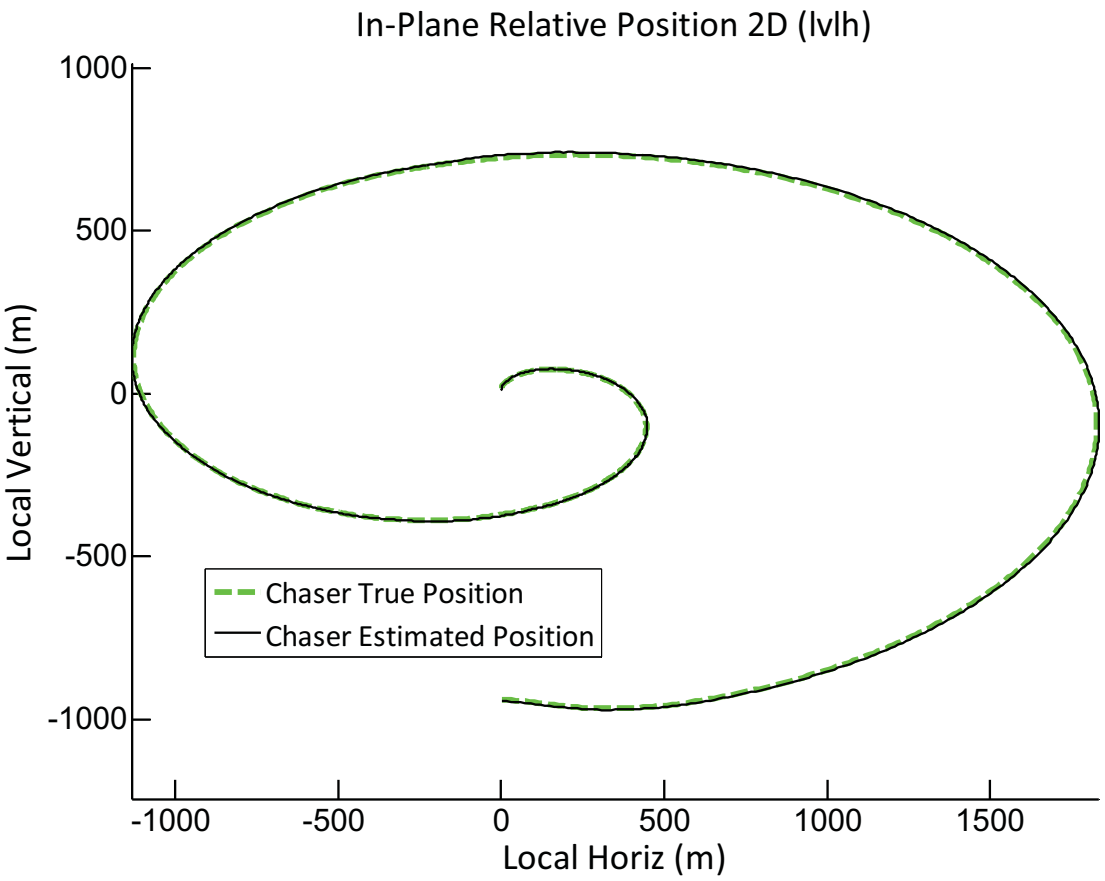

Fig. 7.27: Spiral approach.

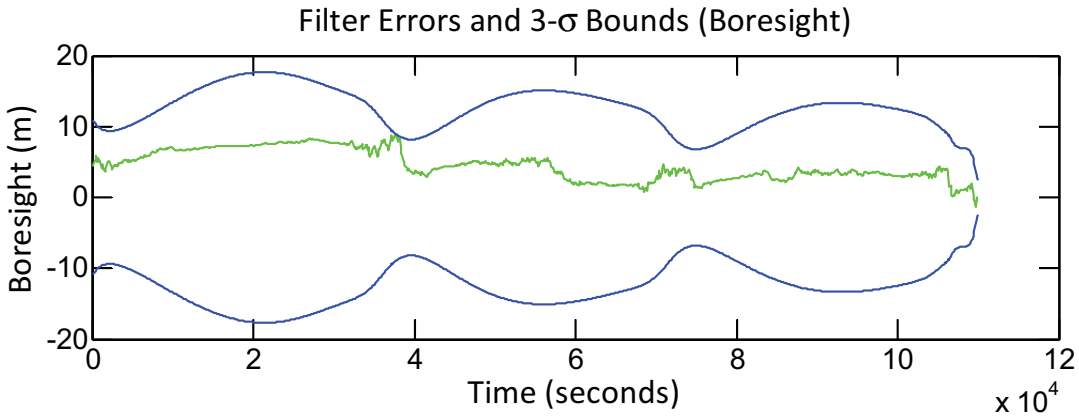

Fig. 7.28: Filter errors and 3-σ bounds while in a spiral approach.

Table 7.10: Filter Error 3-σ Bounds for Example Mission

	Start (m)	**After 20-10 km Co-elliptic (m)**	**After 10 km Co-elliptic (m)**	**After Spiral (m)**
Bore-sight	1500	476	11	2.6
In Plan	1500	4.6	0.6	0.026
Out of Plan	1500	3.3	0.8	0.021

Table 7.11: Boresight Errors 3-σ Bounds for Example Mission

	Start (mm/s)	**After 20-10 km Co-elliptic (mm/s)**	**After 10 km Co-elliptic (mm/s)**	**After Spiral (mm/s)**
Bore-sight	3,000	4.2	0.67	0.28
In Plan	3,000	1.3	1.6	0.39
Out of Plan	3,000	0.36	0.20	0.063

Chapter 8

Results - Effects of Sensor and Actuator Error Sources

To determine the effect of sensor and actuator error sources on range observability several different scenarios were run. The effectiveness of low-thrust assisted angles-only navigation in dealing with error sources is then determined by analyzing the resulting navigation filter state uncertainties.

8.1 Thruster Errors

The amount of thrust necessary to maintain a displaced orbit can be estimated from the CW equations. For the 500 m below station-keeping case from Section 7.6.2 the necessary steady state thrust can be calculated using Equation 4.29. Remembering that for this case $\dot{x} = 0$ and $\omega = \frac{2\pi\, rad}{24\, hr} = \frac{2\pi\, rad}{86400\, sec}$, the required thrust can be calculated as $a_z = -3\omega^2 z = 8\,\mu m/s^2$. Taking into account initial errors, measurement errors, and process noise, the simulation agrees very well with this calculation, as shown in Figure 8.1.

Until now, all the scenarios have assumed perfect thrusters. Now the 500 m below station-keeping case is rerun with thruster noise. An error equal to 10% of the steady state thrust $\left(Q_a = \left(0.8\,\mu m/s^2\right)^2 I_{3x3}\right)$ is added to the acceleration of the chaser every time step (100 s). Because of this extra source of noise, the filter is not able to estimate relative position quite as well as before, as can be seen in Figure 8.2. Considering the level of thruster uncertainty added here, the degradation of range information is relatively minor, and suggests that, even though some electric propulsion systems can track command thrusts very accurately [30], highly accurate thrusting knowledge may not be strictly necessary for this type of navigation.

Adding thruster noise at this point is some what redundant because the simulation already has process noise, and thruster noise is really just one type of process noise. To further illustrate this point, the simulation is run with the process noise turned off and thruster noise set to the same level as the process noise was before $\left(Q_a = (1.014\mu m/s^2)^2 I_{3x3} \text{ and } Q_d = 0_{3x3}\right)$. As can be seen in Figure 8.2 and Table 8.1, running the simulation with thruster noise instead of the process noise

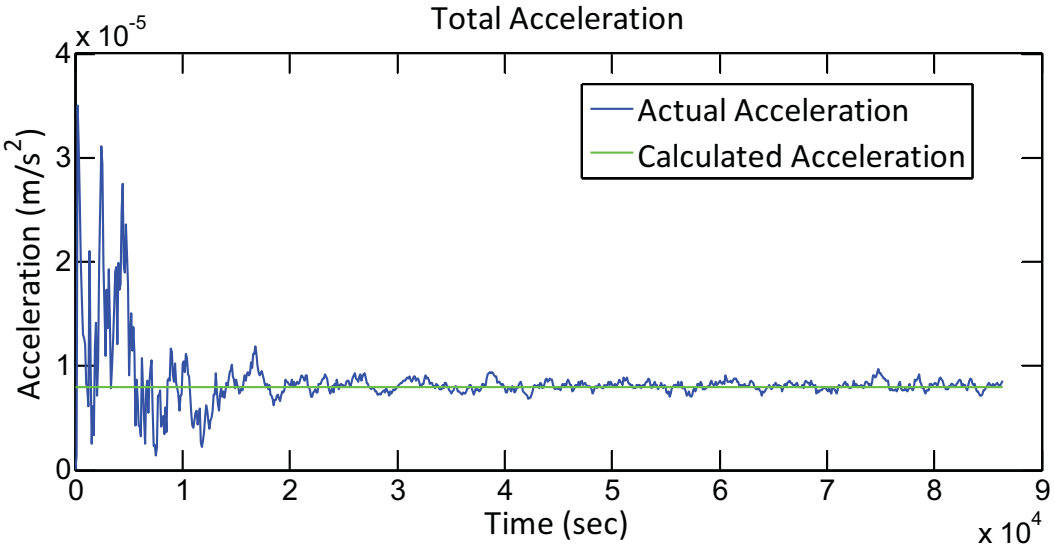

Fig. 8.1: Total acceleration while station-keeping 500m below for 24 hours.

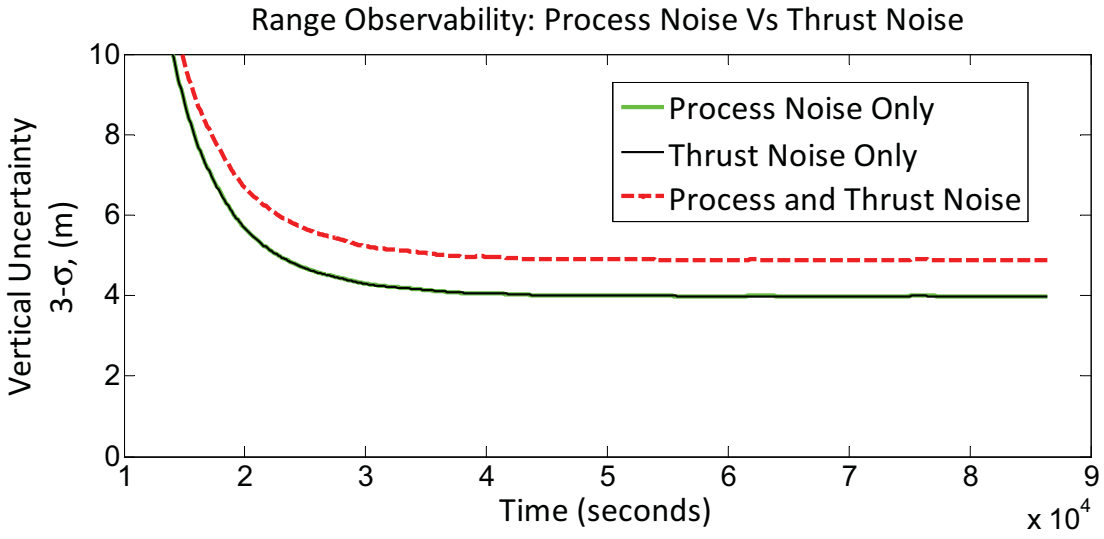

Fig. 8.2: Filter error 3-σ bounds while station-keeping 500 m below over 24 hours (process vs thruster noise).

Table 8.1: Filter Error 3-σ Bounds While station-keeping 500 Meters Below for 24 Hours (Process and Thruster Noise, Variable-Thrust Case)

	Initial Error	**Process Noise Only**	**Thruster Noise Only**	**Thruster and Process Noise**
Vertical Error (m)	75	4.0	4.0	4.9
Cross-track Error (m)	3	0.37	0.37	0.40
Horizontal Error (m)	3	0.44	0.44	0.49
Δv (m/s)	—	0.73	0.73	0.73

used before is almost identical to running the simulation with just process noise, at least as far as relative position detectability is concerned.

The simulation only adds thrust noise while the chaser's thrusters are actually thrusting. In the throttleable thrust case above, the thrust noise is always on since the thrusters are firing continuously. However, with the 10 cm/s minimum impulse case from Section 7.6.2, the thrusters are only firing part of the time (see Figure 8.3). This case is re-run with the same thrust noise as above $\left(Q_a = \left(0.8\,\mu m/s^2\right)^2 I_{3x3}\right)$, but the noise is only added when firings occur. Figure 8.4 shows a very similar effect to the above case. However, it appears that the thrust noise did not increase the uncertainty in the range estimate quite as much as in the constant thrust case. This makes sense since the the thrust noise term is only added some of the time here. To better understand the affect of only adding the noise part of the time, this case was re-run with $Q_a = (1.014\mu m/s^2)^2 I_{3x3}$ and $Q_d = 0_{3x3}$, identical to the "thrust noise only" case above, the difference being that the thrust noise will only be on part of the time. It can be seen in Figure 8.4 and Table 8.2 that this significantly reduces the range uncertainty.

Table 8.2: Filter Error 3-σ Bounds While Station-Keeping 500 Meters Below for 24 Hours (Process and Thruster Noise, Low-Minimum Impulse Case)

	Initial Error	**Process Noise Only**	**Thruster Noise Only**	**Thruster and Process Noise**
Vertical Error (m)	75	3.9	3.0	4.4
Cross-track Error (m)	3	0.43	0.41	0.45
Horizontal Error (m)	3	0.37	0.34	0.39
Δv (m/s)	—	44.0	46.2	49.0

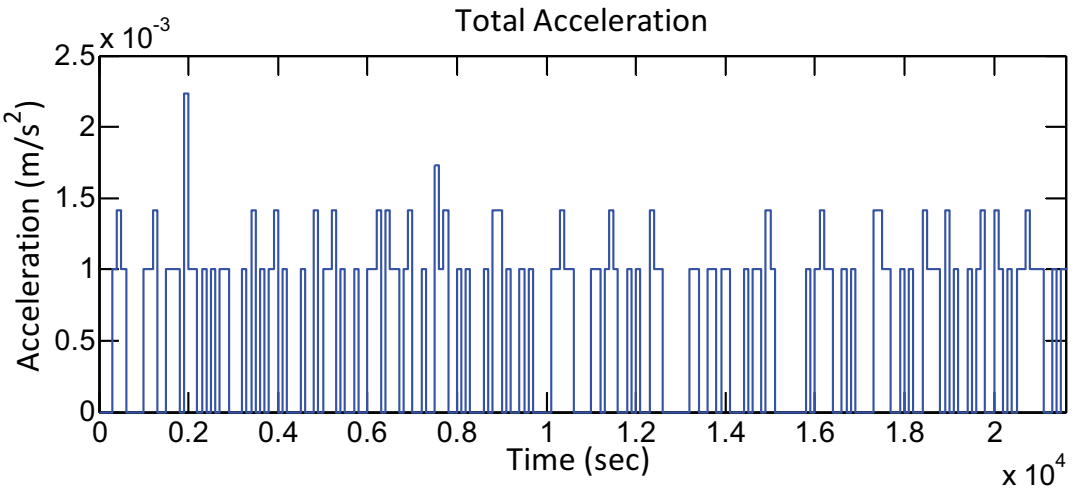

Fig. 8.3: Total acceleration with fixed thrust while station-keeping 500m below for 6 hours.

While $0.8\,\mu m/s^2$ is 10% of steady state thruster acceleration for the throttleable case, the minimum impulse case generates much higher accelerations. It can be seen in Figure 8.3 that the minimum none-zero acceleration is $1 \times 10^{-3} m/s^2$. This is given by the minimum impulse divided by the simulation time step: $a_{min} = \Delta v_{min}/t_{step} = (0.1\,m/s)/100\,s = 1 \times 10^{-3} m/s^2$. The simulation is run again with the thrust noise set to one tenth the minimum acceleration $\left(Q_a = \left(1 \times 10^{-4}\,m/s^2\right)^2 I_{3x3}\right)$. It can be seen in Table 8.3 and Figure 8.5 that, unlike in the throttleable case, the chaser is unable to estimate range well. The likely explanation is that in this case the chaser control system is "chattering" a lot. The chaser first thrusts in one direction and then has to thrust in the opposite direction to correct the excessive thrust due to the relatively high minimum impulse, so that over time the average thrust is the same $0.8\,\mu m/s^2$ as the throttleable case. However, since the noise terms are uncorrelated they do not cancel out; making it impossible for the filter to estimate what the true average acceleration is. It is worth noting that it is very unlikely that a spacecraft would ever really try to station keep this way. The control is set very tight in this case so that the chaser stays almost as close to the desired point as in the throttleable case. A real spacecraft control system would have a dead-band and allow itself to drift away for a little while, then thrust again to move back towards the desired position. This strategy would save significant Δv. With less thrusting the Kalman filter would have to deal with less thrust noise, and the estimate and covariances would undoubtedly improve.

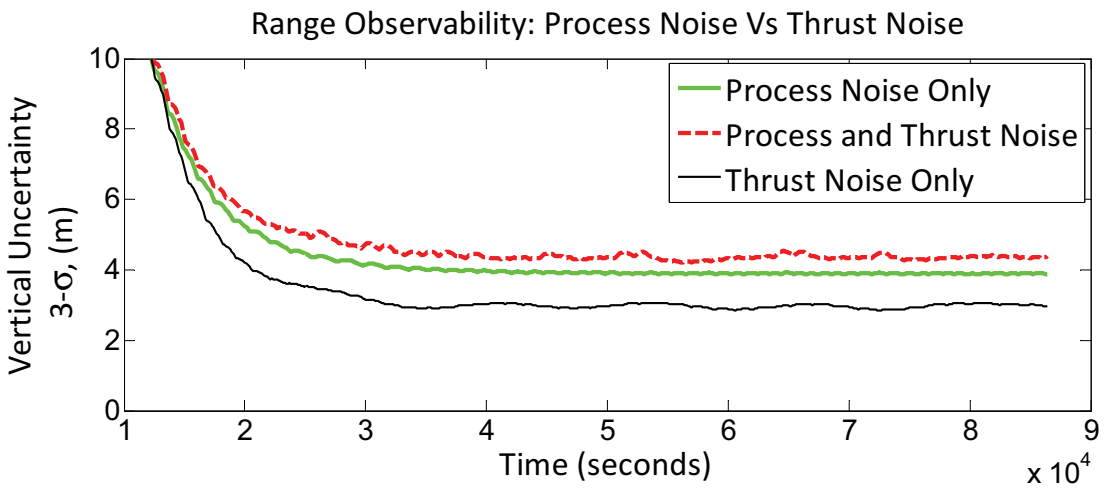

Fig. 8.4: Filter error 3-σ bounds while station-keeping 500 m below over 24 hours (process vs thruster noise, low-minimum impulse case).

Table 8.3: Filter Error 3-σ Bounds While Station-Keeping 500 Meters Below For 24 Hours (Process and Thruster Noise, High-Minimum Impulse Case)

	Initial Error	**Process Noise Only**	**Process Noise and High Noise Thrusters**
Vertical Error (m)	75	3.9	55.7
Cross-track Error (m)	3	0.43	1.01
Horizontal Error (m)	3	0.37	1.01
Δv (m/s)	—	44.0	47.7

8.2 Angular Acceleration Process Noise

Thus far, all analysis has been done without any perturbations in the attitude dynamics. The goal of this section is to investigate the effects of random rotational perturbations implemented as white process noise. The desired to actual attitude quaternion can be written as:

$$q = \begin{bmatrix} \cos(\alpha/2) \\ \sin(\alpha/2)\cos(\beta_x) \\ \sin(\alpha/2)\cos(\beta_y) \\ \sin(\alpha/2)\cos(\beta_z) \end{bmatrix}$$

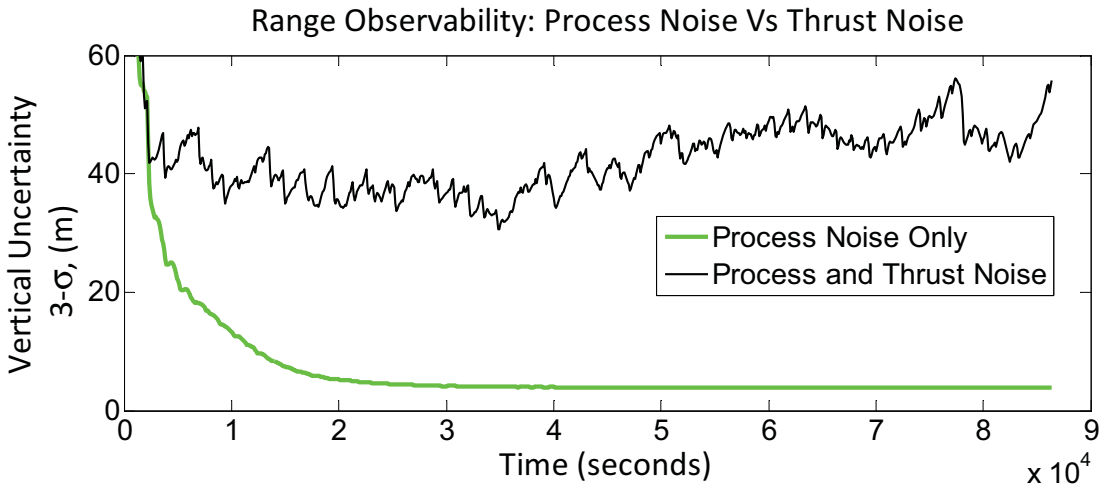

Fig. 8.5: Filter error 3-σ bounds while station-keeping 500 m below over 24 hours (process vs thruster noise, high-minimum impulse case).

where α is the rotation angle and $\cos(\beta_x)$, $\cos(\beta_y)$, and $\cos(\beta_z)$ are the direction cosines locating the axis of rotation. The angular error between the desired and actual attitudes can then be written as:

$$\alpha_e = 2\cos^{-1}(q_{0,e})$$

where $q_{0,e}$ is the first element of the error quaternion q_e (the quaternion representing the rotation from the actual to desired attitude). The angular error for the 500 m below station-keeping case from Section 7.6.2 is plotted in Figure 8.6.

Except for at the very beginning when the chaser is first "homing in" on the target, the attitude control system is able to keep the chaser well within 0.1 degrees of the desired orientation. Over this 12 hour segment the chaser uses .0.38 m/s Δv and is able to lower the 3-σ bounds in the boresight direction to 4.0 m.

When a random angular acceleration is added, the angular errors can be significantly larger. Figure 8.7 shows the results when a random angular acceleration with $\sigma = 1e-5\,rad/s^2$ is added to the dynamics. This makes it harder for the attitude control system to maintain the desired orientation. However, as can be seen if Figure 8.8, despite the much larger orientation errors, there is no significant difference in the filter 3-σ bounds. In this case, the chaser again uses 0.38 m/s Δv and is able to lower the 3-σ bounds in the boresight direction to 4.0 m. There does not seem to be

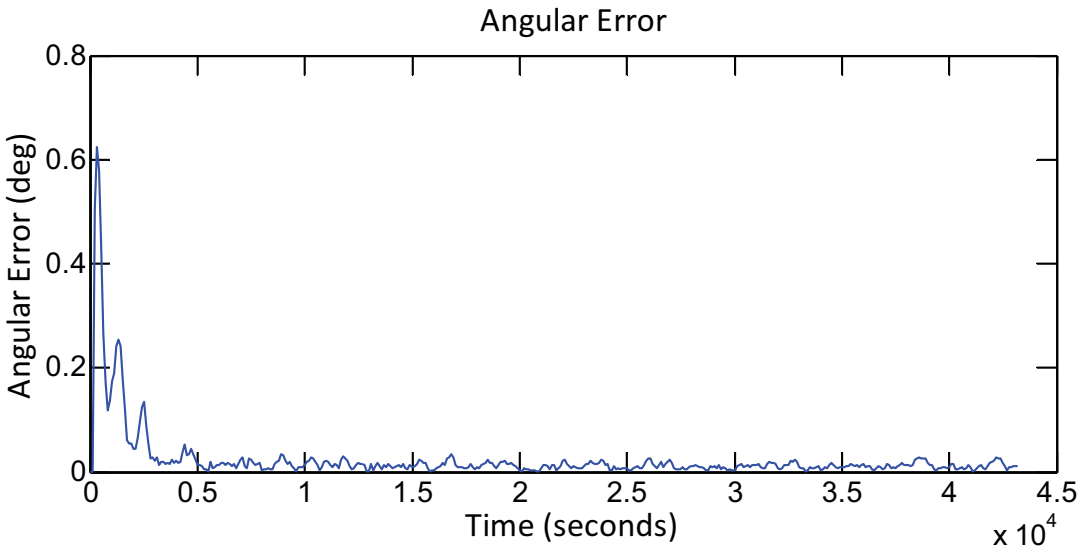

Fig. 8.6: Angular error without angular noise while station-keeping 500 m below over 12 hours.

any significant difference between this case and the previous when it comes to translational control or relative position knowledge. This fact suggest that when angular knowledge is good, as it is in this case, that precise angular control is not necessary for this type of angles-only navigation.

8.3 Star-Tracker Noise

All analysis thus far has assumed a perfect star-tracker. For many cases this may not be far from the true. A good star-tracker is likely much more accurate than other sources of error like the LOS camera. However, in many cases there may be reasons (cost, size, etc...) to use less accurate attitude determination sensors. To explore the effect of decreased attitude certainty, the 500 m below, station-keeping case, from Section 7.6.2 is re-run with noise on the star-tracker.The simulation is first run with 3 mrad 3-σ noise on the star tracker and a perfect LOS camera. Since the chaser's Kalman filter does not estimate attitude, this noise is accounted for by adding a new noise term R_{star} to the covariance update equation associated with LOS camera measurements. As expected, the uncertainty in the range direction is almost exactly the same as the base case where the star-tracker is perfect and the LOS camera has 3 mrad 3-σ noise on it. This is seen in Figure 8.9 and Table 8.4. The simulation is also run with both noise sources turned on. It can be seen that both noises sources together produced a small but measurable decrease in range certainty. While star-trackers can be very accurate, other forms of attitude measurements have significant errors. Magnetometers are limited to accuracies of about half a degree [37] ($0.5^o = 8.7\,mrad$). The

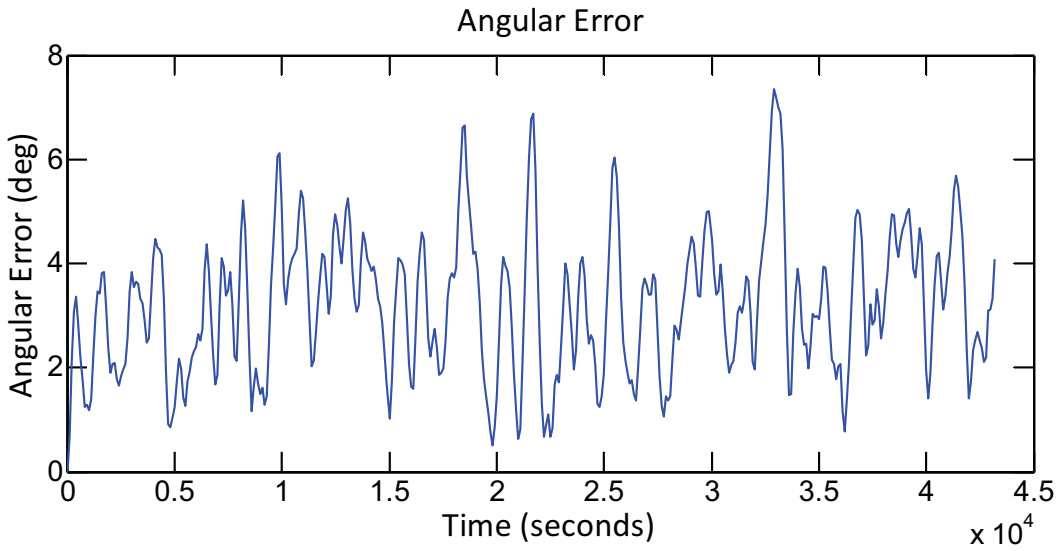

Fig. 8.7: Angular error with angular noise while station-keeping 500 m below over 12 hours.

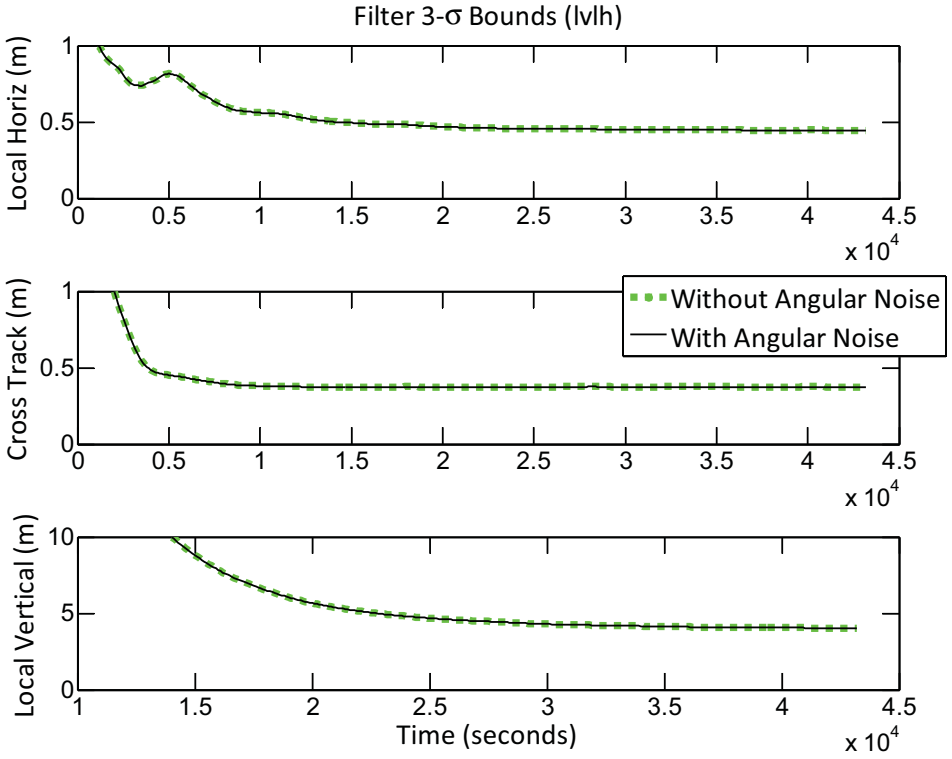

Fig. 8.8: Filter error 3-σ bounds while station-keeping 500 m below over 24 hours (with/without angular noise).

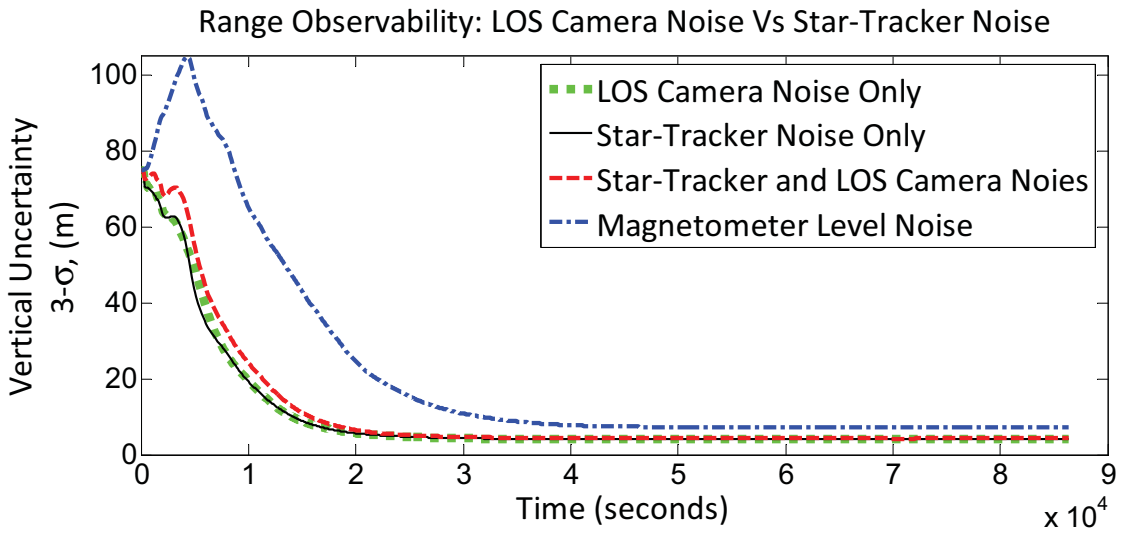

Fig. 8.9: Filter error 3-σ bounds while station-keeping 500 m below for 12 hours (LOS camera and star-tracker noise).

Table 8.4: Filter Error 3-σ Bounds While Station-Keeping 500 Meters Below For 12 Hours (LOS Camera and Star-tracker Noise)

	Initial Error	**LOS Camera Noise Only**	**LOS Camera and Star-tracker Noise**	**Magnetometer Level Noise**
Vertical Error (m)	75	4.0	4.2	7.2
Cross-track Error (m)	3	0.37	0.49	2.0
Horizontal Error (m)	3	0.44	0.59	3.0
Δv (m/s)	—	0.73	0.75	0.77

simulation is run again with 3 mrad 3-σ noise on the LOS camera and with 30 mrad 3-σnoise on the "star-tracker" to simulate a less accurate attitude determination sensor like a magnetometer. It can be seen in Figure 8.9 that, even though the final range estimate in this case is more uncertain than in the lower noise cases, the estimate is still pretty good (under 10 m from 500 m away, less than a 2% error in the range estimate). Figure 8.10 displays the same scenarios, but is zoomed in to better illustrate the steady state 3-σ bounds.

In addition to making accurate relative angle measurements more difficult, poor attitude knowledge also produces thrust errors. This is due to the chaser not firing in exactly the commanded direction. However, in this case the disturbance thrust due to inaccurate pointing is rather small. The worse case is the "magnetometer" noise level case. Recalling that the steady state thrust for this case is $\sim 8\,\mu m/s^2$ and using small angle approximation the variance of the disturbance thrust

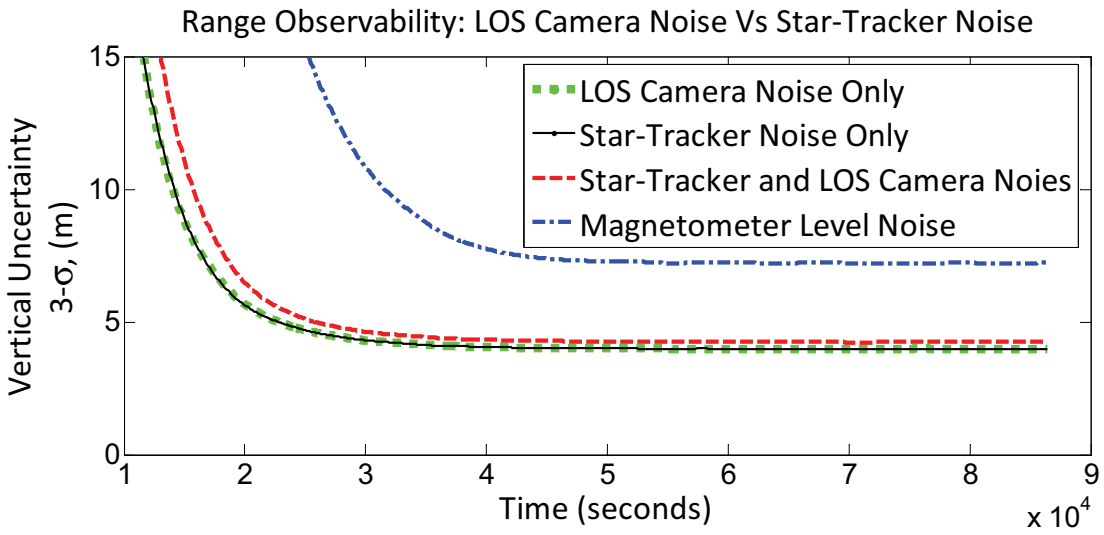

Fig. 8.10: Filter error 3-σ bounds while station-keeping 500 m below for 12 hours (LOS camera and star-tracker noise, zoomed in).

can be calculated as: $\sigma_{thrust} = 0.01\left(8\,\mu m/s^2\right) = 0.08\,\mu m/s^2$. This is well below the process noise $\left(1.014\mu m/s^2\right)$ already included in the simulation. Because the added thruster noise was so much lower than the base noise, the Kalman filter was able to work just fine. However, if this noise term were to get significantly larger, maybe due to a higher thrust maneuver or even worse attitude sensors, another noise term would need to be added to the propagation step in the Kalman filter to account for it.

Chapter 9

Conclusions and Future Work

When this study was first begun, it was believed that range information could be calculated from angle information augmented by knowledge of the magnitude and direction of thrust needed to maintain a desired angular position. The objective of this thesis was to prove that angles only navigation (AON) can produce significant range information when assisted by low continuous thrust.

This hypothesis has been proved to be true. In the scenarios studied, the chaser was able to determine relative range using LOS-angle measurements for a variety of low-thrust maneuvers, including nominal operational maneuvers. Forced motion also enhances angles-only navigation. In either case, it is clear that even small maneuvers provide good range detectability.

While this thesis focused primarily on geosynchronous orbit applications, low-thrust assisted angles-only navigation is also expected to be equally valid in any orbit. Low-thrust assisted angles-only navigation was also shown to work well for both throttable and fixed minimum-impulse case. Additionally, it was shown that even without thrusting relative angle measurements can be used to accurately estimate relative velocity. This can be particularly important for docking operations where relative velocity must be well controlled to avoid damage to either the target or chaser.

In one scenario the chaser's filter was able to accurately determine relative position at every point of a multiple step mission that took the chaser from over 20 km away from the target to near docking. Over this series of maneuvers the filter was also able to maintain a very accurate relative velocity estimate. This shows that low-thrust assisted AON works over a wide variety of distances and can potentially be used as a stand alone relative navigation solution.

The sensitivity of low-thrust assisted AON to error and perturbation sources was also investigated. When thruster/actuator errors were added to the thrust command the filter was not able to estimate LOS-range as well as it did with perfect thrust. However, this decrease in estimate accuracy was relatively small. Even when the thruster errors where equal to 10% of the total thrust, the filter LOS-range estimate 3-σ bounds was still less 1% of LOS-range.

When angular acceleration disturbances were added to the attitude dynamics the error

between the true and desired angular position increased significantly. However, the quality of the relative position estimate was shown to be insensitive to these rotational disturbances. Even when actual angular position was varying from the desired angular position by six or more degrees, the relative position estimate 3-σ bounds where essentially identical to the 3-σ bounds without perturbations in the attitude dynamics.

When measurement errors were added to the star-tracker data, the filter relative position 3-σ bounds increased. However, when the star-tracker measurements where corrupted by noise levels comparably to what would be expected from a magnetometer (1.5^o 3-σ error), the Kalman filter was still able to calculate a LOS range estimate with 3-σ bounds that where less than 2% of the LOS range.

Overall these findings suggest that low-thrust assisted angles-only navigation is a viable candidate for relative navigation, whether as a primary solution or as a supplement and/or backup to other navigation systems.

References

[1] Mitchell, I. T. and Gorton, T. B., "GN&C Development of XSS-11 Micro-Satellite for Autonomous Rendezvous and Proximity Operations," *Procedings of the 29th Annual AAS Guidance and Control Conference*, No. AAS 06-014, February 2006.

[2] Rumford, T. E., "Demonstration of Autonomous Rendezvous Technology (DART) Project Summary," *Proceedings of SPIE Space Systems Technology and Operations*, Vol. 5088, Orlando, FL, April 2003, pp. 10–19.

[3] Weismuller, T. and Leinz, M., "GN&C Technology Demonstrated by the Orbital Express Autonomous Rendezvous and Capture Sensor System," *AAS Rocky Mountain Section, 29th Annual AAS Guidance and Control Conference*, No. AAS 06-016, Boeing, Breckenridge, CO, February 2006.

[4] Chari, R. J. V., *Autonomous Orbital Rendezvous Using Angles-Only Navigation*, Master's thesis, Massachusetts Institute of Technology, June 2001.

[5] Woffinden, D. C. and Geller, D. K., "Navigating the Road to Autonomous Orbital Rendezvous," *Journal of Spacecraft and Rockets*, Vol. 44, No. 4, July 2007, pp. 898–909.

[6] Schmidt, J. K., *Analysis of Square-Root Kalman Filter for Angles-Only Orbital Navigation and the Effects of Sensor Accuracy on State Observability*, Master's thesis, Utah State University, 2010.

[7] Goebel, D. M. and Katz, I., *Fundamentals of Electric Propulsion: Ion and Hall Thrusters*, John Wiley & Sons, Hoboken, NJ, 2008.

[8] Mason, L. and Oleson, S. R., "Spacecraft Impacts with Advanced Power and Electric Propulsion," *Proceedings of IEEE Aerospace Conference*, Vol. 4, Big Sky, MT, Mar. 2000, pp. 29–38.

[9] Parten, R. P. and Mayer, J. P., "Development of the Gemini Operational Rendezvous Plan," *Journal of spacecraft and rockets*, Vol. 5, No. 9, September 1968, pp. 1023–1028.

[10] Young, K. A. and Alexander, J. D., "Apollo Lunar Rendezvous," *Journal of Spacecraft and Rockets*, Vol. 7, No. 9, Sep. 1970, pp. 1083–1086.

[11] Fehse, W., *Automated Rendezvous and Docking of Spacecraft, Chapter 7.2.5 Example: The Russian Kurs System*, Cambridge University Press, New York, NY, 2003.

[12] Pearson, D. J., "Shuttle Rendezvous and Proximity Operations," *Space Dynamics*, 1989, pp. 833–851, http://home.comcast.net/ djpearson/rndz/rndzpaper.html.

[13] NASA, "Overview of the DART Mishap Investigation Results," May 2006.

[14] Bingham, B. E. and Geller, D. K., *Preliminary Orbit Determination for Orbital Rendezvous using Gauss' Method*, Master's thesis, Utah State University, 2007.

[15] Curtis, H. D., *Orbital Mechanics for Engineering Students*, Elsevier Ltd, Linacre House, Jordan Hill, Oxford, 2005.

[16] Jo Ryeong Yim, J. L. C. and Junkins, J. L., "Autonomous Orbit Navigation of Two Spacecraft System Using Relative Line of Sight Vector Measurements," *AAS Space Flight Mechanics Meeting*, Maui, HI, 2004.

[17] Aidala, V. J., "Kalman Filter Behavior in Bearings-Only Tracking Applications," *IEEE Transactions on Aerospace and Electronic Systems*, Vol. AES-15, IEEE, Jan. 1979, pp. 29–39.

[18] Junkins, J., Hughes, D., Wazni, K. P., and Pariyapong, V., "Vision-Based Navigation for Rendezvous Docking and Proximity Operations," *22nd Annual AAS Guidance and Control Conference*, Vol. AAS 90-021, Breckenridge, CO, February 1999.

[19] Alonso, R., C. J. and Junkins, J., "Vision-Based Relative Navigation For Formation Flying of Spacecraft," *AIAA Guidance, Navigation and Control Conference*, No. AIAA-2000-4439, Denver, CO, Aug. 2000.

[20] Chen, T. and Xu, S., "Double Line-of-Sight Measuring Relative Navigation for Spacecraft Autonomous Rendezvous," *Acta Astronautica*, Vol. 67, July-August 2010, pp. 122–134.

[21] Stallard, D. V., "Angle-Only Tracking Filter in Modified Spherical Coordinates," *Journal of Guidance, Control, and Dynamics*, Vol. 14, No. 3, 1991, pp. 694–696.

[22] Hablani, H. B., "Autonomous Inertial relative Navigation with Sight-Line-Stabilized Integrated Sensors for Spacecraft Rendezvous," *Journal of Guidance, Control, and Dynamics*, Vol. 32, No. 1, January-February 2009, pp. 172–183.

[23] Woffinden, D. C., *Angles-only Navigation for Autonomous Orbital Rendezvous*, Ph.D. thesis, Utah State University, 2008.

[24] Martinez-Sanchez, M. and Pollard, J. E., "Spacecraft Electric Propulsion - An Overview," *Journal of Propulsion and Power*, Vol. 14, No. 5, September-October 1998, pp. 688–699.

[25] Anderson, J., Goodfellow, K., Polk, J., Rawlin, V., and Sovey, J., "Performance Characteristics of the NSTAR Ion Thruster During an On-Going Long Duration Ground Test," *IEEE Aerospace Conference Paper 8.0303*, Mar. 2000.

[26] Polk, J., Anderson, J., Goodfellow, K., Rawlin, V., and Sovey, J., "In-Flight Performance of the NSTAR Ion Propulsion System on the Deep Space One Mission," *IEEE Aerospace Conference Paper 8.0304*, March 2000.

[27] Patterson, M. and Benson, S., "NEXT Ion Propulsion System Development Status and Capabilities," *Proceedings, 2007 NASA Science Technology Conference*, Collage Park, MD, June 19-21 2007.

[28] Rossetti, P., Saverdi, M., and Biagoni, L., "Electric-Propulsion Systems," *Advanced propulsion systems and technologies, today to 2020*, Vol. 223, 2008, pp. 223–289.

[29] Meckel, N. J., Cassady, R. J., Osborne, R. D., Hoskins, W. A., and Myers, R. M., "Investigation of Pulsed Plasma Thrusters for Spacecraft Attitude Control," *IEPC-97-128*, Aug. 1997.

[30] Marcuccio, S., Genovese, A., and Andrenucci, M., "Experimental Performance of Field Emission Microthruster," *Journal of Propulsion and Power*, Vol. 14, 1998, pp. 774–781.

[31] Blandino, J. and Rock, B. S., "Micronewton Thruster Requirements for Earth-Orbiting Imaging Formation," *Journal of Spacecraft and Rockets*, Vol. 43, No. 3, May-June 2006, pp. 673–684.

[32] McKay, R., Macdonald, M., de Frescheville, F. B., Vasile, M., McInnes, C., and Biggs, J., "Non-Keplerian Orbits Using Low Thrust, High ISP Propulsion Systems," *60th International Astronautical Congress*, Daejeon, South Korea, 2009.

[33] Bryson, A. E. and Ho., Y., *Applied Optimal Control: Optimization, Estimation, and Control*, Taylor and Francis, revised edition ed., 1975.

[34] Clohessy, W. H. and Wiltshire, R. S., "Terminal Guidance System for Satellite Rendezvous," *Journal of the Astronautical Sciences*, Vol. 27, No. 9, 1960, pp. 641–652.

[35] Kalman, R., "A New Approach to Linear Filtering and Prediction Problems," *Transactions of the ASME - Journal of Basic Engineering*, Vol. 82, 1960, pp. 35–45.

[36] Maybeck, P., *Stochastic Models, Estimation, and Control*, Vol. 1, Navtch Book and Software Store, New York, NY, 1994.

[37] Fortescue, P., Stark, J., and Swinerd, G., editors, *Spacecraft Systems Engineering*, John Wiley & Sons Ltd., Southern Gate, Chichester, West Sussex, England, 2003.